

Silicon Photomultiplier Classification of the Pre-Production GCT Camera of CTA

Silicon Photomultiplier Klassifikation der Pre-Production GCT Kamera von CTA

Master-Thesis von Ben Gebhardt aus Heidelberg

Tag der Einreichung:

1. Gutachten: Dr. Richard White (MPIK)

2. Gutachten: Prof. Jim Hinton (MPIK)

3. Gutachten: Prof. Tetyana Galatyuk (TU DA)



TECHNISCHE
UNIVERSITÄT
DARMSTADT

Fachbereich Physik

Max Planck Institut für Kernphysik Heidelberg

8 Silicon Photomultiplier Classification of the Pre-Production GCT Camera of CTA
Silicon Photomultiplier Klassifikation der Pre-Production GCT Kamera von CTA

Vorgelegte Master-Thesis von Ben Gebhardt aus Heidelberg

1. Gutachten: Dr. Richard White (MPIK)
2. Gutachten: Prof. Jim Hinton (MPIK)
3. Gutachten: Prof. Tetyana Galatyuk (TU DA)

Tag der Einreichung:

¹⁰
¹¹ **Abstract**

¹² Earth is continuously hit by high energy gamma radiation originating from outside our solar
¹³ system. This gamma radiation carries with it vast amounts of information about the most ener-
¹⁴ getic phenomenon in our galaxy and beyond. It delivers this information to Earth in the form
¹⁵ of a gamma ray induced particle shower in our atmosphere. While it is also possible to detect
¹⁶ those particles directly on the ground, traveling through Earth's atmosphere those particles emit
¹⁷ Cherenkov light. The path of the shower emits light that is shaped like a cone and this can
¹⁸ be detected by telescopes on the ground, who are able to reconstruct the path of the emitting
¹⁹ particles. With this information, besides energy and shape, the source in the sky of the gamma
²⁰ ray, that hit our atmosphere can be reconstructed.

²¹ One such experiment capable of observing gamma rays is the proposed Cherenkov Telescope
²² Array. It consists of over 100 telescopes grouped in three energy ranges. The instrument ob-
²³ serving at highest energies is able to use Silicon Photomultipliers for photon detection. Silicon
²⁴ Photomultipliers are semiconductors that attracted increased attention for their possible use in
²⁵ astroparticle physics. Each detected photon entering the detector is converted to a measurable
²⁶ signal through avalanche creation. Being a fairly new technology, they are continuously being
²⁷ developed, and finding the most promising candidate is a task spread across many groups.
²⁸ This work will conduct dark measurements of five proposed candidates. A teststand will be
²⁹ build and data acquisition and analysis code will be developed.



Abstract

worum es geht



33 List of Figures

35	1	Cosmic radiation	7
36	2	Fermi LAT	8
37	3	Cherenkov light cone	10
38	4	GCT and CHEC-M at Meudon	12
39	5	GCT optical system	13
40	6	CHEC focal plane	14
41	7	Structure and carrier multiplication through an avalanche inside a SiPM	16
42	8	Cherenkov light spectrum	18
43	9	Avalanche induced secondary effects	21
44	10	Teststand outside view	23
45	11	Thermal chamber inside view	24
46	12	Experimental setup scheme	25
47	13	Shaped versus unshaped signal	26
48	14	Zero pole cancelation	26
49	15	Multi p.e. persistence plot	27
50	16	Pulse height spectrum generated by the oscilloscope	27
51	17	Pedestal subtraction	30
52	18	Peak Detection	31
53	19	Fitted pulse area histogram	32
54	20	Regression line plots of 1p.e. and Δ p.e.	33
55	21	MPD parameter challenges and the integration window	35
56	22	MPD parameter challenges and the threshold	36
57	23	List of examined SiPM devices	38
58	24	CHEC-S SiPM	40
59	25	CHEC-S average pulse shape	40
60	26	CHEC-S gain	41
61	27	CHEC-S DCR	42
62	28	CHEC-S OCT	43
63	29	LCT5 6mm SiPM	45
64	30	LCT5 6mm average pulse shape	45
65	31	LCT5 6mm gain	46
66	32	LCT5 6mm DCR	47
67	33	LCT5 6mm OCT	48
68	34	LCT5 7mm SiPM	49
69	35	LCT5 7mm average pulse shape	49
70	36	LCT5 7mm gain	50

71	37	LCT5 7mm DCR	51
72	38	LCT5 7mm OCT	52
73	39	LCT5 LVR 6mm SiPM	53
74	40	LCT5 LVR 6mm average pulse shape	53
75	41	LCT5 LVR 6mm gain	54
76	42	LCT5 LVR 6mm DCR	54
77	43	LCT5 LVR 6mm OCT	55
78	44	SensL FJ60035 SiPM and average pulse shape	56
79	45	SensL FJ60035 gain	57
80	46	SensL FJ60035 DCR	57
81	47	SensL FJ60035 OCT	58
82	48	DCR device comparison	60
83	49	OCT device comparison	61
84	50	Comparison based on two proposed points of operation	63
85	51	PDE versus OCT comparison	64
86	52	CTA in Chile and the stereoscopic technique	69
87	53	Current IACT experiments	69
88	54	OCT dependency on the cell-size	70
89	55	Pulse area spectra of three different integration windows	73
90	56	S12642 pulse height and pulse area spectrum	74
91	57	LCT5 6mm pulse area spectrum	75
92	58	Breakdown-voltage versus temperature	76
93	59	Breakdown-voltage dependency	77
94	60	Full schematic of the shaper developed at the University of Leicester.	78
95	61	List of examined SiPM devices	79
96	62	CHEC-S pixel comparison of the gain	80
97	63	CHEC-S pixel comparison of the DCR	80
98	64	CHEC-S pixel comparison of the OCT	81
99	65	Description	82
100	66	Description	83
101	67	Description	84
102	68	Description	85

103 **Contents**

105	1 Cosmic Radiation	7
106	1.1 Air shower induced Cherenkov Radiation	9
107	1.2 Imaging Atmospheric Cherenkov Telescopes	10
108	2 Cherenkov Telescope Array	12
109	2.1 Gamma Cherenkov Telescope	13
110	2.2 Compact High Energy Camera	14
111	3 Silicon Photomultipliers	16
112	3.1 SiPM characteristics	16
113	3.2 Gain of a Silicon Photomultiplier	18
114	3.3 Thermally induced dark counts	20
115	3.4 Avalanche-induced secondary effects	20
116	3.5 Photon Detection Efficiency	22
117	4 Experimental Setup	23
118	5 Data Analysis	29
119	5.1 Tracefile Conversion	29
120	5.2 Pedestal Subtraction	30
121	5.3 Peak Detection	31
122	5.4 Gain Extraction	32
123	5.5 Analysis improvements	34
124	5.6 Data Challenges	35
125	6 Results	38
126	6.1 SiPM devices for CTA	38
127	6.2 Hamamatsu S12642-1616PA-50 50 μ m 3mm	40
128	6.3 Hamamatsu LCT5 50 μ m 6mm	45
129	6.4 Hamamatsu LCT5 75 μ m 7mm	49
130	6.5 Hamamatsu IVR 50 μ m 6mm	53
131	6.6 SensL FJ60035 6mm 35 μ m	56
132	7 Comparison	59
133	7.1 Dark Count Rate	59

¹³⁴	7.2 Optical Cross Talk	60
¹³⁵	7.3 Point of Operation Comparison	62
¹³⁶	7.4 Photon Detection Efficiency	62
¹³⁷	8 Conclusion and Outlook	65
¹³⁸	9 Glossary	66
¹³⁹	10 Bibliography	67
¹⁴⁰	11 Appendix	69

¹⁴¹ 1 Cosmic Radiation

¹⁴³ Cosmic rays consist of a single particle with energies from 10^{10} to 10^{20} eV and describes extra-
¹⁴⁴ solar charged particles arriving on Earth and hitting the atmosphere fig(1). The most energetic
¹⁴⁵ laboratory based accelerators operate in the 10^{12} eV energy range. They were discovered
¹⁴⁶ by V.F. Hess in 1912 during the famous balloon flight experiments. He aimed to measure the
¹⁴⁷ conductivity of air, that until then, was believed to be an insulator resulting in some problems
¹⁴⁸ regarding the discharge of an electrically charged body, no matter how well it was isolated from
¹⁴⁹ the ground. Hess found the air's conductivity to increase with higher altitude, concluding the
¹⁵⁰ presence of a large amount of ionizing radiation above the atmosphere.
¹⁵¹ Cosmic rays do not include those low energy particles originating from our sun. With a particle
¹⁵² energy up to 1 keV, those are referred to as solar wind, which means, by definition, cosmic rays
¹⁵³ arrive on Earth from outside our solar system. They consist of 87% protons, 12% α -particles
¹⁵⁴, 1% heavier nuclei and some electrons. High energy cosmic rays hitting Earth are very rare,
¹⁵⁵ averaging to one per year in an area of one square kilometer. Except at those very high ener-
¹⁵⁶ gies ($>10^{18}$ eV) cosmic rays will not reach earth directly and can not be observed to pinpoint
¹⁵⁷ their source. Traveling through the interstellar medium, they get scattered by the interstellar
¹⁵⁸ magnetic fields, the cosmic microwave background and other hindrances and therefore have
¹⁵⁹ lost all directional information. However, directly observable cosmic rays, for example at the
¹⁶⁰ Pierre-Auger Observatory, provide an insight into cosmic particle accelerators.[2]

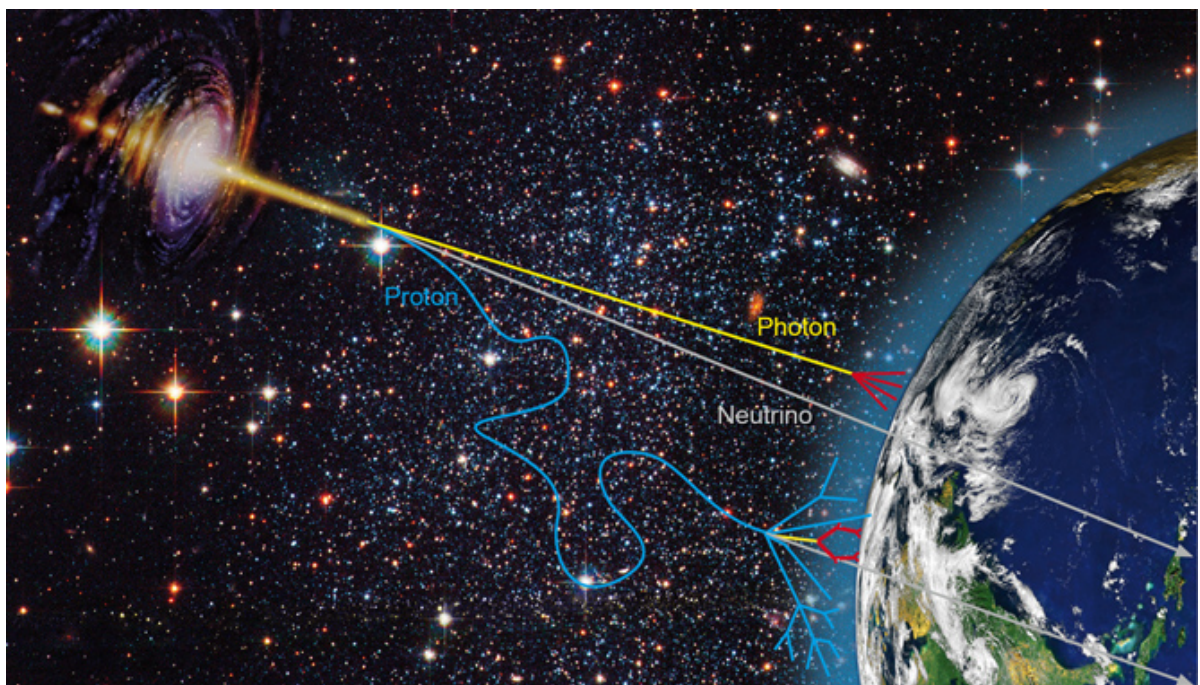


Figure 1: Gamma radiation photons (yellow) and scattered cosmic ray protons (blue) from an astrophysical source arriving on Earth. Neutrinos (grey) mostly do not interact. Picture from [26]

161 Cosmic rays of the higher energies are therefore observed via a detour: Gamma radiation.

162

163 Gamma radiation cannot be generated by
164 thermal emission of hot stellar objects, the
165 only event with a high enough temperature
166 to produce thermal radiation in the range
167 of GeV and TeV gamma radiation would be
168 the big bang, there is and has been nothing
169 else in the known universe. If thermal
170 radiation reflects the temperature of the
171 emitting body, what do gamma rays tell
172 us?



Figure 2: FermiLAT Picture from [27]

173
174 Gamma radiation probe a non-thermal universe.
175 In this other mechanisms are needed to concentrate large amounts of energy into a
176 single quantum. The possible emission mechanisms are outlined below.

177 There are many diverse mechanisms of emitting gamma radiation. Gamma rays are generated
178 by high relativistic particles, in a first step for example: accelerated by the shockwave of a super-
179 nova explosion. Those cosmic rays then collide with ambient gas, interact with photons or
180 magnetic fields, by inverse compton scattering, emitting high energy photons in a down-top
181 fashion. Very-high-energy (VHE) gamma radiation is defined as gamma radiation in the energy
182 range of 10^{11} to 10^{14} eV.

183

184 One such source of VHE gamma radiation and also the most famous, because the first to be
185 discovered, lies within the Crab Nebula. The Neutron Star located inside the Crab Nebula is a
186 Pulsar and the remnant of Supernova1054 and steadily emits gamma radiation energies up to
187 80 TeV. Another compound of the gamma radiation here is the so called Pulsar Wind Nebula. It
188 is composed of highly relativistic charged particles from the Pulsars giant rotating magnetic field
189 interacting with the expanding Supernova remnant via inverse compton scattering. Supernova
190 shockwaves themselves can also drive atomic nuclei to high energies which in turn emit observ-
191 able gamma-rays in a top-down fashion. Additionally, binary systems consisting of a black hole
192 or pulsar orbiting a massive star can emit a flow of high-energy particles with varying intensity,
193 based on the elliptical orbit, where particle acceleration conditions vary.

194 So just like thermal radiation reflects the temperature of the emitting object, the flux and en-
195 ergy spectrum of the gamma rays reflect the flux and spectrum of the high energy seed particles,
196 coming from the source. So they can be used to trace these cosmic rays and electrons in distant
197 regions of our own galaxy or even beyond. [1]

198 One surprise was the discovery of so called "dark sources" , objects emitting VHE gamma-rays,

199 but have no counterpart in other wavelengths, meaning those objects might only be observable
200 through gamma-rays. In extragalactical regions, gamma rays provide information on active
201 galaxies, where a constant stream of gas feeds a supermassive black hole at the center, releasing
202 enourmous amounts of energy. From there, gamma rays are believed to be emitted, giving insight
203 into one of the most violent but to date poorly understood environments in our universe.

204 Even higher energy gamma rays could also be the product of decays of heavy particles, like
205 dark matter or cosmic strings. They therefore also provide a window to the discovery of dark
206 matter.

207

208 Gamma Radiation carries unique information about the most energetic phenomena in our
209 universe. The only problem is, our atmosphere is opaque for gamma radiation, gamma ray as-
210 tronomy in the lower energies is done by satellite based instruments like FermiLAT. The Large
211 Area Telescope, the principle scientific instrument on the Fermi Gamma-Ray Space Telescope
212 Spacecraft sensitive in the energy range between 20 MeV and 100 GeV, launched in June 2008
213 fig(2). To reach the higher energy range through space based telescopes is very inconvenient,
214 since the required mass the telescope active area would need to detect the gamma rays increases
215 with gamma ray energy, and can therefore by very expensive to launch into space. Low energy
216 gamma rays can be efficiently captured by a volume appropriate for a spacecraft, for higher en-
217 ergy gamma rays using other interaction and detection media, like water or Earths atmosphere,
218 is more viable.

219 **1.1 Air shower induced Cherenkov Radiation**

220 The effect of gamma radiation on Earth is visible through gamma-ray induced particle cascades.
221 When a primary particle, i.e. a gamma photon or cosmic ray enters the atmosphere and collides
222 with a nucleus of the air, it gets scattered and creates secondary electrons, positrons and pho-
223 tons. Those secondary particles also interact with the atmosphere creating a cascade of particles
224 called a particle shower.

225 In this air shower, the initial and each subsequent particle traveling through our atmosphere
226 emitts Cherenkov light. Cherenkov radiation is a phenomenon caused by charged particles trav-
227 eling faster than the local speed of light would allow in that medium. This light is emitted in a
228 narrow cone with an increasing angle as the particles travel downward. This Cherenkov light
229 shows as a very short ($\sim 5\text{ns}$) flash with a peak in the UV-spectrum at around 330nm. Thus,
230 we can image the particle cascade measured with the telescope and can reconstruct the direc-
231 tion and energy through a stereoscopic image of the shower taken by multiple telescopes (see
232 section(A)), reconstructing the position of the source in the sky. Is is also possible to recon-
233 struct the energy of the original photon from the amount of light produced, because energy is
234 conserved, so all energy of the original photon is now distributed between the particles of the
235 shower.

237 To determine whether it is a hadronic shower, originating from cosmic rays, or a gamma shower,
238 originating from gamma ray photons, the shape of the shower and so called Hillas parameters
239 are used to determine the difference.

240 1.2 Imaging Atmospheric Cherenkov Telescopes

242 The technique, pioneered by the Wipple Collaboration
243 behind the ground based experiments called
244 Imaging Atmospheric Cherenkov Telescope (IACTs)
245 aims at measuring the time, direction and en-
246 ergy of flashes of Cherenkov light from exten-
247 sive air showers caused by VHE gamma radia-
248 tion.

249 Those ground based instruments have a much larger
250 effective detection area than any satellite based in-
251 strument, which have a typical detection size of
252 1m^2 . The range of the Cherenkov flash being be-
253 tween 300-600nm, current generation Silicon Photo-
254 multipliers (SiPMs) are a promising candidate to re-
255 place the progenitor photon detector used in previ-
256 ous experiments like HESS, the Photomultiplier Tube
257 (PMT).

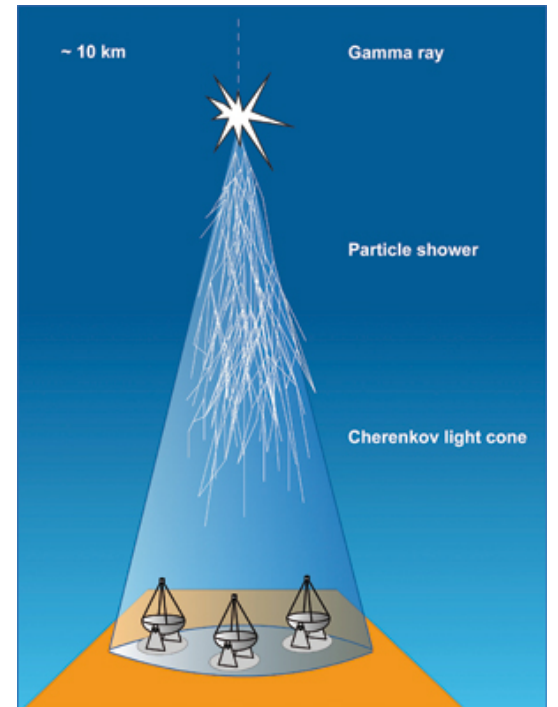


Figure 3: The cone of Cherenkov light emitted by an extensive air shower. Picture from [28]

259 Current ground based IACT experiments are HESS,
260 MAGIC and Veritas. (see section(B)) HESS¹, based in
261 Namibia, consists of four telescopes the size of 12 m
262 operating in the energy range of 3 GeV to 100 TeV. The chosen name is in honor of Victor Hess,
263 the first to discover cosmic rays. The recent HESS upgrade added a fifth larger telescope in the
264 center of the array with a mirror diameter of 28 m. MAGIC², based in La Palma one of the
265 Canary Islands, is a system consisting of two 17 m diameter telescopes at 2200m asl³, covering
266 the energy range 30 GeV and 30 TeV. Veritas⁴, operating between 50 GeV - 50 TeV consists of
267 four 12 m telescopes, based in Arizona, USA.

268
269 Due to the limited effective area, caused by the number of telescopes spread over a wide
270 area, most cascades are viewed by only 2 or 3 of the telescopes. Additionally, due to the low
271 flux of VHE gamma radiation, detectors for this energy range are spread over a large area, mak-

¹ High Energy Stereoscopic System

² Major Atmospheric Gamma Imaging Cherenkov Telescopes

³ above sea level

⁴ Very Energetic Radiation Imaging Telescope Array System

272 ing space based instruments, which detect the incident gamma ray, an inconvenient and costly
273 choice.

274

275 Another detection concept for VHE gamma radiation are ground based air shower particle
276 detectors such as the High-Altitude-Water-Cherenkov observatory (HAWC) [6]. It employs a
277 similar detection principle, recording shower particles reaching arrays of ground based particle
278 detectors filled with water as detection medium, in contrast to air in IACTs. Those have the
279 advantage of a larger duty cycle than IACTs, as they are able to operate during the day. Their
280 limited sensitivity even with high observation time however will not allow them to compete
281 with the sensitivity and resolution of IACTs such as in the CTA. The array will however be able
282 to provide useful complementary information.

2 Cherenkov Telescope Array

The Cherenkov Telescope Array, CTA, is a proposed ground-based observatory array of many tens of telescopes distributed over a larger energy range than before. It will allow detection of gamma rays over a large area on the ground and from multiple different directions. The array will consist of 60 - 100 telescopes of different designs and sizes to cover the aimed for energy range and area. Science goals of CTA are the understanding of cosmic rays and their role in the universe, including the study of cosmic particle accelerators, such as pulsars, pulsar wind nebulae , supernova remnants and gamma ray binaries. Secondly particle acceleration around black holes of supermassive or stellar size and lastly physics beyond the Standard Model. There are currently three groups of telescopes planed, differing in their size and achievable energy range:[2]



Figure 4: The prototype GCT Structure with mounted CHEC-M at the Observatory at Meudon, Paris, one of the telescopes of CTA.

1. LST⁵ The low energy instrument, between 20 and 200 GeV, is a 23 meter class telescope with a moderate field of view (FoV) of the order of about 4.5°.
 2. MST⁶ The medium energy range, from around 100 GeV to 10 TeV, is covered by a telescope of the 12 meter class with a FoV of 7°.
 3. SST⁷ The high energy instrument, operating between a few TeV to 300 TeV, is a 4 meter telescope with a FoV ranging from 9.1° to 9.6°.
- There are currently two sites planed, which when deployed, will achieve full-sky coverage. The southern site in the Atacama Desert in Chile, one of the most driest and isolated regions on Earth, will consist of four LSTs, 24 MSTs, and about 70 SSTs covering an area of 4 km². The

⁵ LST large sized telescope

⁶ MST medium sized telescope

⁷ SST small sized telescope

316 northern site will only cover 0.4 km^2 and will only contain four LSTs and 15 MSTs due to spac-
317 ing reasons with the MAGIC observatory at the same location at the Roque de los Muchachos
318 Observatory on La Palma, one of the Canary Islands.

319
320 One proposed concept for the SST is the Gamma Cherenkov Telescope (GCT) fig(4).
321

322 **2.1 Gamma Cherenkov Telescope**
323

324 The reflector design of IACTs traditionally consists of multiple mirror segments, which focus the
325 incident light onto a camera covering $\sim 1 \text{ m}$ with pixels $1'' - 1.5''$ in diameter. Such a reflector
326 design is proposed for both, the LST and the MST of CTA resulting in the telescope sizes men-
327 tioned in section(2) above, that will use the traditional PMTs.

328 For the SST such a design would result in a cheap telescope structure, but a disproportionately
329 expensive camera, i.e. the cost and size of the structure is reduced, while the cost of the camera
330 is not. The cost of one SST camera would be near the cost of a MST camera, which given the

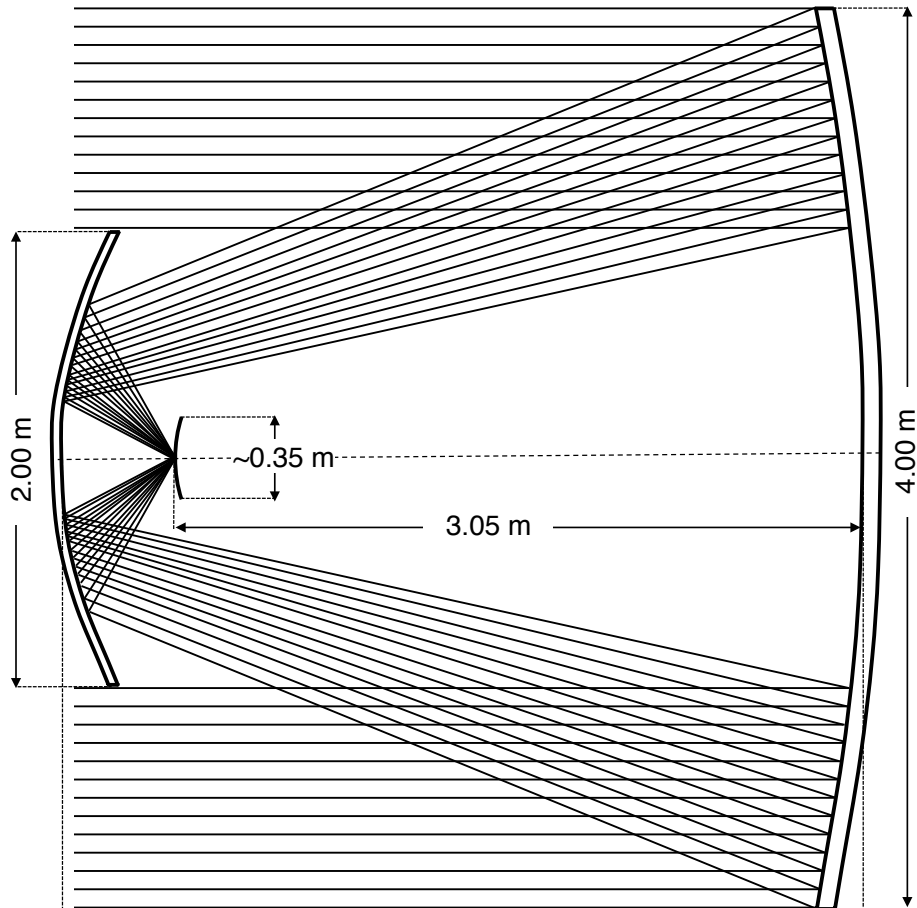


Figure 5: Optical mirror system of the GCT telescope. A primary(4 m)-secondary(2 m) mirror optics system focuses the light onto a 0.35 m camera focal plane.

331 number of SST telescopes at the southern site is sub-optimal.
 332 The alternative solution is the reduction of the camera plate scale through a dual-mirrors de-
 333 sign allowing the use of more affordable photosensors. The optical system of the telescope is
 334 complemented with a secondary mirror added to the primary mirror. This shortens the effective
 335 focal length so the focal surface will lie between primary and secondary mirror fig(5). This
 336 optical design is based on the Schwarzschild-Couder design first produced by Karl Schwarzschild
 337 (Schwarzschild, 1905) and later refined by Couder (Couder, 1926) and then adapted for use in
 338 IACTs by Vassiliev and Fegan [10]. With the dual-mirror design optimised for GCT by Blake et
 339 al. [11] the camera plate scale is reduced, allowing the use of more affordable photosensors,
 340 Silicon Photomultipliers (SiPMs) and multi-anode photomultiplier tubes (MAPMs) among them,
 341 potentially reducing the cost of each SST.

342 **2.2 Compact High Energy Camera** 343

344 The Compact High Energy Camera, or CHEC fig(6) is one of three prototype camera concepts in
 345 development for one of the SST structures within CTA. One camera features 2048 photosensors,
 346 building equally many readout channels per camera. The readout is done by so called TARGET⁸
 347 modules for sampling, digitization and triggering, one of those consists of 4 ASICs⁹ with 16
 348 channels each. The camera houses 32 TARGET modules, one of them responsible for readout
 349 of 64 photosensors. The TARGET modules build the front-end of the integrated electronics¹⁰
 350 inside the CHEC camera connecting the buffer to the cameras backplane. After the photosensor

⁸ TARGET TeV Array Readout with GS/s sampling and Event Trigger

⁹ ASIC Application Specific Integrated Circuit

¹⁰ FEE front end electronics

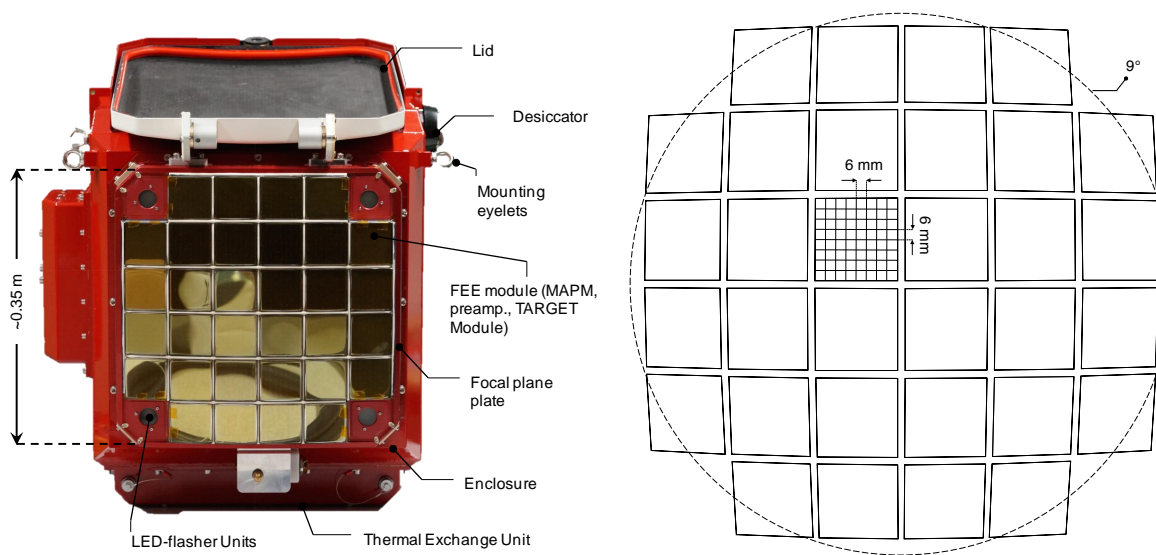


Figure 6: Front view of the CHEC-M prototype (left), view of the camera focal plane. Schematic of the focal plane (right), illustrating the 9° FoV with 6 mm pixels. Pictures from [18]

351 is triggered the buffer amplifies the signal, that is then send to the ASIC inside the TARGET
352 modulde, where an analog-to-digital converter and a shaper convert the signal before it is send
353 to the backplane for transfer to the main array hub. Two iterations of the CHEC camera are
354 tested, CHEC-M is the first design based on MAPMs as photosensors and was the initial proto-
355 type platform all improvements to the electronics are tested on. CHEC-M since then moved to
356 Meudon in Paris and is now mounted on the GCT structure for further testing of the entire GCT
357 prototype. The second iteration of the camera: CHEC-S, based on SiPMs as photosensors is a
358 similar concept, with applied improvements to electronics and mechanical design. The two cam-
359 eras are very similar in shape and can both be mounted on the GCT structure without alterations.

360

361 In order to make an educated choice on the best SiPM candidate to use to populate the camera
362 focal plane of the camera, an in-depth characteristic study on pulse-shape, gain, temperature-
363 dependence, detection efficiency, thermal noise and correlated secondary effects is conducted
364 by multiple groups within the CTA collaboration.

365

366 This work studies the gain, noise from thermal, as well as correlated secondary effects and
367 their temperature dependence.

3 Silicon Photomultipliers

368 Silicon Photomultipliers (SiPMs) are semiconductor photo detectors, that have attracted in-
369 creased attention over the last decade for their possible use in astroparticle physics. The sensor
370 consists of an array of avalanche photo-diodes, typically $\sim 50 \mu\text{m}$ in size. Depending on the
371 pixel-size, one pixel contains several 1000 diodes, hereafter called cells. Each cell is a PN junc-
372 tion fig(7) supplied with a reverse bias-voltage above breakdown, which is called operation in
373 Geiger-mode, in analogy to the Geiger counter. In this mode, a photon or thermal excitation will
374 produce an electron-hole pair in the depleted region. Through impact ionization these charge
375 carriers will in turn trigger an avalanche in a cell, which in turn generates a large output pulse
376 typically in the range of several Mega electronvolt. This avalanche is then passively quenched
377 by a resistor to limit the current in the substrate and to reset the cell to a quiet state so it is
378 photosensitive again. The signal of the SiPM is the sum of the signal of all cells, read out over
379 their quenching resistor via a common output.
380
381

3.1 SiPM characteristics

383 SiPMs posses major advantages over their progenitor, the Photomultipliertubes, or PMT. They
384 are more resistent to mechanical and accidental light-exposure damage through ambient light.
385 Single SiPM cells have a lower power consumption, but more SiPM cells are needed to cover the
386 same space as a PMT. Operating at a much lower bias-voltage, there is no need for high-voltage
387 as in PMTs. They di require more They posses a high photon detection efficiency and are in-
388 sensitive to magnetic field changes. There is rapid improvement, being a fairly new technology,
389 with new generations every ~ 5 months and decreasing costs per mm^2 . Viewed over all cells

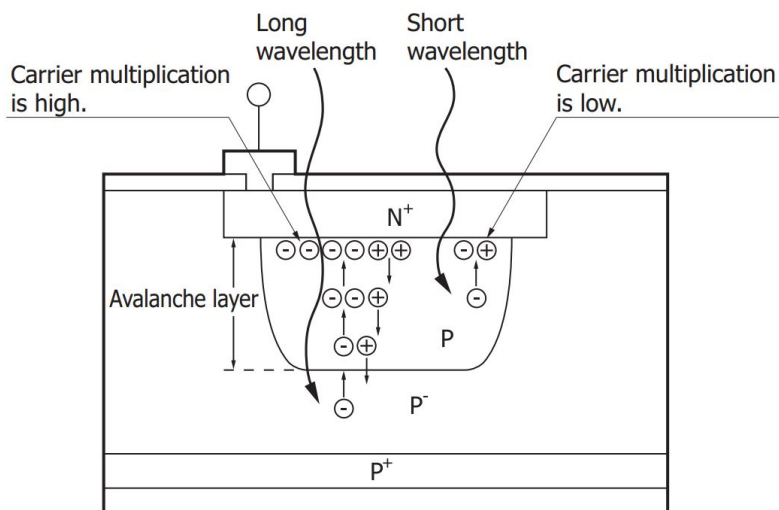


Figure 7: Structure and carrier multiplication through an avalanche inside a SiPM. Picture from [16]

392 of the whole pixel, fluctuations in the gain are very small. This is because of the uniformity
393 during manufacture and visible in the width and the clear resolution of the p.e. peaks in the
394 pulse area spectrum. See section(E) for examples. MAPMs on the other hand posses larger
395 gain fluctuations, which is due to their structure. These make SiPMs an interesting candidate
396 in astrophysics experiments for both, space- and ground-based telescopes (like IACTs). How-
397 ever SiPMs also posses drawbacks, one of which is their temperature dependence through their
398 gain and Dark Count Rate (DCR). Another source of worry is their Optical Cross Talk (OCT),
399 although manufacturers advance to reduce this source of noise.

400

401 Advantages:

- | | |
|---|---|
| 402 1. Sturdiness | 409 5. No need for HV as in PMTs |
| 403 2. May be exposed to ambient light (obser-
410 vation during bright moonlight periods
411 possible) | 412 6. High Photon detection efficiency |
| 406 3. Low power consumption ($\leq 50\mu\text{W}/\text{mm}^2$) | 413 7. Insensitivity to magnetic fields |
| 407 4. Low operation voltage (typically ~ 20
414 100 Volts) | 415 8. Being a fairly new technology it is
416 steadily improved, meaning a new gen-
417 eration of SiPMs every 5months |
| | 418 9. Rapidly decreasing cost per mm^2 |

416 Drawbacks:

417

- 418 1. temperature dependence of gain and DCR
419 2. Noise through OCT
420 3. cost per mm^2 larger than PMTs

421

422 There is a multitude of desired attributes of SiPMs by CHEC, and CTA in general, among them is
423 a high enough fill-factor (detector space versus dead space) to guarantee high Photon Detection
424 Efficiency (PDE) (section(3.5)). The PDE quantifies the absolute efficiency of any photon detec-
425 tor to absorb a photon and produce a measurable signal at its output. To achieve a high PDE in
426 the 400 nm regime, the design moves to very thin implantation layers on the surface in order
427 to minimize the absorption of shorter wavelength photons in insensitive areas fig(??). Different
428 entry window coatings and avalanche structures explore the capable enhancements in the blue
429 sensitive UV region.

430 The peak of the spectral response of the SiPM is desired to be around the spectral peak of the
431 Cherenkov light at ~ 400 nm and at the same time, must have a fast enough drop to ensure less
432 Night Sky Background (NSB) pick up (fig(8)). The overall noise from thermal and correlated
433 secondary effects, like cross-talk, of the SiPM must be sufficiently below the expected NSB rate
434 at the location (usually around $\sim 20\text{-}80$ MHz[9]). It is common practise to compare those two
435 characteristics directly to showcase the behavior of the PDE versus OCT. A point of low cross-

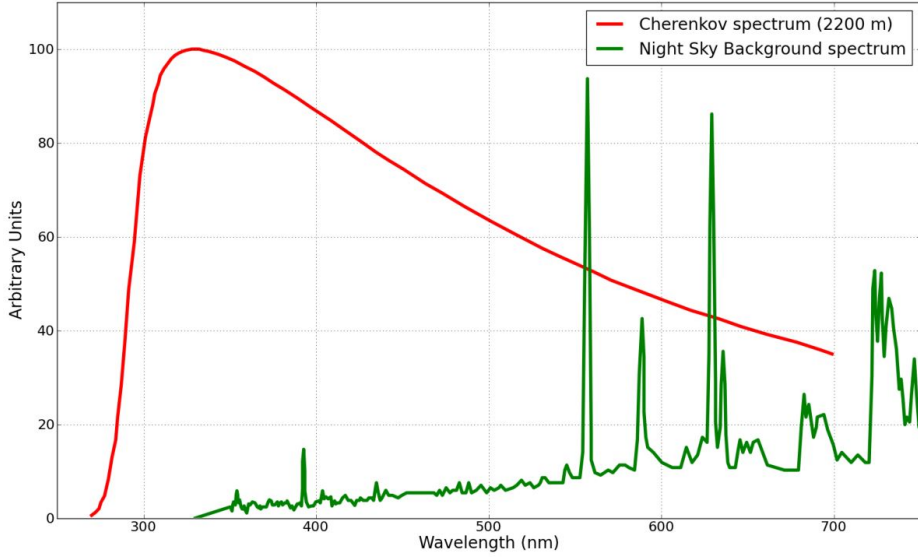


Figure 8: The spectrum of Cherenkov light observed from an extended air shower at 2200m asl. compared to the expected NSB measured in La Palma. Cut-off of the spectrum at wavelengths below ~ 300 nm due to atmospheric absorption. The emission peaks above ~ 550 nm in the NSB spectrum are mostly attributed to atomic oxygen, hydroxide and sodium in the atmosphere. Units on the y-axis are arbitrary because NSB and Cherenkov light vary by different parameters. There is a region between 550 and 650 nm, where the average Cherenkov light spectrum across the focal plane and contributions from the NSB overlap. Image from [9]

436 talk, where the PDE is still at maximum is desired.

437 Another important characteristic is the temperature dependence of the gain. While the CHEC
438 camera is observing, the preferred fluctuation of the gain is below 10%. The camera focal plane
439 underlies temperature shifts during operation, which will be slightly countered by cooling the
440 photosensing area. Despite that the focal plane will still be warming up, so a lower gain depen-
441 dence on temperature is desired in order to minimise the gain fluctuations.

442 **3.2 Gain of a Silicon Photomultiplier**

444 The gain of a SiPM measures the internal conversion of a photon incident into a signal at the
445 output. The amplification of the device is expressed as the average number of charge carriers
446 produced. There is no distinction whether the incident was caused by a single original photon
447 or a thermal electron. The gain (M) (eq 1) of a SiPM results from the deposited charge (Q)
448 of the pulse generated from one cell when it detects one photon, divided by the charge per
449 electron (e). The charge deposited per event is proportional to the cells capacitance (C) and

450 the supplied over-voltage ($V_{bias} - V_{breakdown}$).[9] This results in the gain (M) in units of total
451 number of charge carriers, usually in the several 10^6 range.

$$M = \frac{Q}{e} \quad (1)$$
$$Q = C \times (V_{bias} - V_{breakdown})$$

452 Estimation can be done via the voltage mean of the 1 p.e. amplitude: (e.g. see figure(25)).
453 For a better understanding, stating the gain in units of mV per photoelectron or mV/p.e. is
454 more suitable, as it gives a direct correlation between detected photoelectron and expected
455 voltage amplitude. Given the very narrow pulse shapes, using the average pulse amplitude and
456 extracting FWHM as a time measure of the total charge flowing during discharge and using the
457 formula (eq 2):

$$Q(p.e.) = C \times (V_{bias} - V_{breakdown}) \quad (2)$$
$$U(p.e.) = \frac{Q(p.e.)}{t(FWHM)} \times 50\text{ohm}$$

458 Resulting in the expected event charge flowing during capacitor discharge. Given the bias-
459 voltage and C as capacitance of one cell and the resistance (50ohm) of the quenching resistor, a
460 conversion factor and the average amplitude per photoelectron can be extracted.
461

462 The gain is obviously higher the larger the cell capacitance or the higher the bias-voltage
463 (eq 1) will be. But increasing the bias-voltage also increases dark counts and crosstalk. The
464 gain is also dependent on the temperature, mainly through the quenching resistor but also from
465 the silicon bulk itself, at a certain bias-voltage decreasing as temperature rises. The quench-
466 ing resistor is affected by a lowering of the electrical conductivity with rising temperature, in
467 accordance to the Wiedemann-Franz law, stating that the ratio of electrical and thermal con-
468 ductivity remains constant. The silicon bulk at rising temperatures underlies increased crystal
469 lattice movement. This impinges charge transport by increasing the probability that carriers
470 might impact on the lattice before the carrier energy has become large enough for continued
471 ionization. In order to counteract this, the electric field must be increased by increasing the sup-
472 plied bias-voltage so ionization is more likely. Doing this has drawbacks as discussed before. For
473 application as a photon detector, keeping the gain constant is an inevitable step, otherwise the
474 shifting gain leads to problems. To do that, either the bias-voltage need to be adjusted to match
475 ambient temperature, leading to problems with varying dark counts and crosstalk. Or the sur-
476 face temperature must be regulated to be kept constant. Although more challenging hardware
477 would be required, the latter option has obvious advantages, keeping dark counts and crosstalk
478 and more important the gain constant by simply regulating the surface temperature.

479 Taking into account equation 1, it appears that the breakdown-voltage can be estimated from
480 the zero-crossing of a linear extrapolation of the gain at every bias-voltage per temperature. By
481 doing this a linear breakdown-voltage dependence of the temperature can be observed. See
482 section(F)
483 When parametrized over over-voltage, the gain is essentially temperature independent.
484 For gain measurements see section(6).

485 3.3 Thermally induced dark counts

487 Inside the SiPMs depleted region a dark pulse originates from thermal excitation of an electron
488 to the conduction band. Without an event photon present to trigger the avalanche, it is still
489 indistinguishable from a photoelectron pulse. These thermally generated carriers are observed
490 along with the signal from a real photoelectron, presenting an irreducible source of noise. The
491 number of dark pulses observed is referred to as dark counts and the number per second as the
492 Dark Count Rate. For applications that need to operate in an environment with low noise, those
493 dark counts are a concern. In IACT application of SiPMs however, this is only a minor problem,
494 since IACTs operate in a naturally noisy environment. Even though sky darkness is one of the
495 prime criteria of the proposed site selections for CTA, the surrounding NSB at the most darkest
496 side in Chile will still exceed any random noise in the detector. The pollution of those NSB pho-
497 tons is unavoidable noise and will essentially limit the low energy resolution of the telescope to
498 the NSB rate. As long as any random noise, being dark counts or other, is significantly below
499 the NSB rate, it will not affect the telescopes performance.

500 Telescope performance simulations of the Schwarzschild-Couder MST of CTA at the site of
501 Chilec showed a rate of $\sim 20 - 80$ MHz per pixel for one of the older SiPM iterations from
502 Hamamatsu.[9] This is purely for NSB photons and pixels with a size of 6×6 mm², the cov-
503 ered range originates from differences in illumination level of the night sky by galactic- and
504 extragalactic-fields.

505 3.4 Avalanche-induced secondary effects

507 An avalanche originating from the primary cell can sometimes, either directly or by reflection,
508 propagate outside the cell and trigger an avalanche almost simultaneously in a secondary cell.
509 This will, unless accounted for, degrade the SiPMs photon counting resolution, since the sig-
510 nal will be a merge of cross-talk cells and real incident cells. This effect is referred to as the
511 OCT, since it is conveyed via secondary photons generated in the primary avalanche. Afterpuls-
512 ing also falls under this category, with the main difference to cross-talk being that the carrier
513 triggers a secondary avalanche in the primary cell, basically generating a parasitic pulse inside
514 the previously fired cell. Contained in a single cell, afterpulsing increases the measured charge
515 registered for an incident photon. The difference in arrival time of the secondary avalanche dis-
516 tinguishes different components comprising the cross-talk and afterpulsing. Those secondary

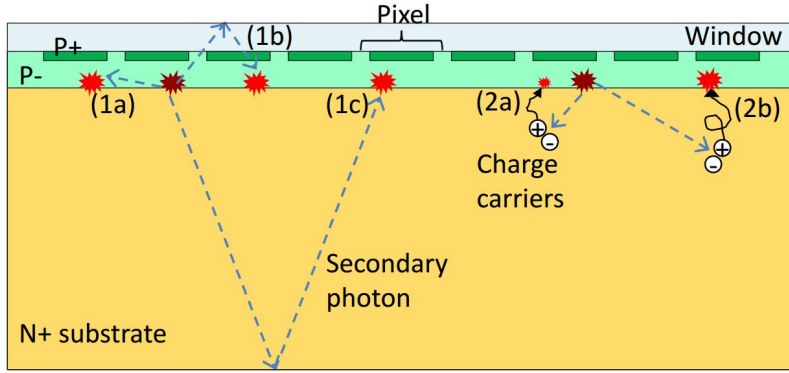


Figure 9: Secondary effects (bright red) caused by primary avalanches (dark red) in a Silicon Photomultiplier. In this work a single pixel, in this figure, is referred to as a cell (see section(3)). Everything labeled under 1 is associated with prompt cross-talk, afterpulsing labeled as 2a, and delayed cross-talk labeled as 2b. Image adapted from [13]

avalanches can again emit photons, that can trigger secondary avalanches themselves, leading to high amplitudes, even in dark conditions. Cross-talk is dependent on the ability of the secondary photons to reach a neighboring cell. This means, that an increase in cell-size and therefore cell-area should directly correlate with the OCT of a pixel. The OCT dependency on the cellsize was tested and can be found in section(C).

Figure(9) shows different physical processes causing secondary effects in SiPMs based on their delay time. Cause of the delay time is the dependence on the penetration depth of the incident photon, or the region the dark count generated, and the diffusion time inside the substrate. At long delay times of up to 70ns afterpulsing and cross-talk are not distinguishable.[13] The prompt OCT happens basically simultaneous to the primary avalanche, since it is unaffected by the primary cells recovery time and is labeled 1 in Figure(9). It is either triggered by the secondary photon directly (1a) reaching the neighboring cell, or after first reflecting on the surface layer (1b) or the bottom surface (1c). If the cross-talk avalanche delay time is shorter than the detection resolution, the difference in signal between an OCT event or an incident photon being detected, is not observable.

Time delayed OCT is caused by a carrier generated in the non-depleted substrate diffusing to a neighboring cell and triggering an avalanche in the depleted region (2b). If the carrier stays in the primary cell, the triggered avalanche is labeled afterpulsing (2a) and will have a lower amplitude, due to the cell not being recovered yet. The delay time is influenced by how deep the carriers are being trapped in the substrate, the time they need to diffuse to the surface, and also distinguished by traps with different lifetimes.

This is very important in IACT performance, since this effect gives random NSB and dark count photons the ability to rise to larger amplitudes. The consequent need to raise the trigger threshold to counteract the resulting rising accidental-triggerate has a negative impact on the low

541 energy resolution of the telescope.

542

543 Parametrized with over-voltage, the secondary avalanche effects are temperature indepen-
544 dent, for OCT measurements see section(6).

545 3.5 Photon Detection Efficiency

$$PDE = \frac{N_{detected\ photons}}{N_{total\ photons}} \quad (3)$$

547 The Photon Detection Efficiency is the probability of a detector to absorb an incoming pho-
548 ton and produce a measurable signal at its output, and depends on a number of factors. First
549 the photon must enter the depleted region via transmission through the surface of bare sili-
550 con, which has a reflectivity of 30%. However, the transmission probability can be improved
551 by coating the surface with a substrate with adequate thickness and a refraction index between
552 air $\eta_{air} = 1$. and silicon $\eta_{silicon} = 3.4$. Devices presented in this work are coated with epoxy,
553 a silicon resin and glass. The coating also has the added benefit of insulating and protecting
554 the cells against environmental influence. A possible negative effect of coating is an increase in
555 prompt cross-talk and a larger dependency of the overall cross-talk on the cellsize. The second
556 factor is quantum efficiency, describing how susceptible the depleted region is to photons ex-
557 citing electrons from the valence band to the conduction band. This is sometimes referred to as
558 spectral response of a detector to reflect the wavelength dependence of a detector and makes
559 the PDE wavelength dependent. The over-voltage dependency of the PDE is conveyed by the
560 third factor, the avalanche probability. It depends on the electric field present, and thus on the
561 applied over-voltage. The last factor is the fill-factor: the more the surface area of the detector
562 is covered with active-area cells and the less dead-area exists between cells the higher the fill-
563 factor is.

564 The Photon Detection Efficiency is commonly measured by illumination of the pixel and a cali-
565 brated reference photodiode with a flashing light source, and determining the average number
566 of photons hitting the photosensor during a light pulse.

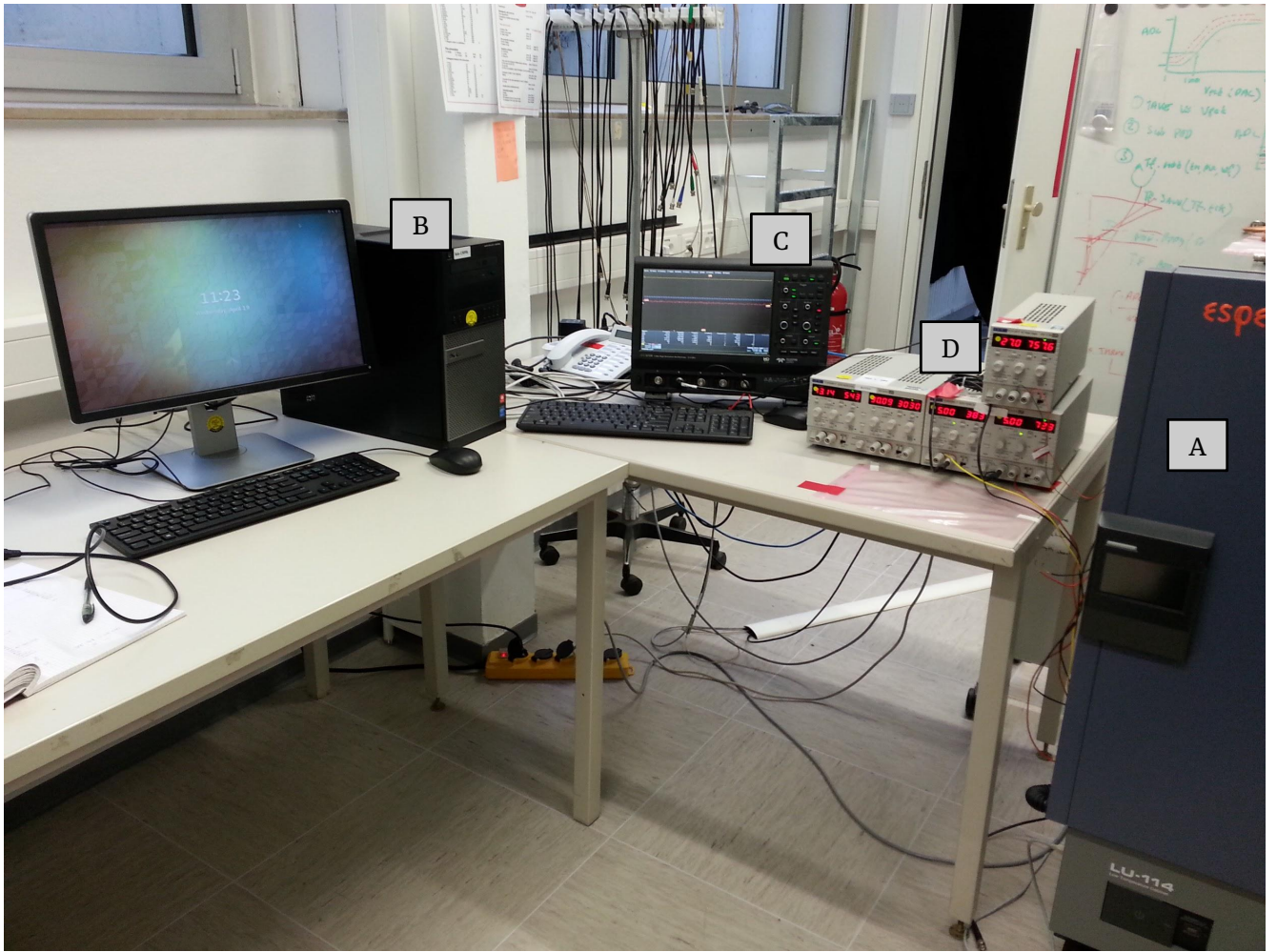


Figure 10: Outside view of the teststand with the ESPEC LU-114 thermal chamber (A), the Lab-PC (B), the Lecroy HD6104 oscilloscope (C) and the TTi power supplies (D).

567 4 Experimental Setup

568 The experimental setup in general is designed to house a variety of SiPM devices. Over the
 569 course of this work, 5 different types of SiPMs were mounted on the setup and evaluated. It
 570 involves a thermal chamber fig(12)(A) for temperature regulation which proved light tight and
 571 thus also serves as a dark box, to prevent any stray light to reach the SiPMs surface. The thermal
 572 chamber in question is a LU-114 constant climate cabinet from ESPEC with a programmable in-
 573 terface for remote control. The chamber is able to raise and lower the inside temperature with a
 574 $\pm 0.5^\circ\text{C}$ accuracy, direct measurements of the SiPMs surface with a temperature probe confirmed
 575 this. In the absence of light tests, heating of the SiPM surface through the dark current proved
 576 no concern.

577 Depending if the SiPM fig(12)(A1) in testing is pre-manufactured on a test-array or supplied as
 578 a standalone chip, it is either mounted directly on a mechanical arm inside the chamber in the
 579 former case, or in the latter the mechanical arm supports a specifically designed PCB connecting

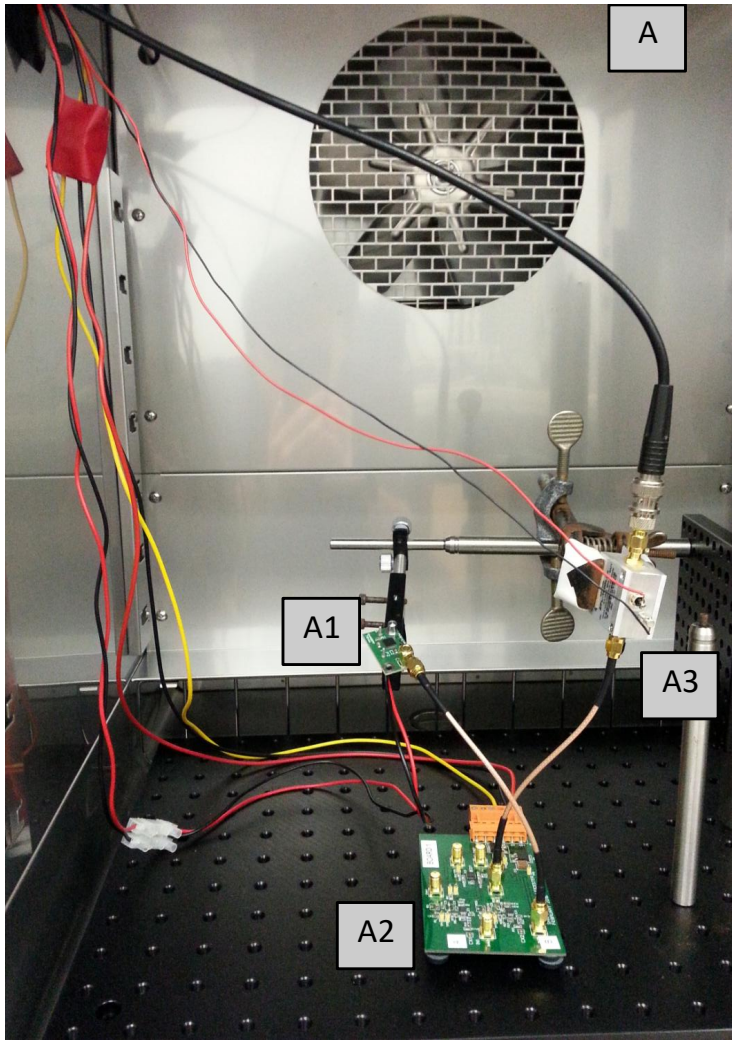


Figure 11: Inside view of the thermal chamber (A), with the SiPM (A1), the shaping electronics (A2) and the MiniCircuits PreAMP (A3). Signal throughput in the top left corner.

581 to the device. Via the mount, bias-voltage is supplied and signal is transferred to the shaper
 582 fig(12)(A2). In some cases the output signals amplitude is too low to trigger the oscilloscope,
 583 therefore amplification is needed. I used an amplifier from MiniCircuits fig(12)(A3) supplied
 584 with different voltages depending on the tested device to amplify the shaped signal.
 585

586 Data acquisition in the Laboratory is realized by a Lab-PC fig(12)(B), that forms the central
 587 control station for multiple pieces of equipment. It is connected to the oscilloscope fig(12)(C),
 588 which records the waveforms of the device in testing, and then sends the data back to the PC
 589 via ethernet. The oscilloscope is a Lecroy HDO6104 1GHz HS Oscilloscope capable of 2.5 GS/s.
 590

591 The power supplies fig(12)(D) control the bias-voltage of the SiPMs, ramping of the bias-voltage
 592 is controlled by the PC. Lastly the thermal chamber is connected to the Lab-PC, where the data
 593 acquisition script controls the temperature, and continuously rechecks it during temperature

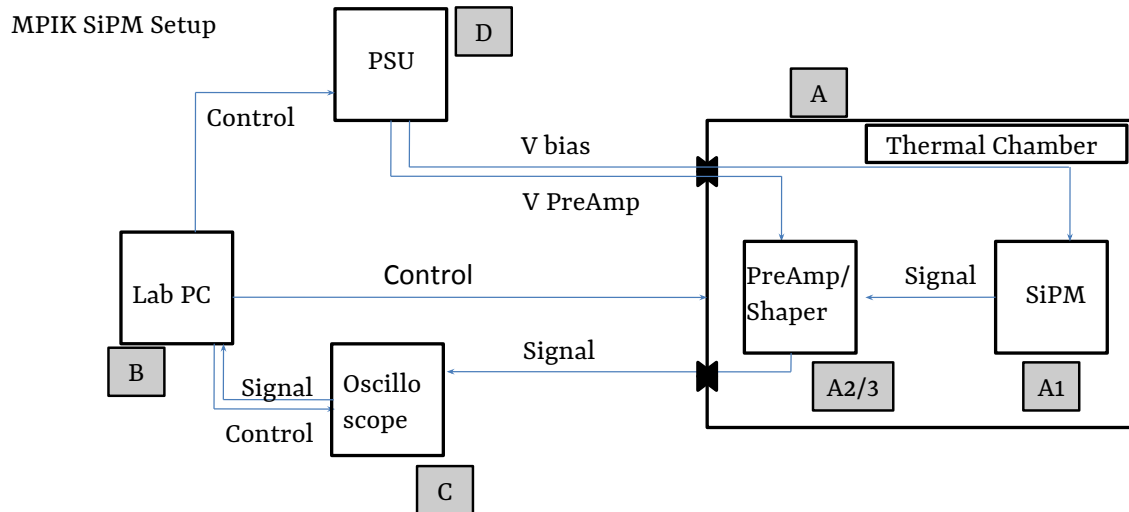


Figure 12: Experimental setup scheme, Annotations see text

594 ramps. Signal transfer from the shaper to the oscilloscope is via a throughput on the side. All
 595 equipment is connected via ethernet, plugged into a common hub, to form a local network.
 596 While the temperature of the thermal chamber is ramping from the previous to the next set-
 597 point, the data is send to the Lab-PC.

598

599

600 Temperature regulation is an issue in the teststand, as there is no way of controlling the SiPMs
 601 surface temperature. In dark conditions however, without conducting illumination tests, the
 602 shift in temperature on the SiPMs surface is only minimal. See section(F) for the breakdown-
 603 voltage dependence on temperature. Checking the surface temperature of all devices with a
 604 temperature probe during testing showed minimal rising temperatures. So the influence of the
 605 temperature on the breakdown-voltage is only of minor concern. However, once illumination
 606 tests begin, the rising temperature on the SiPMs surface will no longer be negligible and the
 607 temperature must be regulated, either by cooling of the surface or including the temperature
 608 parameter.

609

610 There is also the issue of the saturation of the input of the oscilloscope making the higher
 611 over-voltage range difficult to reach, due to potential multi p.e. pulses being amplified and
 612 reaching the input. This is possible because of the difference in amplitude between a 1 p.e. and
 613 a multi p.e. event and the electronic noise, forcing a high resolution of the amplitude in the
 614 oscilloscope.

615



Figure 13: The shaped and unshaped pulse from a pulse generator emulating the output of the front-end buffer of the CHEC-S SiPM. The unshaped pulse in yellow and negative, due to the buffer-output. The shaped pulse is flipped to the negative through the electronics in green. Image credit [21]

616 The shaper consists of two stages, the main
 617 components are an Op-Amp amplifier serving
 618 as an input buffer followed by a zero pole
 619 cancelation circuit for pulse shaping and is
 620 commonly used in photon-counting applica-
 621 tions. A zero pole cancelation circuit is ba-
 622 sically a RC circuit eq(4) (C_Z , R_0) supressing
 623 the high frequencys to narrow the pulses from
 624 the usual ~ 50 ns to ~ 10 ns, using a high-pass
 625 filter with a tunable time constant, through
 626 f_C which gives control over the frequency re-
 627 sponse of the circuit.[22]

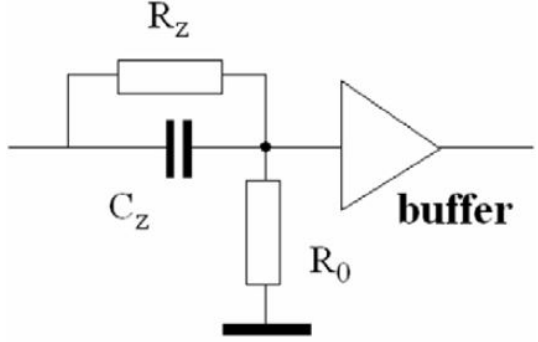


Figure 14: A Zero Pole cancelation circuit com-
 monly used in photon counting applica-
 tions. Taken from [22]

$$R_0 \times C_Z = 1/(2\pi \times f_C) \quad (4)$$

628 In Figure(13)[21], the shaped and unshaped pulse is shown, the negative amplitude (yellow)
 629 corresponds to the unshaped signal mimiced by a function generator to emulate the output of
 630 the front-end buffer of the CHEC-S SiPM. These tests correspond to an initial design of the
 631 shaper and do not correspond to the final setup.

632

633

634

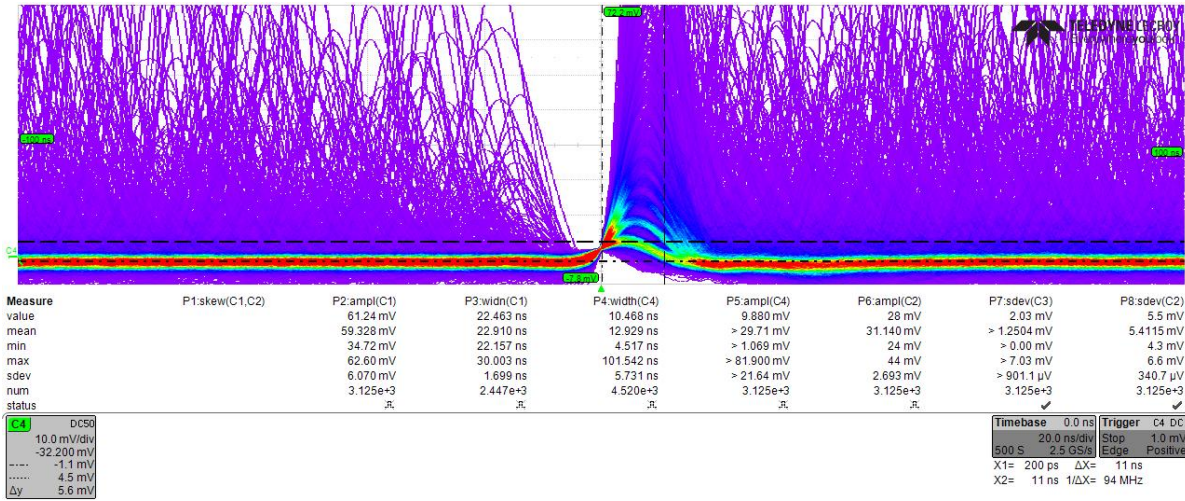


Figure 15: Persistence figure of the shaped pulse after adapting the electronics to a preferable pulse shape. In the center, a row of pulses with rising quantified amplitudes is visible. These are the multiple N p.e. pulses, differing by ~ 5 mV. The purple area off-center is due to delayed cross-talk and after-pulsing. Image credit [21]

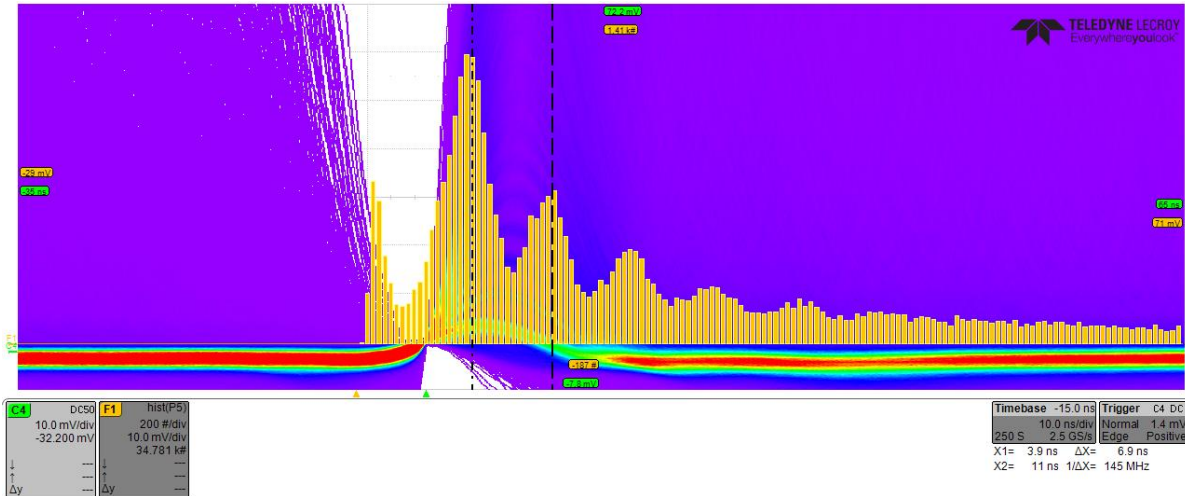


Figure 16: An oscilloscope based pulse height spectrum in the same scheme as the persistence plot fig(15). The distance between the peak maxima delivers an estimation of the gain of the SiPM at this bias-voltage. Image credit [21]

635 The shaper board contains tuneable capacitors (C9) and resistors (R20) (see schematic in
 636 section(G)), that can be tuned and optimized for ideal pulse layout. The green pulse in
 637 figure(13) shows the output after shaping, with a width of FWHM of 9 ns. The output pulse has
 638 some ringing after the main pulse.

639

640 After tweaking the tunable electronics on the shaper to a preferable pulse shape, clear quan-
 641 tified single p.e. peaks are visible in a persistence plot. fig(15). The peaks have an amplitude of
 642 ~ 5 mV/p.e., from this and from the following, a gain estimate for the peak finding threshold in

643 the analysis can be made. With the same configuration a gain estimate at different bias-voltages
644 of the SiPM is possible through an on-oscilloscope pulse height spectrum fig(16). The distance in
645 peak maxima is a reference to the gain of the SiPM, in the case of figure(16) close to ~ 5 mV/p.e..

646

647 This chain of shaper modification is done for every single SiPM cell from Hamamatsu Photo-
648 tonics K.K. tested in this work (three in total) as they arrived as a single unmounted device,
649 in need of shaping and amplification. The device from SensL is premounted on a test array,
650 preshaped and only externally amplified.

651 5 Data Analysis

653 The analysis of the SiPM waveforms is done exclusively in python following the sequence:

654

- 655 1. data conversion
656 2. pedestal subtraction
657 3. peak detection
658 4. gain extraction
659 5. calculation

660 The waveform data, after being transferred to a separate PC, is analyzed offline. The goal is
661 to extract event-data from the waveforms in order to produce pulse-area spectra for every bias-
662 voltage at every temperature. To that end, the pedestal of the electronic noise must be found and
663 subtracted from the data. After that, event-pulses are detected and integrated. This generates
664 a list of pulse-areas, which is in turn used to fill a pulse-area histogram. To this pulse-area
665 histogram, a model is fitted from which the gain can be extracted. Due to the linear behavior
666 of the gain with rising bias-voltage, a regression line is fitted, from which the DCR and the OCT
667 are calculated using the original pulse-area histogram.

668 5.1 Tracefile Conversion

670 The oscilloscope produces the waveform data in its intrinsic data format, called a trace with
671 the data suffix trc in binary. A trace file contains a header and two binary lists, an amplitude
672 based on the oscilloscopes voltage-range and offset, and a list of the same length containing the
673 associated event-time, based on the time-range and horizontal offset. The first step is therefore
674 a conversion of the amplitude and associated event-time of all segments of a waveform trace
675 file into two lists of floats.

676

5.2 Pedestal Subtraction

678 A single waveform from the oscilloscope is
679 anticipated to be uncentered fig(17)(grey), it
680 will be slightly above or below zero, depending
681 on the device setup (some devices pro-
682 duce inverted signals). The signal is mixed
683 with electronic noise when it is observed
684 and forms a pedestal, shifting the mean of
685 the waveform from its original position to
686 zero. Pedestal subtraction removes this av-
687 erage noise.

688 The first step of the process is reading in the
689 uncentered waveform fig(17)(grey) and cal-
690 culating an initial mean(mean0), expected to
691 be slightly higher than the actual mean of the
692 noise, due to the presence of event-pulses.
693 The waveform is then shifted to about zero,
694 by subtracting the mean0. A second mean of the now nearly centered waveform is taken
695 (mean1). Now a new, same-sized array is formed and filled with the data from the wave-
696 form that is smaller than mean1, this represents the negative part of the noise. The data larger
697 than mean1, the positive noise, is also filled into the array, but is negative-signed. This cre-
698 ates an array of the waveform centered around zero and, above the mean1, folded towards the
699 negative. It proved reliably, that calculating the root-mean-square of this helper-array is a solid
700 possibility of stripping the waveform of event-peaks. Taking the root-mean-square with a factor
701 3 of the helper-array, a cut is now applied to the waveform on both, the positive and negative
702 side. In that fashion, the remnant is the waveform between the positive and the negative root-
703 mean-square and is now called a peakless-signal, representing the noise of the waveform.
704 Pedestal subtraction is done by calculating the mean of this peakless signal and subtracting
705 it from the waveform. After that, the peakless signal is also smoothed by convolving it with
706 a wide-windowed gaussian and subtracted from the waveform to eliminate any slow moving
707 noise, the resulting waveform is called "Filtered Signal 1" fig(17)(blue).

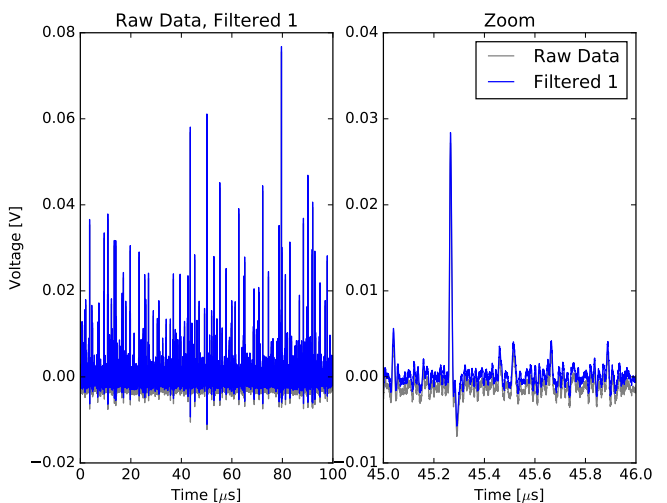


Figure 17: Raw, real data from a HPK SiPM in grey, in blue the pedestal subtracted and smoothed "Filtered Signal 1"

5.3 Peak Detection

710 Peak detection exploits the fact, that the first
 711 derivative of an event-peak will cross zero
 712 into the negative at the time of the peak max-
 713 imum. The presence of random noise in the
 714 signal however will lead to many false de-
 715 tections. Therefore, before the detection of
 716 the event-peaks, the waveform fig(18)(grey)
 717 is smoothed with a narrow-window gaussian
 718 with a width of about the FWHM of the de-
 719 vices characteristic event-pulse, in order to at-
 720 tenuate non-event peaks fig(18)(blue). After
 721 the first derivative of the signal is calculated,
 722 which in python is a fast process if using ar-
 723 rays, a number of parameters decide the va-
 724 lidity of the detected peaks. Most important
 725 parameters are a certain predetermined mini-
 726 mum amplitude, called the amplitude thresh-
 727 old or: minimum peak height. This is determined from initial examination of pulses on the
 728 oscilloscope and entered as a parameter to the analysis chain, but could later be calculated
 729 based on the noise level. The second important parameter defining validity is the minimum
 730 peak distance, which defines how close two events can occur after another. The value is deter-
 731 mined by the FWHM of the device in testing, which is expected to be sensible enough to resolve
 732 two events happening close after another. The peak detection algorithm can not distinguish
 733 between instantaneous and delayed Optical Cross Talk, but nonetheless, due to the fact, that
 734 the signal data is taken over many micro-seconds, all events are detected, independent of their
 735 source. On the other hand, this also means, that it is possible for two events to happen at the
 736 same time, for example a real photoelectron-event coinciding with delayed OCT or two simul-
 737 taneous dark events being misinterpreted as one dark event + its prompt cross-talk. This can
 738 not be distinguished and will lead to a slight shift of the amplitude, due to the mostly lower
 739 amplitude of afterpulsing and cross-talk events.

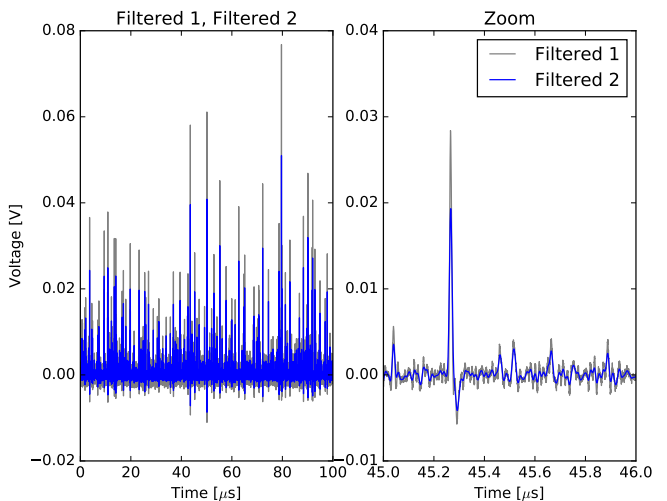


Figure 18: "Filtered Signal 1" in grey before smoothing with a narrow gaussian to generate "Filtered Signal 2" in blue, which is used for peak finding.

740
741

5.4 Gain Extraction

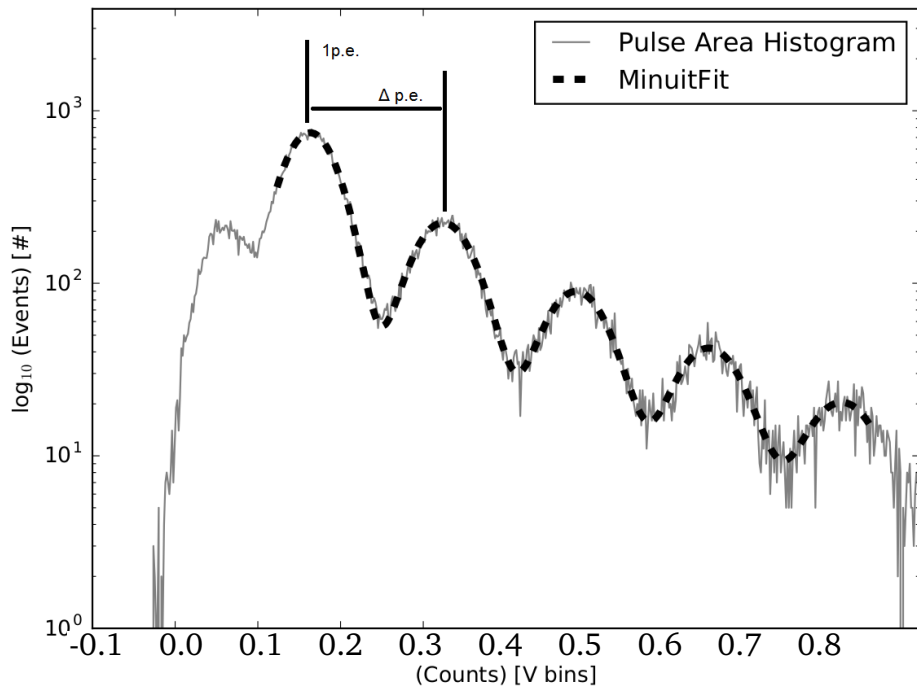


Figure 19: Pulse Area Histogram of a HPK S12642 with 1p.e. and Δ p.e. positions. Multi gaussian fitted function eq(5) as black dashed line.

742 The detected peaks are integrated with a window extending symmetricaly from the peak
 743 maximum, the width is chosen as slightly wider than the peaks FWHM. The generated list
 744 of peak areas is generating a peak area histogram (see section(E)). The amplitude, position
 745 and sigma of the first p.e. peak is calculated and fitted with a single gaussian using pythons
 746 scipy curvefit, the fitted parameters serve as a first guess. After the first guess parameters are
 747 determined, the histogram is fitted with a function of multiple gaussians eq(5) using iMinuit
 748 in python, seen in figure(19). To determine the number of gaussians to fit, another function
 749 checks the viability of each N p.e. peak, among the checked parameters is the ratio in height
 750 to the 1 p.e. peak and the amplitude of the checked Nth p.e. peak in the histogramm. The fit
 751 function $F(x)$ is a function of multiple gaussians with equal spacing eq(5). N is the multiplicity
 752 of the funciton or range the fit function is to be applied. A is the Amplitude of the Nth p.e. peak
 753 with σ , χ_0 is the x-position of the 1 p.e. peak, Δx is the p.e. spacing distance.

$$F(x) = (N \times \left[A \times e^{\frac{-(x-(\chi_0+N \times \Delta x))^2}{2 \times \sigma^2}} \right]) \quad (5)$$

754 Two parameters are extracted from the fit to the peak area histogram. The first χ_0 , the posi-
 755 tion of the 1p.e. peak is the position of the maximum of the first peak in the histogram, and the

756 position of corresponding multiple p.e. events should be integral factors of the 1p.e. position.
 757 This proved to not be the case for some devices, the suspected source of this error is a pedestal
 758 generated during the peak integration. For a more detailed study of the effect of the integration
 759 window see section(5.6).

760

761 A second parameter is extracted from
 762 the peak area histogram to deal with
 763 this problem, which is the distance be-
 764 tween N p.e. peak maxima of the his-
 765 togram, labeled Δ p.e. . This dis-
 766 tance defines the gain, as it gives a
 767 measure of the difference of the gener-
 768 ated signal of a 1p.e. signal and a
 769 2p.e. signal. The apparent pedestal
 770 of the pulse area histogram makes ex-
 771 traction of the two parameters necessary
 772 in order to calculate the DCR and the
 773 OCT.

774

775 The gain of a SiPM has a linear dependence
 776 of the supplied bias-voltage. Given that the
 777 bias-voltage range is deliberately chosen such

778 that the over-voltage ranges from about 1V growing upwards, the range of linearity only starts
 779 at around the point of operation given by the manufacturer of the device. At the higher end of
 780 the bias-voltage range the behaviour usually starts to divert from the linearity. In order to get
 781 an estimation of the gain over a large range, both previously extracted parameters, the 1p.e.
 782 peak and the distance Δ p.e. are fitted with a linear regression line. The fit assumes linear-
 783 ity utilizing weighted least squares inherited from pythons statsmodels package. For the fit, the
 784 data, where more than two gaussians are fitted to the peak area histogram has a stronger weight.

785

786 Plotting both extracted parameters, as well as their respective regression lines versus bias-
 787 voltage, as in fig(20), shows the difference between the two parameters. Comparing the
 788 manufacturer supplied breakdown-voltage from the datasheet for all devices shown, that the
 789 zero-crossing of the 1 p.e. regression line is more consistent with datasheet values, in contrast
 790 to the zero-crossing of Δ p.e. , which lies slightly higher. The over-voltage, corresponding to the
 791 set bias-voltage at any given temperature is calculated from this breakdown-voltage.

792 DCR and OCT are calculated utilizing 1p.e. position and Δ p.e. derived from the regression
 793 line. Both values are applied, in the calculation, to the peak area histogramm with the DCR of a

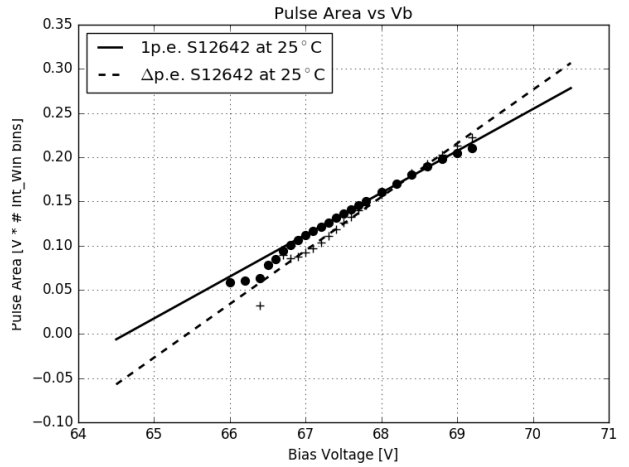


Figure 20: 1p.e. position and Δ p.e. extracted from the Pulse Area histogram at every bias-voltage for HPK S12642 with their respective regression lines.

794 SiPM being defined as all events exceeding 0.5 p.e. in amplitude $N_{events(\geq 0.5p.e.)}$ occurring over the
795 experiment time $t_{experiment}$ eq(6). Included in the measurement are thermally generated dark
796 counts, as well as delayed cross-talk and afterpulsing with only a minor contribution.

$$DCR = \frac{N_{events(\geq 0.5p.e.)}}{t_{experiment}} \quad (6)$$

797 The OCT of a SiPM is defined as all events exceeding 1.5 p.e. in amplitude [$N_{events(\geq 1.5p.e.)}$]
798 devided by all events exceeding 0.5 p.e. in amplitude [$N_{events(\geq 0.5p.e.)}$] eq 7. It scales with the
799 number of photons produced inside an avalanche, as well as the probability of these photons to
800 trigger a neighboring cell

$$OCT = \frac{N_{events(\geq 1.5p.e.)}}{N_{events(\geq 0.5p.e.)}}. \quad (7)$$

801 5.5 Analysis improvements

802
803 For one, at higher DCR the multi hit coincidence of two 1p.e. pulses rises and together with the
804 resolution of the waveforms this could lead to the OCT being calculated high (see section(K)).
805 Changing the determination of the threshold from being measured with an oscilloscope and
806 added as a parameter by hand, to being determined on a per-waveform basis before peak-
807 finding could improve the lower over-voltage resolution depending on electronic noise.
808 The source of the 'pedestal' in the pulse area spectra is suspected to originate from the pulse
809 integration, but this is not certain.

810
811

5.6 Data Challenges

812
813

5.6.1 The influence of the minimum peak distance

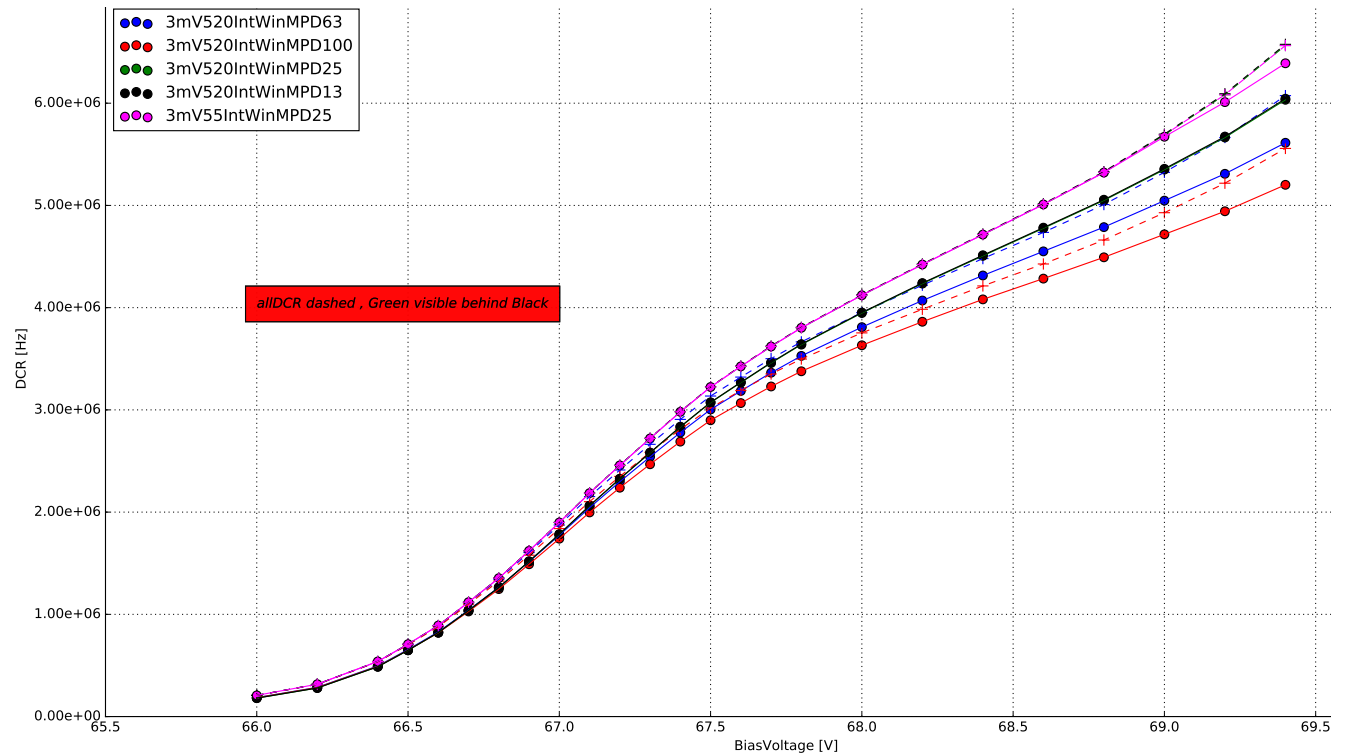


Figure 21: The difference between 4 minimum peak distance windows, in time-bins, during the peak detection. The dashed lines are the DCR considering all recorded events, forming an upper limit. In pink, the effect of a different integration window is shown.

The influence of the minimum peak distance is shown in fig(21) . Based on their bin-width, four different windows are tested. With the oscilloscopes sampling rate of 2.5 GS/s, the windows of 100, 63, 25 and 13 time-bins, correspond to 40, 25, 10, 5 ns windows respectively. With a event pulse FWHM of \sim 10 ns, setting the minimum peak distance to 100 bins, resulting in a 40ns window is visibly to large, as the algorithm will skip over valid data fig(21)(red). After an event is detected, skipping over 40ns worth of data will result in errors of the DCR, since the calculation uses the complete experiment time. Therefore a more reliable distance window must be chosen. The second window of 25ns was the next approach, originating from the length of the pulse-tail fig(21)(blue). This would lead to no detected events overlapping with the tail of one previously detected, resulting in a sharper pulse-area spectrum. Compared to a window of approximately the pulse FWHM, the previously discussed window would still lead to lost event-data. Since the sharpness of the pulse-area spectrum is already sufficient, a window around the pulse FWHM was chosen as reference for all measured devices fig(21)(green, obscured by black). Going lower than the pulse FWHM showed no improvement fig(21)(black).

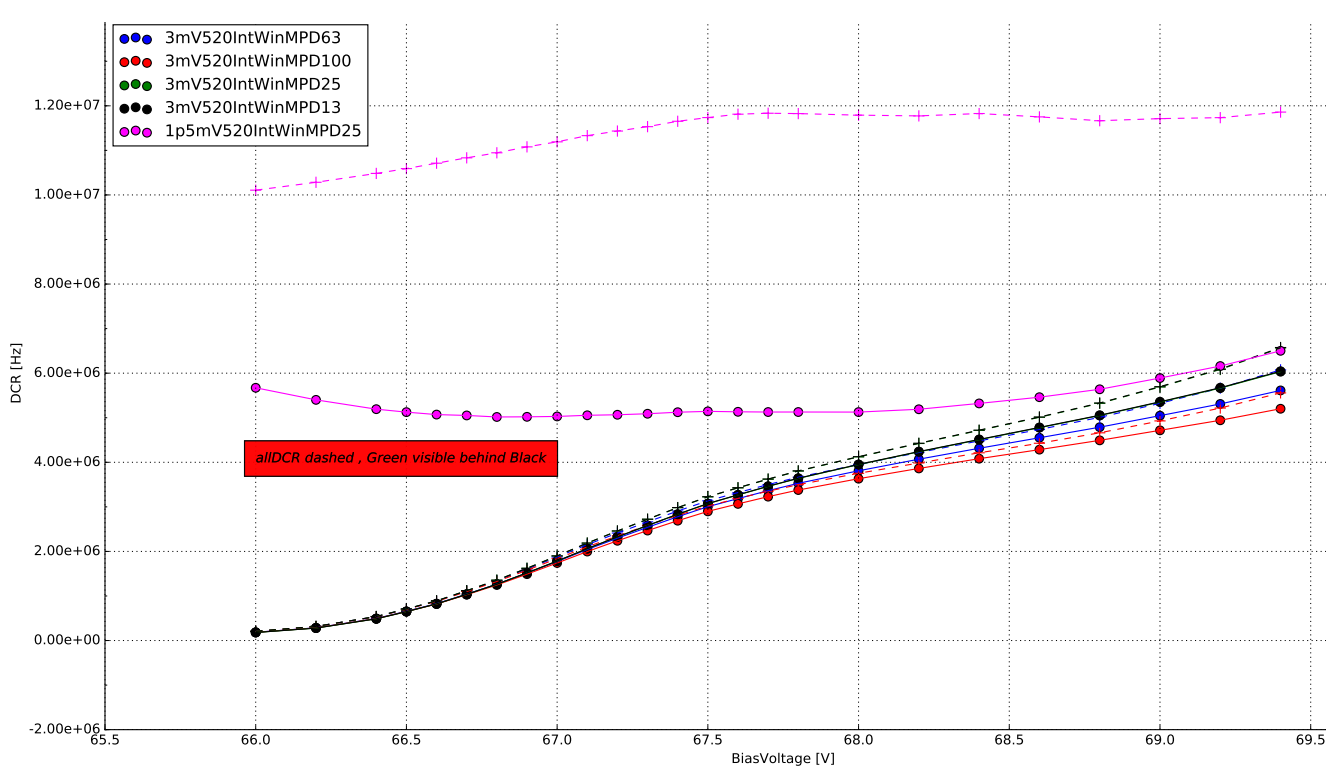


Figure 22: The difference between 4 minimum peak distance windows, in time-bins, during the peak detection. In pink, the effect of a lowered peak detection threshold is shown. The dashed lines are the DCR considering all recorded events, forming an upper limit.

828 5.6.2 The influence of the integration window

829
 830 Figure(21) also shows the influence of the size and shape of the integration window on the
 831 DCR. The influence of the chosen integration window is most visible in their respective pulse
 832 area spectra. Choosing a narrow, symmetrical integration window of 5ns left and right of the
 833 peak maxima, the noise peak, or zero-peak, is much more prominent compared to the pulse
 834 area spectrum of a symmetrical 10 ns window. This leads to errors in the multi-gaus fitting
 835 step, or the fitting will fail altogether. An asymmetrical integration window of 5ns left, 20ns
 836 right, to capture the influence of the pulse-tail proved, at first, to be the best solution as their
 837 was no visible zero-peak present. The low amplitude pulses are averaged out by the extended
 838 integration window to the right of the pulse-maximum. The downside of the asymmetrical
 839 window is the shifting of the pulsle area spectrum and the fact, that the N p.e. peaks get blurred.
 840 The next step was widening the window on both sides. This proved the best solution, since there
 841 is no zero-peak visible and the N p.e. peaks are gaussian shaped. Please see section(D) for the
 842 respective plots of pulse area spectra of the different windows.

843 5.6.3 The influence of the peak detection threshold

845 Choosing an adequate peak-finding threshold is a crucial step. Lowering of the threshold to
846 ~ 0.5 p.e. will cause the peak finding algorithm to misinterpret a lot of noise peaks as actual
847 dark incidents. This, of course, leads to errors in the gain extraction and even if a gain regression
848 line can be extracted, the resulting DCR and OCT will be incorrect. Figure(22)(pink), shows the
849 effect a low peak finding threshold has on the DCR.

850
851

6 Results

852
853

6.1 SiPM devices for CTA

Manufacturer	pixel size [mm]	cell size [μm]	coating	connection	specifics	pre-Amp
HPK S12642-1616PA-50 *CHEC-S SiPM	3	50	SR	TSV	no trenches	CHEC-S buffer
HPK LCT5 S13360-6050CS	6	50	SR	wire-bonds	trenches	MS 13V
HPK LCT5 6.975MM-SIL Single	6.915	75	SR	wire-bonds	trenches	MS 8V
HPK 6050HWB-LVR-LCT	6	50	SR	TSV	trenches	MS 13V
SensL FJ60035	6	35	glass	TSV	no trenches	MS 15V

Figure 23: List of SiPM devices which results are presented in this work. *(SR: silicon resin , MS: MiniCircuits , TSV: through silicon via)

854 SiPM devices for CTA are researched by many different groups, validating different characteristics.
 855 Besides the current SiPM for CHEC-S, newly developed prototypes offer a diverse range of
 856 pixel- and cellsizes. The majority of the devices are tested in Japan, at the University of Nagoya,
 857 conducting in depth analysis of the characteristics over a wide over-voltage range at one static
 858 temperature, mainly focusing on PDE and OCT, and their correlation. This correlation of OCT
 859 and PDE for all devices determines the candidate for CHEC-S, by comparing the highest PDE
 860 at the lowest possible OCT for each device. At MPIK, chosen candidate devices are examined
 861 regarding different characteristics and their temperature dependence and as to assist in the final
 862 decision by confirming results with a different analysis technique.

863

864 The chosen devices include the current CHEC-S device HPK S12642-1616PA-50, from Hamamatsu Photonics K.K., to be implemented in the first prototype camera. It is a previous generation SiPM, which was decided for use in 2014, due to the limited availability in high PDE devices at that time. The manufacturer supplies a 16*16 channel premounted tile of 3x3 mm² pixels with a cell-size of 50 μm. To emulate the usage in a TARGET module, four 3x3 mm² pixels are electrically connected to form a 6x6 mm² superpixel. The tile is typically coated with epoxy resin, but due to specific requirements regarding the uniformity of the coating, it was replaced with a very thin layer of silicon resin equivalent to later prototypes. The CHEC-S devices' electronical connection is realised via the new through-silicon-via (TSV) concept of running a

873 connecting solder through the silicon bulk, instead of wiring on the outside, greatly increasing
874 the fill-factor, but also including some disadvantageous sideeffects later shown.

875

876 Additional tested devices include the LCT5 generation from Hamamatsu Photonics K.K., so
877 called due to their low cross talk properties, namely the commercial available S13360-5050CS.
878 This device is the first to include physical trenches between the cells, effectively dividing the
879 cells optically and thus reducing prompt cross-talk probability.

880

881 The LCT5 generation also made two prototype devices available for testing at MPIK, the first,
882 HPK LCT5 6.975MM-SIL Single, is a larger iteration with a cellsize of 75 μm and a pixelsize of
883 6.915 mm, leading to larger fill-factor, which would imply higher PDE, but also DCR and OCT.
884 Being from the LCT5 generation it also includes optical trenches. The second device available
885 is a LCT5 prototype designated 6050HWB-LVR-LCT , LVR meaning low-voltage-range, with the
886 same physical dimensions and properties as the S13360 device but incorporating TSV technol-
887 ogy and possibly other unknown deviations.

888

889 The final device is a commercially available test-array designated FJ60035 from SensL, pre-
890 mounted on a test-array by the manufacturer. It has the same pixel-size, but a much smaller
891 cell-size 35 μm than the previous mentioned devices, and such a lower fill-factor, and a different
892 coating (glass).

893

894 The tests conducted in Nagoya contain many different iterations of the LCT5 generation with
895 varying pixel- and cell-sizes[19]. For a full overview of the considered SiPMs, please refer to
896 section(H).

897 **6.2 Hamamatsu S12642-1616PA-50 50 μ m 3mm**

899 The SiPM by Hamamatsu Photonics designated S12642-1616PA-
900 50 is a 3 mm by 3 mm device. The array uses the TSV tech-
901 nology, meaning there are no wire-bonds present, the electrical
902 connection is realised through the silicon-body. The pixels are
903 coated with a thin film of silicon resin, after the previously used
904 epoxy resin proved not uniform enough. The electrical contact
905 is realized through the TSV technology, establishing connection
906 through the silicon bulk, allowing a tighter fit of the cells, with
907 minimal dead-space. One array consists of 256 pixels, four of
908 which are electrically tied together to form a 6 mm by 6 mm superpixel respectively. Simula-
909 tions showed 6x6 mm² pixels to be the best choice, balancing FoV and angular resolution.

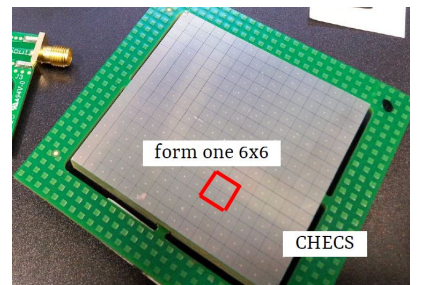


Figure 24: CHEC-S tile

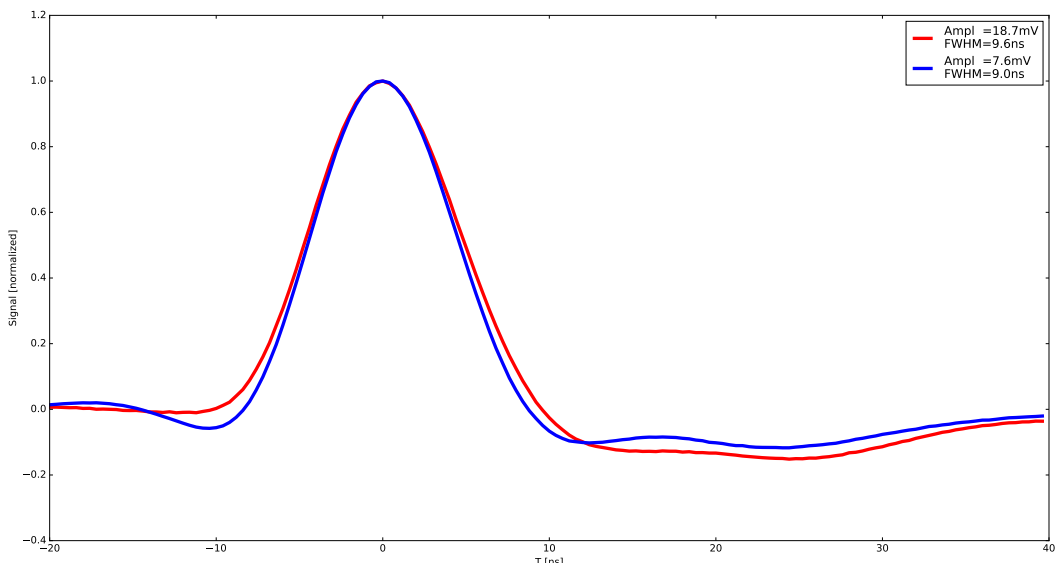


Figure 25: The average pulse shape of the 1photoelectron in blue and the 2photoelectron pulse in red of HPK S12642 at 25° C and 67.8V, which is around the proposed operating point. Both pulses are averaged over »1000 events and normalized to illustrate possible differences in pulseshape resulting from the utilized shaping electronics. Both pulses have a FWHM of around 10ns and are nearly free of ringing. The resulting average amplitude of the 1p.e. pulse is later used to calculate the Gain in [mV/p.e.] instead of [V*IntWin] by cross-referencing the 1 p.e. amplitude at multiple bias-voltages.

910 The measurements of the CHEC-S tile concentrate on the array as an as-is device. This means
911 their performance, influenced by external factors outside the actual SiPMs physics, are valid on
912 the assumption, that the way the measurements were conducted is the way the photomultiplier
913 will later be incorporated into the camera. On that ground, deviations of my results from the

results of other groups and the manufacturer itself are expected. To clarify this further, for example, it is expected that the tests done at Hamamatsu Photonics where conducted on a single 3 mm pixel, not an array of 256 pixels, where four are tied together. Also divergence of shaping and amplification electronics between the groups will result in some differences. For this test, the CHEC-S tile is connected to the CHEC-S buffer, supplied with ± 4 V, where the signal is amplified. This signal in turn is then shaped via the CHEC-S shaper, developed by the University of Leicester, see section(4). This whole amplification and shaping chain is simulating later usage in the TARGET modules. Multiple measurements were conducted on many different pixels of the CHEC-S tile, see section(I). The deviation between the pixels showed larger than measurement errors.

6.2.1 Gain

As described in section(3.2), the average pulse shape fig(25) is used to convert the relative gain from the analysis procedure to an absolute gain in sensible units. This is necessary, because the analysis aims to use pulse-area rather than -height, which results in this relative gain being in units of $V \times timebins$, instead of voltage. In Figure(26) shows the gain gain after conversion. A lower gain with increasing temperature is expected and described in detail in section(3.2). In short, increased lattice movement due to higher temperature hinders photoelectron transport. The effects visible at extreme bias-voltages at both ends are partially analysis related. The gain of a SiPM is expected to be linear over bias-voltage at a constant temperature.

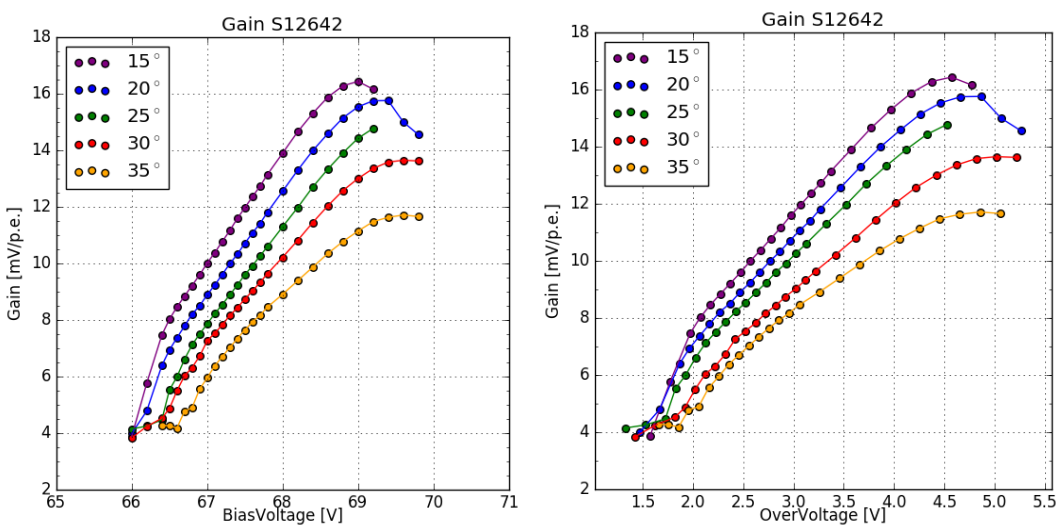


Figure 26: Gain of the HPK S12642 pixel, plotted against over-voltage , bias-voltage and temperature.

In the lower regime at $V_b \sim 66.5$ V the gain is low compared to the noise, so the analysis struggles to pick up pulses. Depending on the determined peak-finding threshold, the analysis is suspected to interpret noise peaks as 1p.e. peaks at an increasing rate, the lower the overvoltage is. This is visible in the sudden break in linearity at 30°C and 35°C , where the gain is almost

in a plateau, due to this effect. The roll-over of the gain at the highest bias-voltages is in part a result of a voltage drop across the bias resistor occurring, because of high current flow through the SiPM. At higher temperatures, and therefore higher dark rates, the effect occurs at lower over-voltages. A second influence is caused again, by the noise at V_{ov} 5V, which is very high compared to the proposed point of operation at V_{ov} 3V. The same threshold is again counting the now increased noise peaks as 1p.e. peaks, but due to the abundance of 1p.e. pulses this results in an apparent lowering of the gain.

6.2.2 Dark Count Rate

The DCR is expected to increase with temperature, which is the case for S12642 shown in Figure(27) and to follow a nearly linear progression, a sudden turn-up or turn-down of the DCR would be analysis related. The turn-up at a certain point is visible in fig(27), particularly for 15° C (purple) and 20° C (blue) respectively. At 15° C and an over-voltage of ~ 4 V, the DCR starts to deviate from the previously linear behaviour. It starts to rise more rapid than before, the OCT at that point is also very high; exceeding 50% fig(28) (left). For the higher temperatures of 25° C (green) and 30° C (red) this critical point is not reached, so the effect is barely, if not at all visible. At 35° C (yellow), due to the high rate of 9-10 MHz, slight heating of

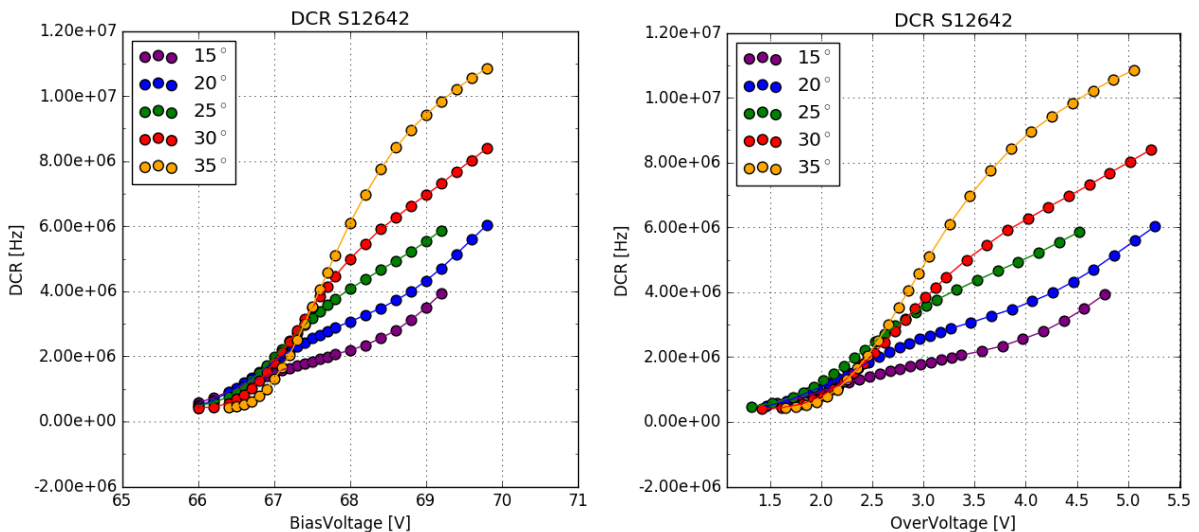


Figure 27: Dark Count Rate of the HPK S12642 pixel, plotted against over-voltage , bias-voltage and temperature. DCR at 2 - 3 MHz from datasheet at operation voltage = 2.4V and 25° C measured by current.

the SiPMs surface could also affect the DCR through a slight shift of the temperature upwards, away from 35° C . So that the DCR declared at 35° C is in reality the rate at higher temperatures. At the lowest end of the bias-voltage range, part of the found 1p.e. pulses are suspected to be noise related. So the DCR changing to a plateau is expected. This is also due to the

fact, that the measurements are done with a fixed bias-voltage range. Due to the increase of the breakdown-voltage with rising temperature, part of the measured bias-voltage range corresponding to a very low over-voltage, attributes to this effect. In order to reliably measure beyond an overvoltage of 2.5V in the lower range, the noise would need to be improved.

6.2.3 Optical Cross Talk

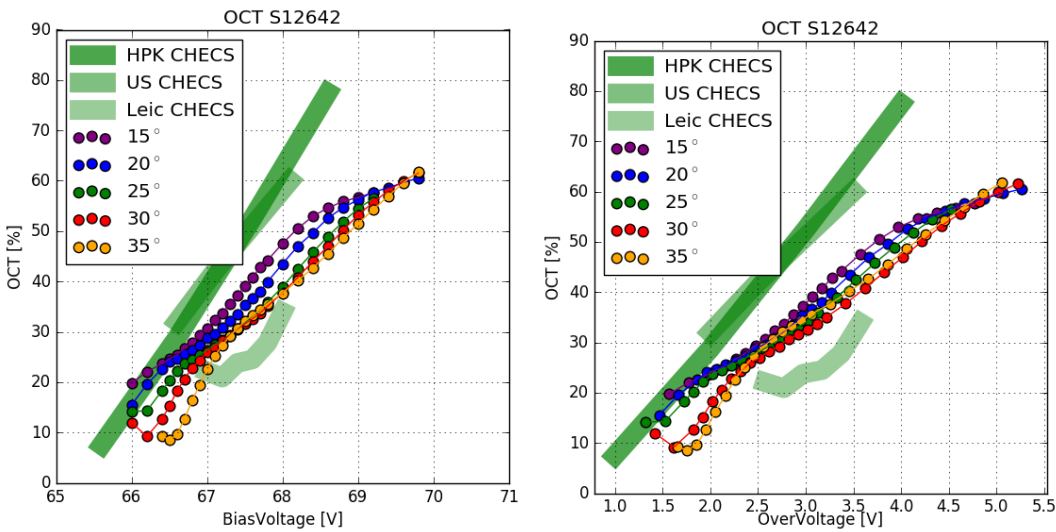


Figure 28: Optical Cross Talk of the HPK S12642 pixel, plotted against over-voltage , bias-voltage and temperature.

The OCT is expected to be linear and independent from temperature. This is confirmed for HPK S12642. Minor deviations from that are probably due to slight errors in the breakdown-voltage calculation from the gain regression line. At higher DCR the multi incident probability rises, an event of two simultaneous dark counts could easily be interpreted as a dar event + cross-talk. This leads to a systematic increase in OCT at the higher DCR, for examples see section(K).

The deviation of 30° C and 35° C below an over-voltage of 2V stems from the way the gain regression line is used to calculate both DCR and OCT. At higher temperatures the lower voltage range consists partly of noise, so using the gain regression line to calculate the OCT at those low voltages leads to the visible effect of the first few datapoints of 30° C and 35° C.

The deviations between the different groups results at 25° C (green) are caused by 4 major factors. Firstly the difference in the tested device. While the device measurements in this work has every four $3 \times 3 \text{mm}^2$ pixels electrically tied together, the way the device will later be implemented into CHEC-S, the groups in the US[17] and Hamamatsu Photonics[16] are likely to run tests on one $3 \times 3 \text{mm}^2$ pixel only. Secondly a slight difference in amplification and shaping electronics is suspected. The measurements conducted in this thesis as well as the measurements of Leicester are done with the same shaper and buffer configuration. The difference here is, thirdly, measurements are done with dark counts only, while measurements from other groups

984 are conducted with a pulsed light source and reading out timed windows. This causes the results
985 from Leicester to be difficult to compare against, their surface temperature of the SiPM is likely
986 much higher than 25° C, and thus, a misinterpreted breakdown-voltage at 25° C causes a shift
987 of the OCT to the right. Lastly the difference in actual data taking and analysis procedure must
988 be mentioned, also this is only of minor concern, as we will see with other measured devices.

6.3 Hamamatsu LCT5 50 μ m 6mm

991 The SiPM designated HPK S13360 6050CS fig(29) is
 992 an LCT5, meaning Low Cross Talk 5th iteration de-
 993 vice from Hamamatsu Photonics. It is one of the most
 994 promising candidates for later usage in CHEC-S. It has
 995 a pixelsize of 6 mm consisting of 14400 cells with a
 996 cellsize of 50 μ m. The present device and its similar
 997 iterations are the first to incorporate trenches border-
 998 ing each cell, effectively insulating the cells and reduc-
 999 ing the prompt OCT. Tests are done with a single pixel
 1000 only, in contrast to measurements done on S12642. It
 1001 is mounted on a ceramic chip and coated with a sil-
 1002 icon resin that is UV-transparent. Wire-bonds supply
 1003 the electrical contact. A similar, but not tested, device from the same generation uses TSV
 1004 technology.

LCT5 6mm

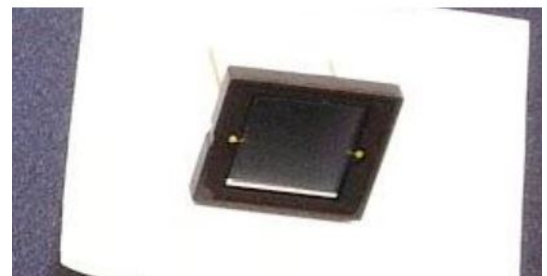


Figure 29: HPK S13360 6050CS pixel

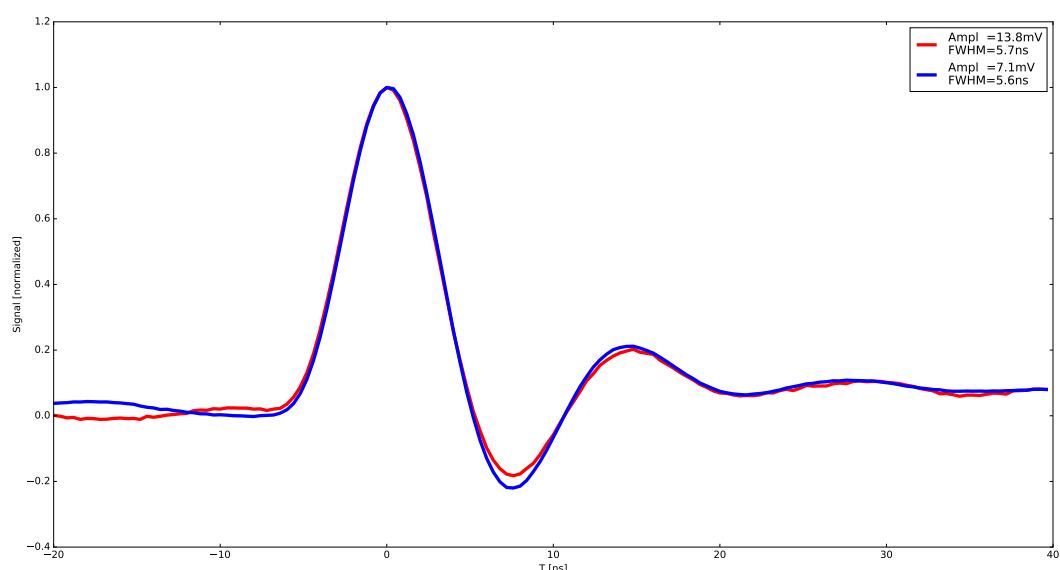
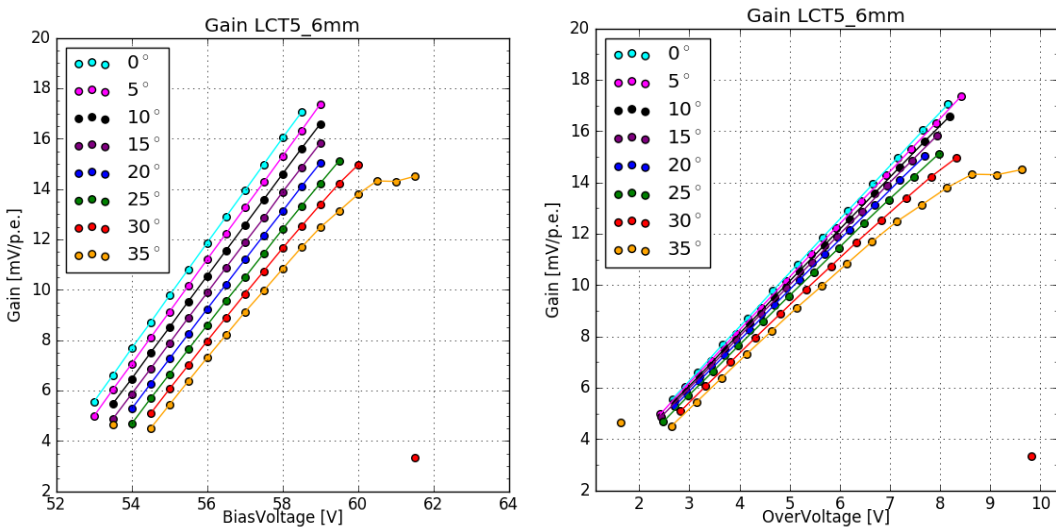


Figure 30: The average pulse shape of the 1photoelectron in blue and the 2photoelectron pulse in red of HPK S13360 6050CS at 25° C and at point of operation. Both pulses have a FWHM of around 5ns and ring for approximately 20ns with an undershoot of 20%.

1005 The layout of the single pixle test device made external amplification necessary. An amplifier
 1006 from MiniCircuits was supplied with 13V during this test. Shaping of the pulse is conducted
 1007 by a CHEC-S shaper, modified to fit the new unshaped pulse. The pulse shape fig(30) makes
 1008 the pulses appear much harder to analyze, due to the possibility of events occurring during the
 1009 ringing window. This assumption proved untrue, due to the devices low DCR and OCT, resulting
 1010 in a low multi incident probability.

1011 1012 6.3.1 Gain

1013 The gain of the LCT5 50 μ m 6mm device is clearly linear with some minor outliers at 30°C.
1014 The same effect as with S12642 is visible at 35°C, again counting noise peaks as 1p.e. peaks,
1015 resulting in an apparent lowering of the gain and the slope changing over into a plateau. In
1016 figure(31)(left) the gain is shown, plotted against over-voltage. It is still dependent on tem-
1017 perature, but due to reliable breakdown-voltage calculation, the spread is much smaller than,
1018 if plotted against bias-voltage. The same conversion is done to transform relative gain into an
1019 absolute gain with sensible units. When parametrized with over-voltage, the gain is essentially
temperature independent.



1020 **Figure 31:** Gain of the HPK S13360 pixel, plotted against over-voltage , bias-voltage and temper-
1021 ature.

1022 6.3.2 Dark Count Rate

1023 The DCR of two similar HPK S13360 devices is shown in figure(32). The bars show the dif-
1024 ference between the two devices, the results of one device is used as a reference, while the
1025 deviation is illustrated with the filled bar. The DCR of HPK S13360 follows the expected be-
1026 haviour, mostly linear in the significant range and rising with increasing temperature. Below
1027 an over-voltage of 2.5 V the gain is suspected to be low enough for larger noise peaks to be
1028 misinterpreted as events. Thus the regression line calculation is unreliable in this range.

1029 The turn-up at high over-voltages is most prominent at 0 °C(teal) after an over-voltage of 9 V. It
1030 is not pulse related, being at a DCR of 1 MHz it would be visible earlier for higher temperatures,
1031 but their slope is linear. This is also the point where the OCT rises very rapidly. The datasheet
1032 values from the manufacturer cover a large range of the DCR at an over-voltage of 3V, making
1033 is difficult to compare against, the manufacturer determines the DCR by measuring the current.

1035 A standard counting error of the DCR is largest in the lower bias-voltage range. Despite the
 1036 low DCR at an over-voltage of 2 V of ≤ 0.5 MHz, in a measurement window of $100 \mu\text{s}$ there
 1037 are still ≥ 50 pulses detected. This means an experimental run of 500 segments of the $100 \mu\text{s}$
 1038 measurement window shows a standard counting error in the DCR of 0.003 MHz, below 0.1%.
 1039 This is lower than errors related to analysis or data acquisition and not visible given the size of
 1040 the datapoints.

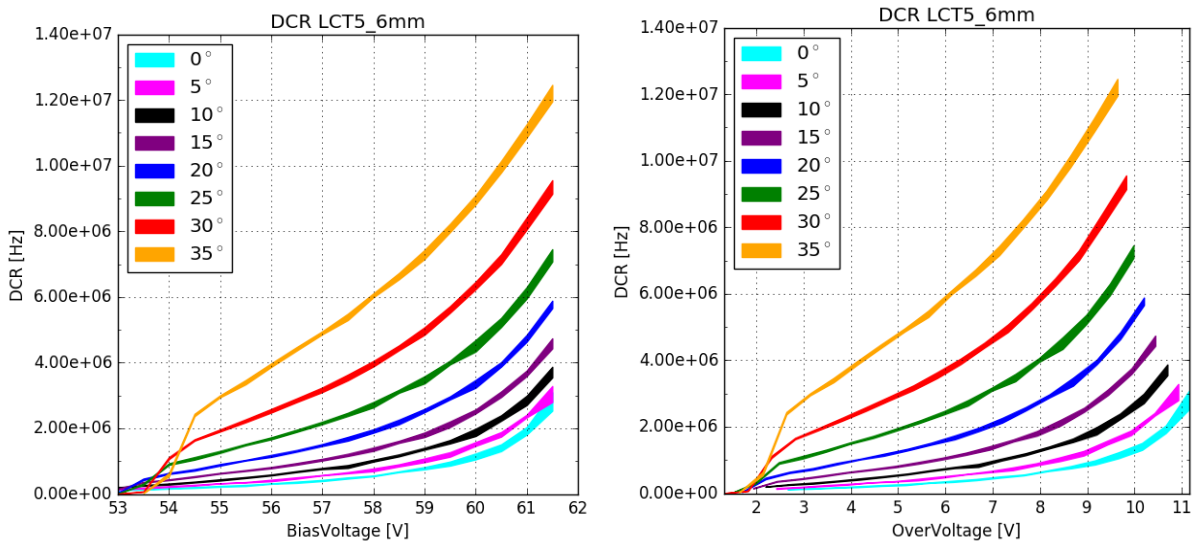


Figure 32: Dark Count Rate of the HPK S13360 pixel, plotted against over-voltage , bias-voltage and temperature. The Datasheet values cover a very large range between a DCR of 2 - 6 MHz at an over-voltage of 3 V at 25 °C, to wide to compare to reliably, and is measured by current.

1041 6.3.3 Optical Cross Talk

1042 The measurements of the HPK S13360 SiPM done at the Nagoya University[19], Japan fig(33)
 1043 (faded green bar), correlate very strong with results from this thesis of the OCT in the over-
 1044 voltage range between 2.5V and 9V. The OCT in this range is linear and independent from
 1045 temperature, with minor deviations attributed to the breakdown-voltage calculation from the
 1046 regression line, causing the horizontal shift. In contrast to the dark counts measurements in this
 1047 thesis, the measurements at Nagoya University followed a pulsed light source approach, read-
 1048 ing out a time-window after the laser incident. This could have consequences, since OCT with
 1049 a longer delay time could be missed. Deviations below an over-voltage of 2.5V are expected,
 1050 they are very likely caused by the regression line calculation being unreliable in this range due
 1051 to the analysis method misinterpreting noise as dark count events. Above an over-voltage of 9V,
 1052 which is also the point of the turn-up of the Dark Count Rate, the OCT is no longer linear and
 1053 the deviation from the results of Nagoya University increase very rapidly. The rapid increase
 1054 in both DCR and OCT is suspected to be caused by the over-voltage reaching ranges, where

interpretation of noise as a 1p.e. pulse becomes more likely. This, joint together with the usage of the MiniCircuits amplifier supplied with 13V, makes false interpretation of noise as pulses even more likely. These two reasons in conjunction are suspected to be responsible for both, the sudden rise of the DCR as well as the deviation of the OCT from linearity and the results of Nagoya University, above over-voltages around 9V. In summary, the correlation between the two measurements, conducted by two different methods of data acquisition and analysis, is evident.

1062

1063

1064 The S13360 series is the first to incorporate physical barriers, called trenches, effectively insulating the cells from each other. This drastically reduces the prompt cross-talk, while increasing 1065 the percentage the delayed cross-talk contributes to the overall cross-talk shown. This could 1066 also be the reason for the up-turn, compared to data from the University of Nagoya; at higher 1067 over-voltages the contribution from delayed cross-talk is higher[14]. With the trenches effectively 1068 reducing the prompt cross-talk and the difference in analysis, the effect could be partially 1069 explained by increased contribution of the delayed cross-talk. More on this subject in section(7). 1070

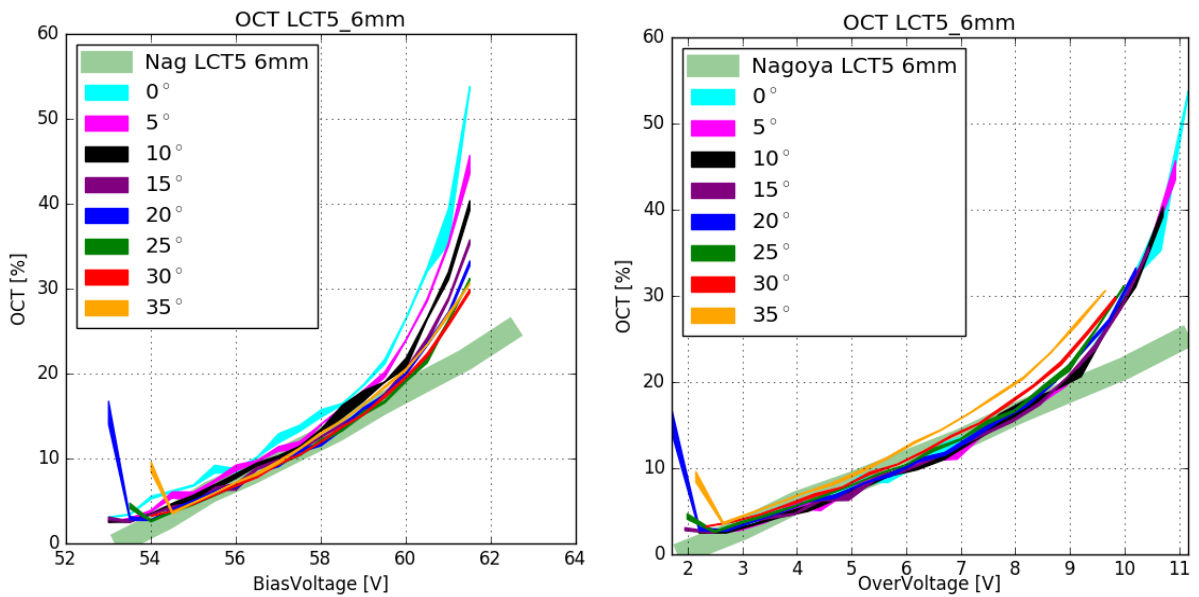


Figure 33: Optical Cross Talk of the HPK S13360 pixel, plotted against over-voltage , bias-voltage and temperature.

1071 6.4 Hamamatsu LCT5 75 μ m 7mm

1073 The device named 6.975MM-SIL Single is a larger LCT5
1074 prototype SiPM of the same design as S13360-6050CS
1075 fig(34). With an increase in cellsize to 75 μ m, the
1076 device gains a higher fill-factor than 50 μ m devices.
1077 The pixel-area is also expanded to 6.915x6.915 mm²,
1078 which will result in a higher fill-factor (less deadspace),
1079 both size increases together will presumably result in a
1080 higher PDE but also a higher OCT. Since it is a proto-
1081 type device, there is limited data from datasheets. The
1082 ID number suggests, that it is also a wire-bond device
1083 with a UV-transparent silicon-resin coating. It is also a
1084 single pixel test device, so external amplification is nec-
1085 essary with the MiniCircuits PreAMP, supplied with 8V during this test. The signal is shaped by a
1086 differently modified CHEC-S shaper, which results in a pulse shape similar to S12642, but with
1087 a much lower amplitude fig(35).

LCT5 7mm



Figure 34: HPK LCT5 7mm pixel

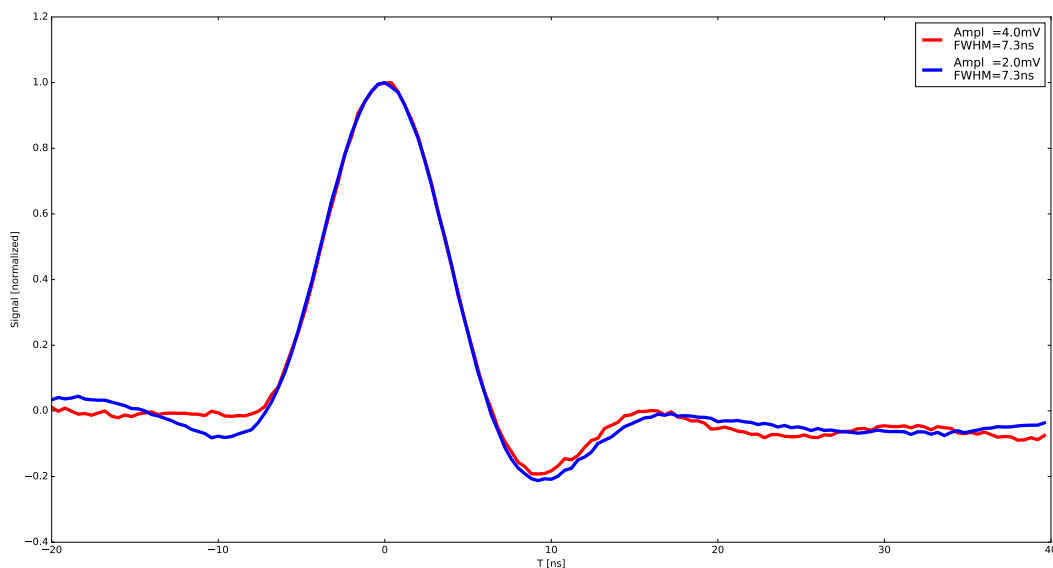


Figure 35: The average pulse shape of the 1 photoelectron in blue and the 2 photoelectron pulse in red of HPK LCT5 7mm at 25° C and at point of operation. Both pulses have a FWHM of around 7ns and an undershoot of 20%, with no ringing.

6.4.1 Gain

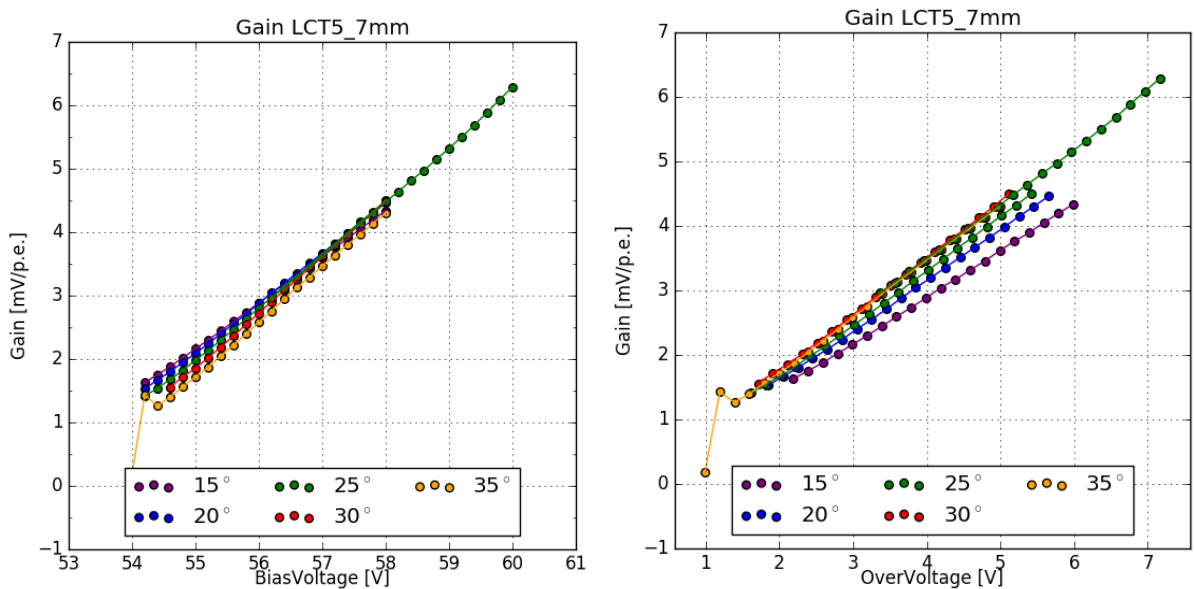


Figure 36: Gain of the HPK LCT5 7mm pixel, plotted against over-voltage , bias-voltage and temperature.

Figure(36) shows the gain of the LCT5 7mm device. Two sets of measurements are done for 25°C to extend the measured range. The first set of measurements covers the lower over-voltage range, where the low gain makes external amplification necessary with a MiniCircuits PreAMP supplied with 8V. The lowest possible amplification of the PreAMP is chosen, so that reaching the point of saturation of the oscilloscope input is as late as possible as the over-voltage rises. Saturation of the oscilloscope occurs due to the possibility of generating very large p.e. ($>10\text{p.e.}$) events at the higher over-voltages, which are saturating the input. Joint together, the LCT5 7mm device and the MiniCircuits PreAMP at 8V reach this point at an over-voltage of $\sim 6\text{V}$. In figure(36) the results from the lower range measurement are displayed as the lower-range green line extending between an over-voltage of 1.6V to 5.4V . The configuration for the second test removes the PreAMP from the setup, which makes the lower over-voltage range unaccesible, but extends the range to higher over-voltages. This configuration reaches the point of saturation at an over-voltage of $\sim 8\text{V}$. The higher range measurement results are displayed as the second green line (25°C) extending from 3.4V to 7.2V over-voltage in figure(36). There is a clearly visible overlap of the two measurements between $\sim 3.4\text{V}$ and $\sim 5.4\text{V}$. It also seems, that the gain dependency on temperature is reversed. While for all other devices, the gain lowers with rising temperatures, the LCT5 7mm device seems to show inversed behaviour. This inverse behaviour is caused by the calculation of the breakdown-voltage from the gain-regression line and is likely an error. Plotting the gain versus bias-voltage, however, shows the expected behaviour of the gain.

1110
1111

6.4.2 Dark Count Rate

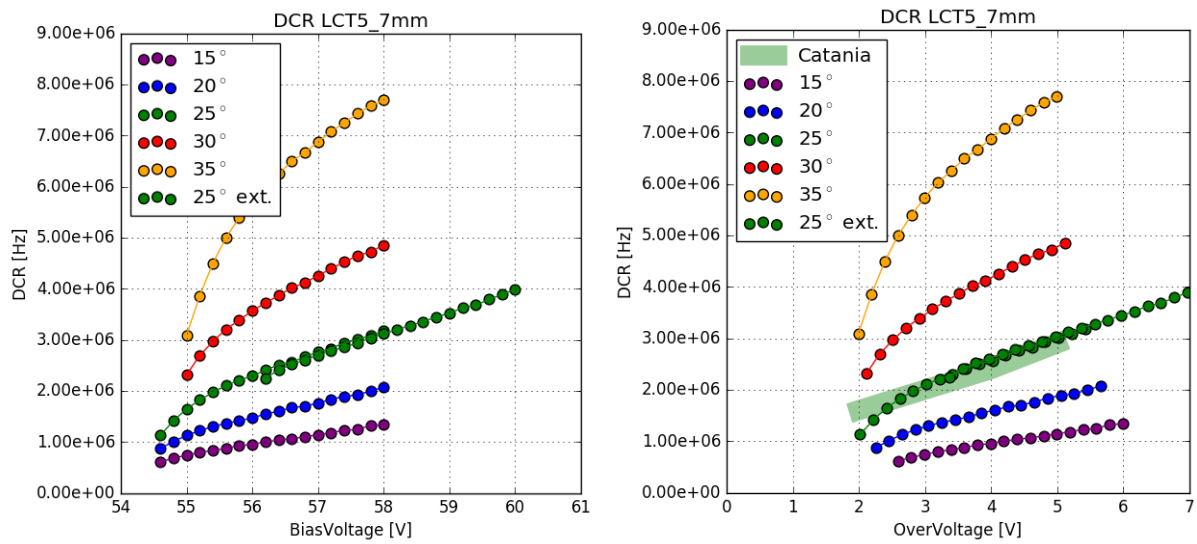


Figure 37: DCR of the HPK LCT5 7mm pixel, plotted against over-voltage , bias-voltage and temperature.

The behaviour of the DCR of the HPK LCT5 7mm device is shown in figure(37) and is as expected, in contrast to the behaviour of the gain of LCT5 7mm, as discussed in section(6.4.1). It follows a linear progression in the relevant range and increases with rising temperature. I suspect the over-voltage range above $\sim 2.5\text{V}$ to be relevant. The extended range measurement at 25°C confirms this behaviour. LCT5 7mm shows a linear DCR over an over-voltage range of 4V. The faded green bar in figure(37) shows results from measurements undertaken by the Department of Physics and Astronomy at the University of Catania. Those measurements were conducted on the exact same device, which is an important point, but with a different method of data acquisition and data analysis. Analysis techniques are discussed in section(7). The correlation between the two experiments is evident, although there is differences in the acquisition and analysis process.

1123
1124

6.4.3 Optical Cross Talk

The OCT is expected to be linear and independent from temperature. This is the case in the, in section(6.4.2) established, relevant over-voltage range of above $\sim 2.5\text{V}$. Minor deviations are attributed to the calculation of the breakdown-voltage from the gain-regression line. The over-voltage is calculated from the former and the supplied bias-voltage, which in turn causes a slight horizontal shift. With that, comparing my results to the measurements at 25°C (faded green bar) from the University of Catania shows a strong correlation.

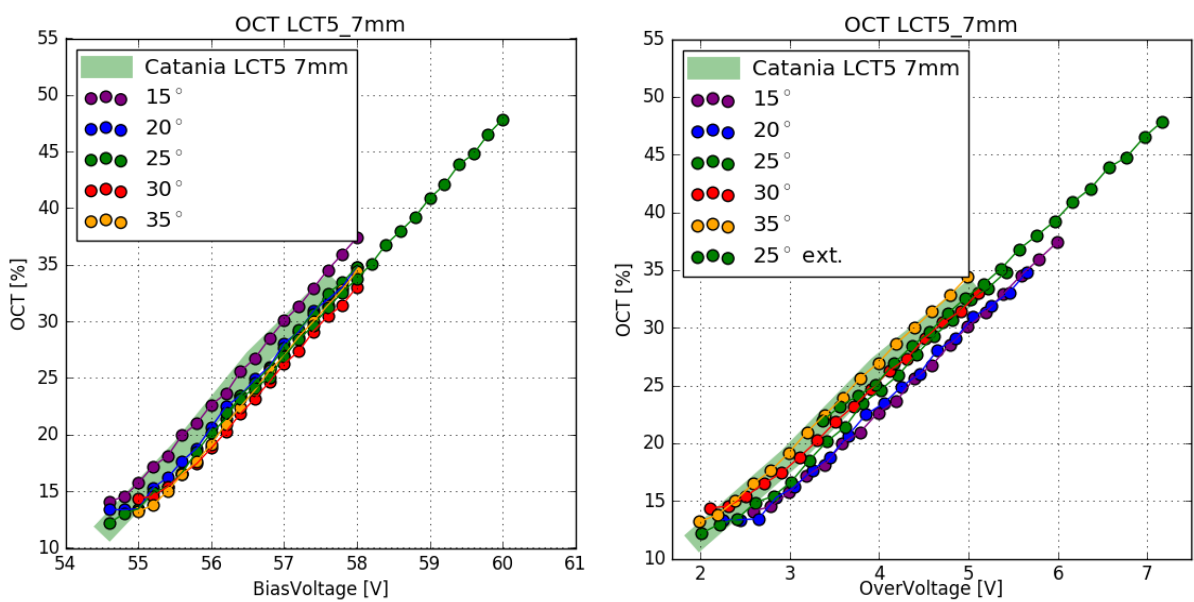


Figure 38: Optical Cross Talk of the HPK LCT5 7mm pixel, plotted against over-voltage , bias-voltage and temperature.

1131 1132 6.5 Hamamatsu LVR 50 μ m 6mm

1133 The SiPM by Hamamatsu Photonics with the designation
1134 6050HWB-LVR-LCT is a special prototype of the
1135 LCT5 design. LVR is an abbreviation of Low Voltage
1136 Range, meaning the device is meant to be operated
1137 at much lower operation voltages than other LCT5
1138 devices. It has the same physical size as an LCT5
1139 50 μ m 6mm device (S13360 section(??)), a pixelsize
1140 of 6mm pixel with a cellsize of 50 μ m. The recom-
1141 mended point of operation however is \sim 15V below
1142 that of the S13360 device, specifically at 40.2V(LVR)
1143 instead of 54.7V (S13360). It uses the TSV technology
1144 for electrical connection. The unshaped signal is similar to other LCT5 devices, therefore us-
1145 ing the same modified CHEC-S shaper is feasible in this case, resulting in a similar pulse shape
1146 fig(40). After that the signal is amplified with the same MiniCircuits PreAMP supplied with 8.5V.
1147

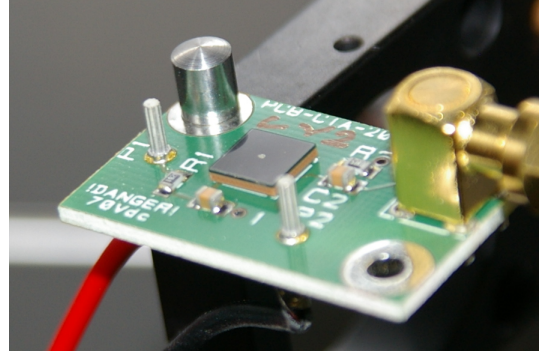


Figure 39: HPK LVR 6mm pixel

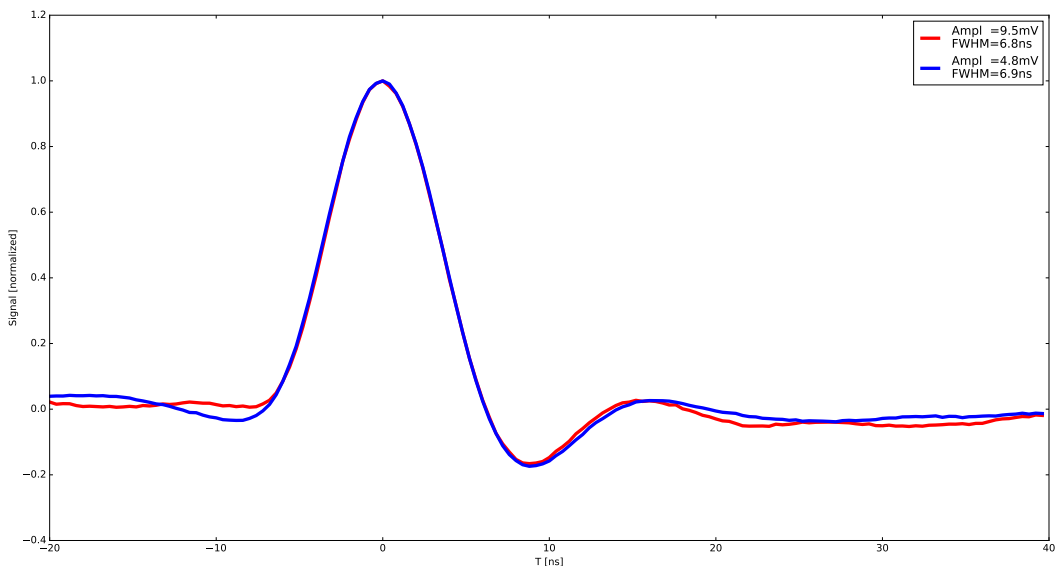


Figure 40: The average pulse shape of the 1photoelectron in blue and the 2photoelectron pulse in red of HPK LVR 6mm at 25° C and at point of operation. Both pulses have a FWHM of around 7ns and an undershoot of 20%, with no ringing.

1148 1149 6.5.1 Gain

1150 Figure(41)(right) shows the gain of the LVR 6mm device. It is, as expected, linear over a
1151 long range and nearly independent of temperature when parametrized with over-voltage. The
1152 flattening of the slope to a plateau shape in the lower over-voltage range is caused by noise

1153 pollution. Only taking into account the linear region, limits the range, where the results are
 1154 relevant to an over-voltage range above ~ 2.5 V. Saturation of the oscilloscope in this range is
 1155 not visible, but a check with a more expanded range revealed, that the point of saturation of
 1156 the oscilloscope is at an over-voltage of ~ 5 V. The apparent overlap of the gain, when plotted
 1157 against over-voltage, is based on the calculation of the breakdown-voltage being very reliable
 1158 due to the large linear range. Plotted versus bias-voltage fig(41)(left) the expected behaviour
 of the gain, lowering with increasing temperature, is visible.

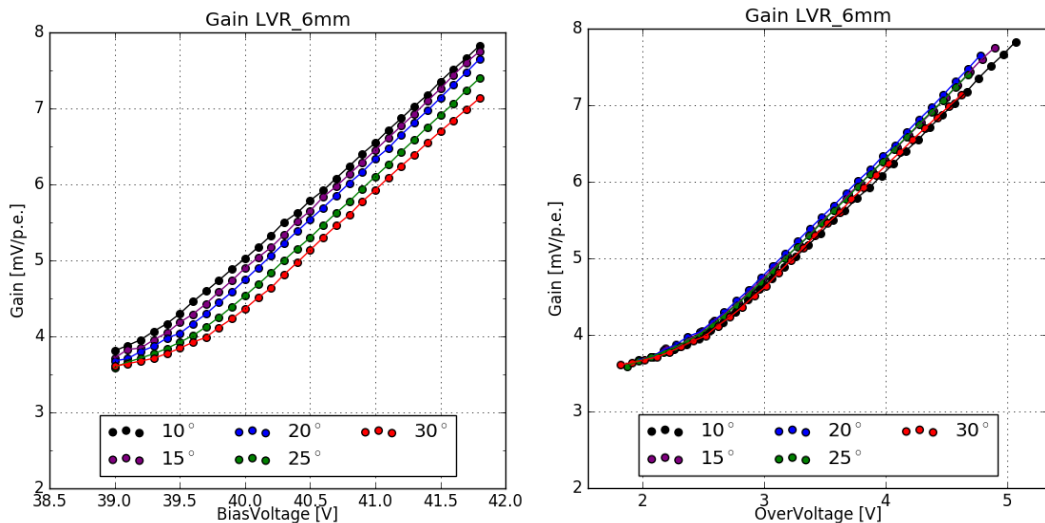


Figure 41: Gain of the HPK LVR 6mm pixel, plotted against over-voltage , bias-voltage and temperature.

1159

1160
1161

6.5.2 Dark Count Rate and Optical Cross Talk

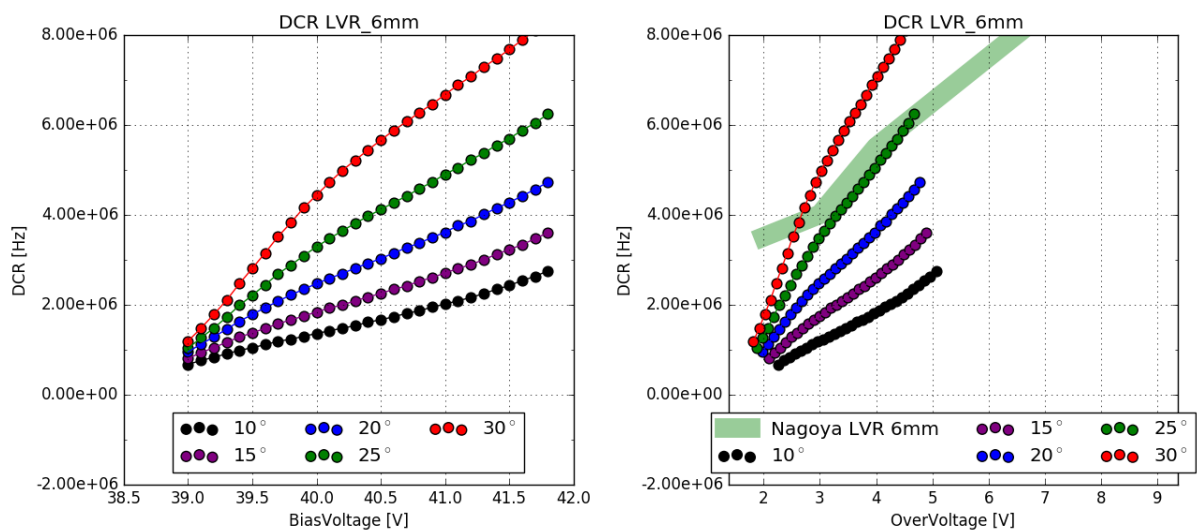


Figure 42: Dark Count Rate of the HPK LVR 6mm pixel, plotted against over-voltage , bias-voltage and temperature.

1162 The DCR fig(??)(left), taking into account only the relevant over-voltage range of $>\sim 2.5V$
 1163 seems to correlate, while the resulting OCT fig(??)(right) is very high compared to results from
 1164 the University of Nagoya, which also cover a much wider range. Only taking into account the
 1165 previously established relevant over-voltage range of $>\sim 2.5V$, the resulting OCT is a factor of
 1166 two higher. The device being a prototype, it could be the case, that there are physical differences,
 1167 a difference in coating, which combined with the TSV technology could lead to the present
 1168 uncorrelation[20]. This uncertainty is a contrast to results from previous devices, where strong
 correlations between different groups and measurement techniques are evident.

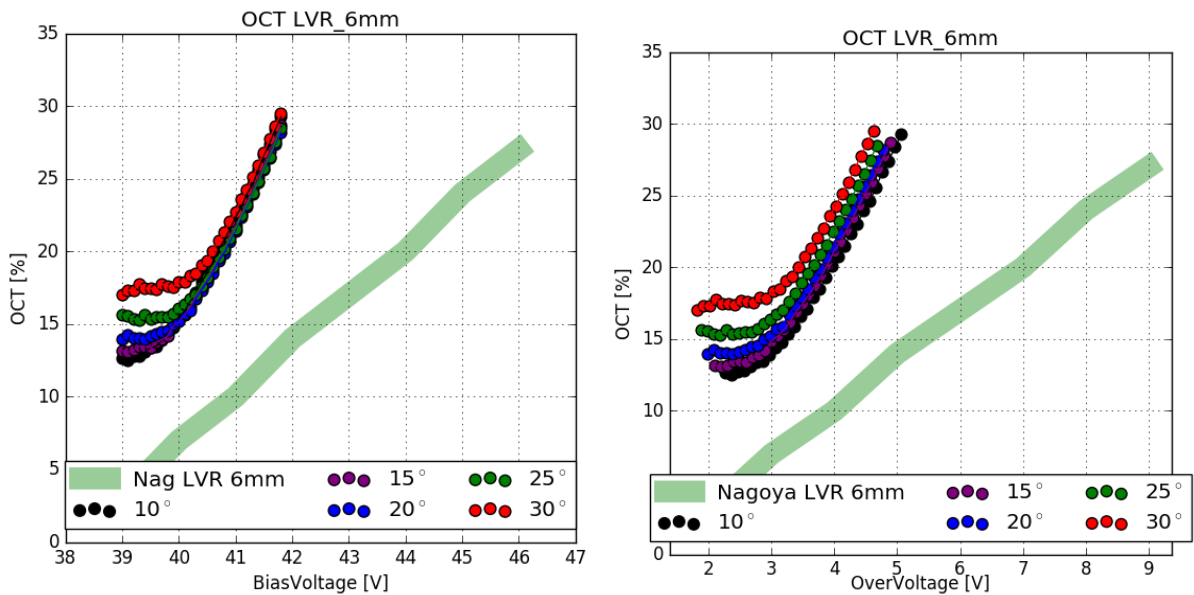


Figure 43: Optical Cross Talk of the HPK LVR 6mm pixel, plotted against over-voltage , bias-voltage and temperature.

6.6 SensL FJ60035 6mm 35 μ m

The SiPM by SensL with the designation FJ-60035 is another candidate device for use to populate the focal plane of CHEC-S. It is also a 6mm device, but with a much smaller cellsize of 35 μ m, using the TSV technology, so there are no wire-bonds present. This results in 22292 cells on a single pixel with a fill-factor of 75% . It is coated with plain glass. The recommended point of operation is around 30V bias-voltage, lower even than that of the HPK LVR prototypes. The device is, by the manufacturer, pre-mounted on a printed circuit board, called a test array. This test array contains a fast output, that directly couples to the cells, and a slow output, conventionally read out via the quench resistor. For the conducted tests, I used the fast output amplified with the MiniCircuits PreAMP supplied with 12V. The SensL device was the first device measured, therefore the analysis procedure used was an older iteration compared to the procedure for the Hamamatsu devices.

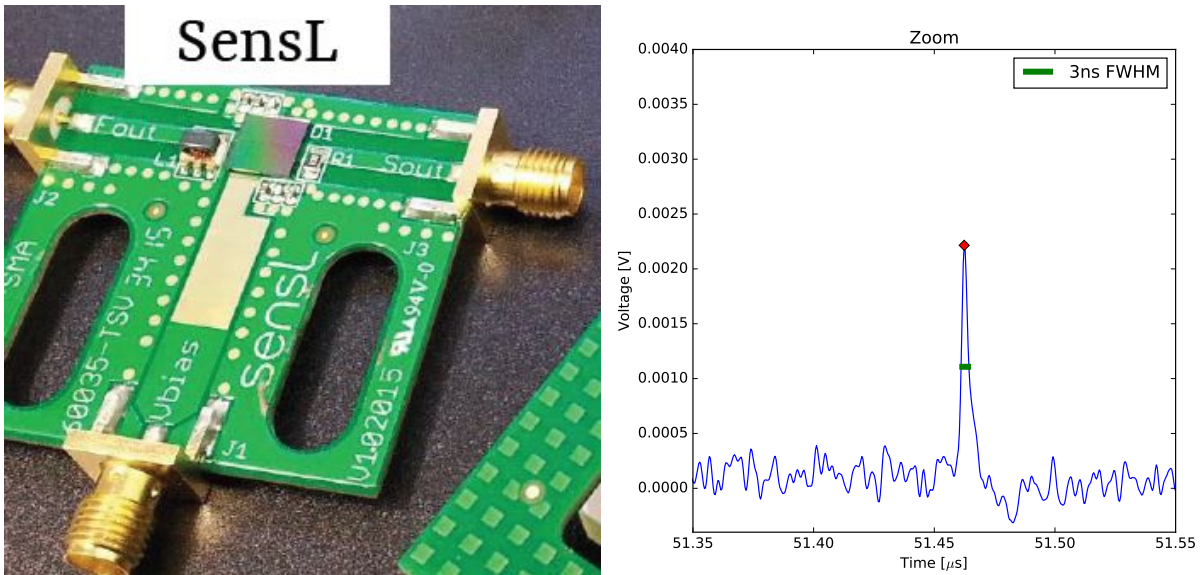


Figure 44: SensL Test Array and the average pulse shape at $V_{bias-voltage} = 29V$

6.6.1 Gain

Evaluating the SensL pulse area spectra shows the 1 p.e. position and Δ p.e. overlapping, so using the older analysis iteration introduced no error when evaluating the gain of the SensL device. It is clearly linear over a wide temperature range from -5°C to 35°C over an over-voltage ranging from 2V up to 8V. When plotted versus over-voltage the spread of the gain is even tighter signaling slight temperature independency, but still following the expected behaviour of decreasing with increasing temperature.

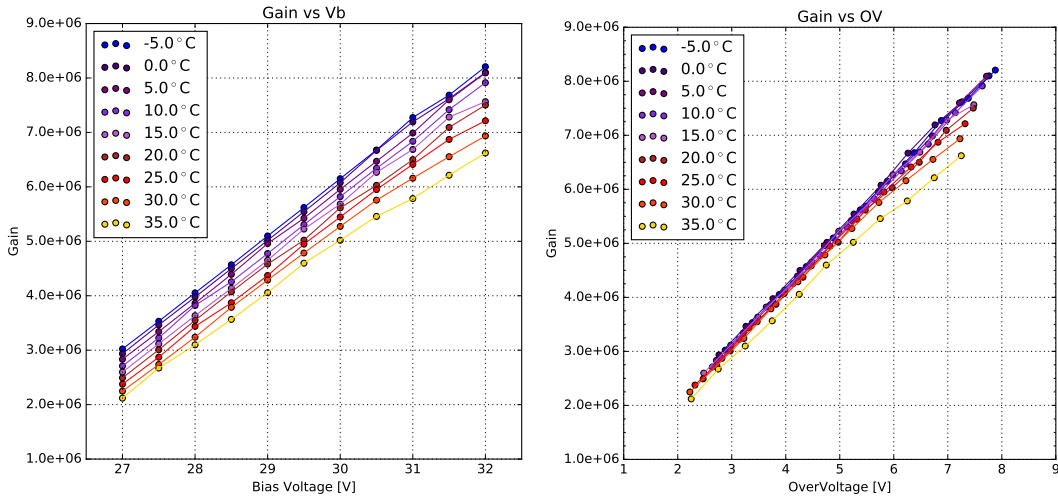


Figure 45: Gain of the SensL FJ-60035 test array, plotted against over-voltage , bias-voltage and temperature.

1191 6.6.2 Dark Count Rate and Optical Cross Talk 1192

1193 The DCR fig(46) also shows the expected behaviour. At very low temperatures the changes in
1194 rate over the over-voltage range is minimal. Increasing the temperature shows a rapid increase
1195 in thermally induced dark counts. The OCT fig(47) on the other hand is independent of the
1196 device temperature, also as expected. In both cases, the values agree with values derived from
1197 the datasheet.

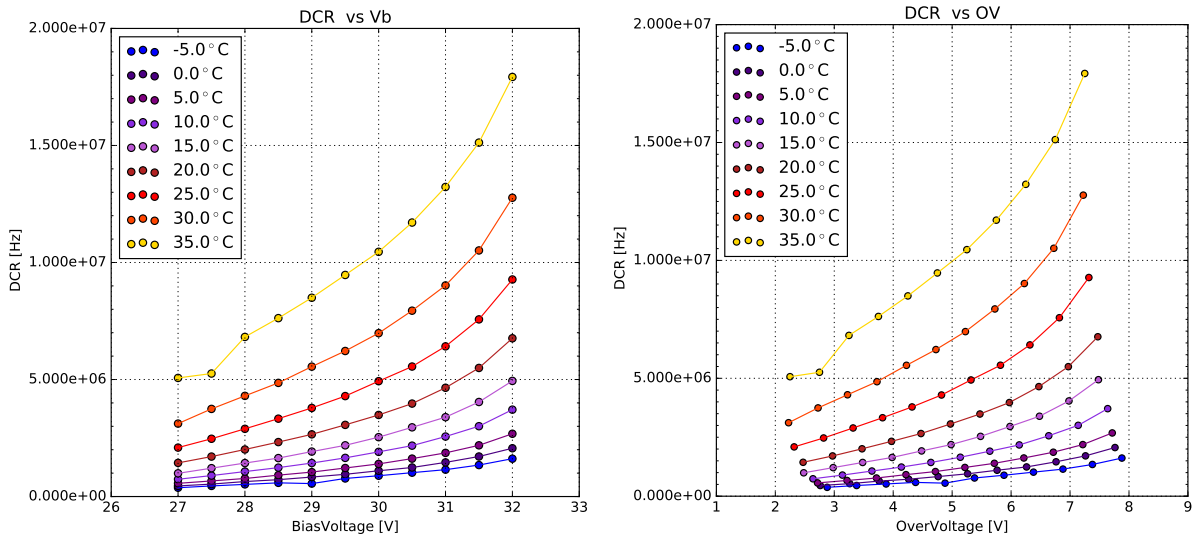


Figure 46: Dark Count Rate of the SensL FJ-60035 test array, plotted against over-voltage , bias-voltage and temperature. Datasheet values at $V_{OV} = 2.5$ V and 5 V at 25 °C are between 1.6 - 2.7 MHz and 2.9 - 5.7 MHz respectively.

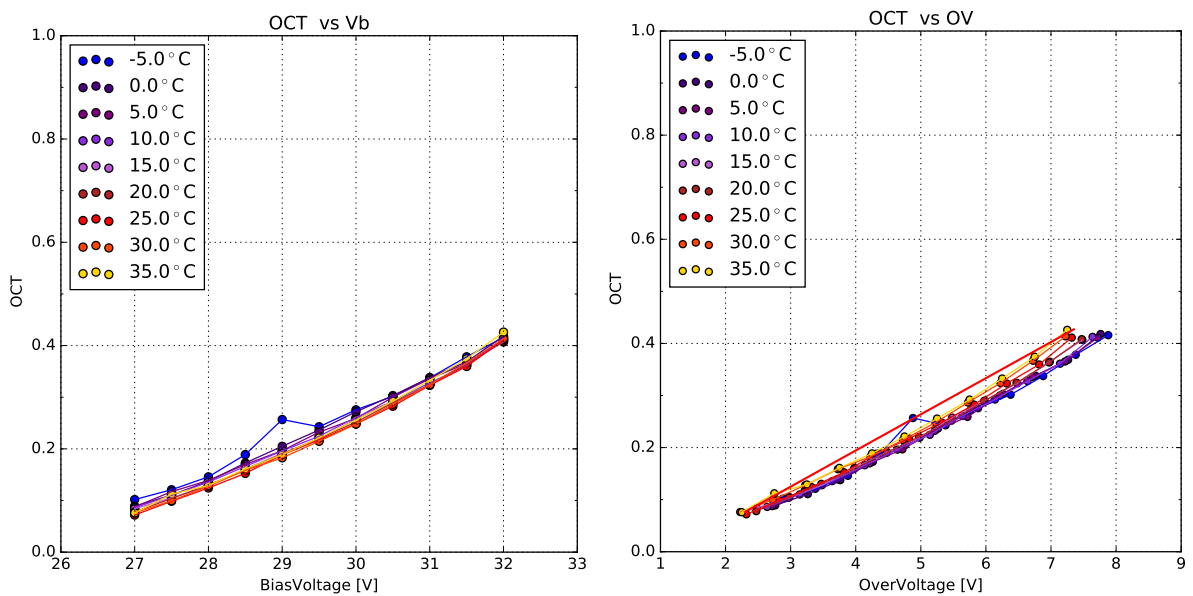


Figure 47: Optical Cross Talk of the SensL FJ-60035 test array, plotted against over-voltage , bias-voltage and temperature. OCT results of Nagoya University marked by the red line. Datasheet values at $V_{OV} = 2.5$ V and 5 V at 25 °C are 7% and 22% respectively.

1198
1199

7 Comparison

1200 A comparison of the performance of all devices is the significant step for choosing the SiPM
1201 later to be used in CHEC-S. In order to do this, all measured characteristics are compared versus
1202 over-voltage. Operation of the CHEC-S camera in GCT will come down to a decision between
1203 two operational points. The first point will be marked by an OCT of under 15%. Every other
1204 attribute of the SiPM at this over-voltage is then compared. This point will trade off precision
1205 for efficiency, a lower OCT makes real event detection easier, on the other hand, a lower PDE
1206 may forfeit a lot of potential data.

1207 The second point of operation is marked at the highest achievable Photon Detection Efficiency.
1208 This work does not involve PDE measurements, other groups are comissioned to determine the
1209 point of highest PDE. This point will assure the highest detection of event photons, but will
1210 trade that for an increase in detector noise, due to the higher DCR and more importantly OCT.

1211

1212 Comparing results to other groups is shown in figure(48), using different experimental se-
1213 tups and procedures and therefore also entirely different analysis techniques. The groups,
1214 that evaluate SiPMs, the University of Leicester, the University of Nagoya and the University
1215 of Catania, are all conducting fixed window readout of the SiPM after an expected light-pulse
1216 from a flasher-LED or pulsed laser.

1217

1218

1219
1220

7.1 Dark Count Rate

1221 Comparing the DCR of the measured devices and results from the other groups is shown in
1222 figure(48). The differences in analysis procedure will only have a slight impact on the pre-
1223 sumed Dark Count Rate, since all experiments record dark-count events over their respective
1224 acquisition time windows. On the other hand, if the readout window is sufficiently small, events
1225 originating from afterpulsing or delayed crosstalk could be missed. All groups experience the
1226 same multi-hit coincidence, meaning a light-event or dark-event coinciding with another, form-
1227 ing a (partial)multi p.e. event.

1228 Only two of the five measured devices have measurements result from other groups to compare,
1229 as it is not their focus. In the case of both, the LVR 6mm and the LCT5 7mm results can be
1230 discussed to some degree as matching. While the correlation is obvious for the LCT5 7mm de-
1231 vice figure(48)(red), where the covered measurement range in this work exceeds the external
1232 results, while matching and showing the same trend, the LVR 6mm results deviate. Between an
1233 over-voltage of 3V and 4V the results overlap, the trend on the other hand is obviously different.
1234 Additionally the limit on the higher range due to noise makes it impossible to compare against

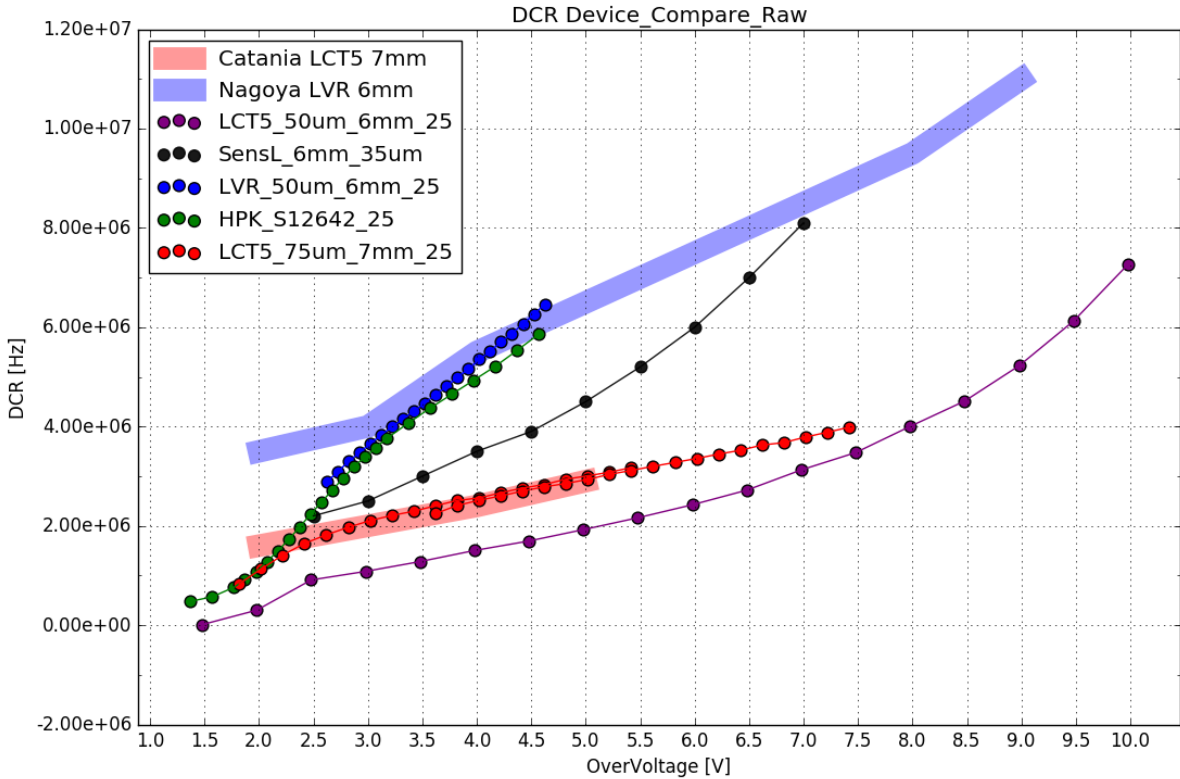


Figure 48: Dark Count Rate comparison of measured devices at 25°C. Description

1235 the full range measured by the external group, so the DCR for LVR 6mm must be labeled as not
 1236 matching.

1237 7.2 Optical Cross Talk

1238 The comparison of the OCT between the different groups and the results presented in this work
 1239 are dependent of the analysis and acquisition procedure. Extended trace analysis, utilized in
 1240 this work captures all aspects of the OCT, prompt and delayed as well as afterpulsing. The
 1241 procedure of time window analysis, utilized by the groups being compared to, are, due to their
 1242 limited window, either biased towards the prompt cross talk or in extreme cases, will not be
 1243 able to capture delayed cross talk or time-delayed afterpulsing at all. Comparing data analysis
 1244 techniques, for example, at the University of Leicester is therefore a vital step. Their approach
 1245 utilizes a pulsed laser as light source and involves no cooling of the SiPM tile. The waveforms
 1246 are extracted from the scope and a small time window is defined from the known time position
 1247 window of the incident pulse to search for peaks, find their value and generate a histogram. To
 1248 the pulse area histogram, a theoretical model of contributing factors is fitted. This theoretical
 1249 model simulates characteristics, updating continuously to find their correct values. Those values
 1250 are the full set of characteristics of the device in testing, among them: gain curve, breakdown-
 1251 voltage, OCT, PDE, noise, dynamic range, crosstalk probability.
 1252 There are a number of differences in their approach compared to the one utilized in this work,

1254 most important is the time window size. If the window after an incident pulse is too short, data
 1255 loss is a possibility, depending on the delay time of delayed cross-talk and afterpulsing assisted
 1256 by traps with long lifetimes. This is a problem, especially with devices of the LCT5 generation
 1257 implementing physical trenches isolating the cells and effectively reducing the prompt cross-
 1258 talk, here the contribution from the prompt cross-talk to the overall OCT is lowered. Missing
 1259 data from delayed cross-talk and afterpulsing, because it will not be recorded yet, would lead
 1260 to errors in the overall OCT results being lower than expected.
 1261

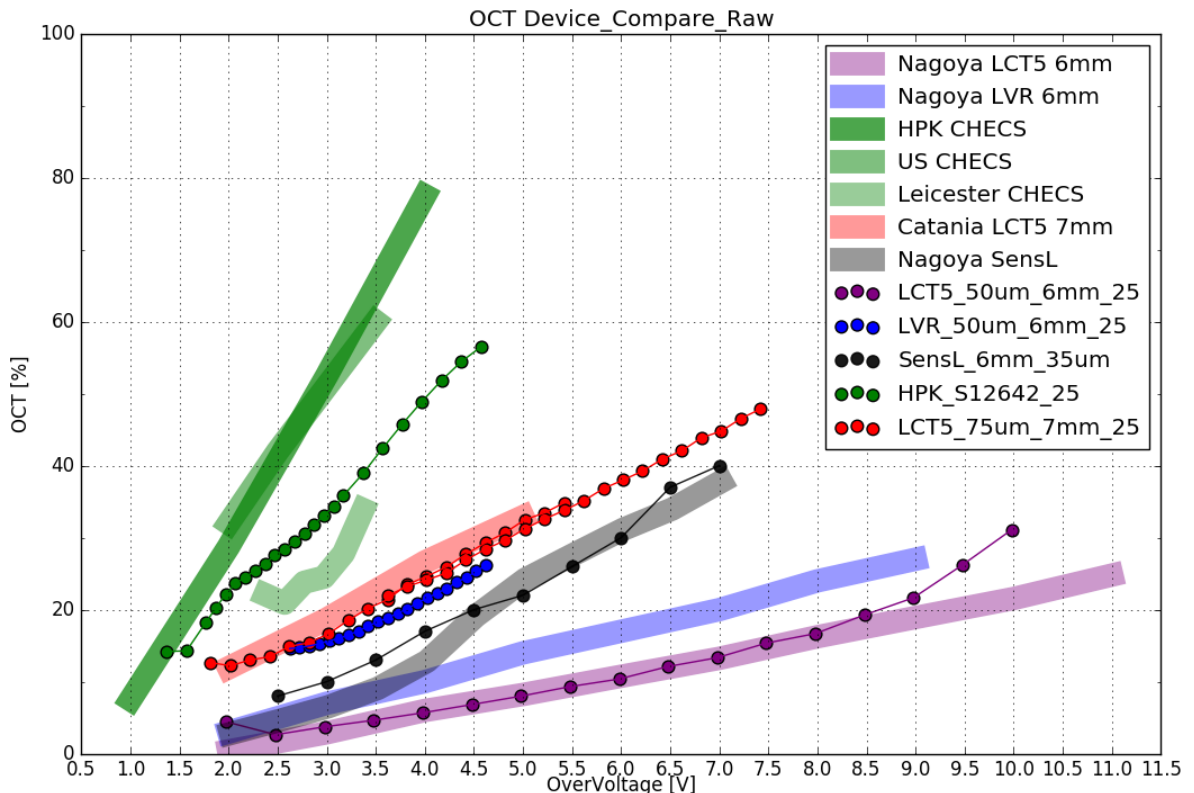


Figure 49: Cross Talk comparison of measured devices at 25°C. Description

1262 This is indeed the case for the S12642 tile in figure(49)(green). The light green bar below
 1263 (negative y-axis) the dotted data presented in this work shows the results form the University
 1264 of Leicester indeed being lower. In purple results of the LCT5 S13360 device with physical
 1265 trenches are shown. Compared to results from the University of Nagoya, there is a prominent
 1266 upturn at around an over-voltage of $\sim 8V$. This could be due to the differences in analysis tech-
 1267 nique. The University of Nagoya also employs time window analysis. LCT5 posseses lowered
 1268 prompt cross-talk probability, so the contribution of delayed cross-talk to the overall cross-talk
 1269 is higher than for S12642. With rising over-voltage the ratio between prompt and delayed
 1270 cross talk shifts towards a higher contribution from delayed cross-talk[14][20]. While at lower
 1271 over-voltages ($\sim 0.5V$) the cross-talk is nearly entirely dominated by the prompt cross-talk with
 1272 nearly no contribution of delayed cross-talk, at ($\sim 2V$) contributions are mostly equal and at

1273 high over-voltages ($\sim 7V$) the contribution of delayed cross-talk is expected to be above 80%,
1274 probably due to higher penetration depth and avalanche probability.
1275 Results of the LCT5 7mm device from both groups mostly overlap, the slight shift between them
1276 is most likely caused by a small error in the breakdown-voltage calculation, due to no cooling
1277 of the tile in experiments involving light. In addition, the slope of both results seems to be mostly
1278 equal, and the extended range measurement, overlapping with the low-range results confirms
1279 that.
1280 Even though results from 3 different groups mostly correlate, or have at least partially un-
1281 derstood differences, the OCT of LVR 6mm figure(49)(blue) compared to the results from the
1282 University of Nagoya do not show any correlation at all. This is concerning, because comparing
1283 S13360 (purple) to the same group showed strong correlation over a wide over-voltage range.
1284 Since there is also no datasheet present yet, this device is a prototype, the assumption is that
1285 the device examined is physically different than the device present at Nagoya. It may just be
1286 a difference in coating, which combined with the TSV technology could lead to the present
1287 uncorrelation[20].

1288 7.3 Point of Operation Comparison

1290 A different method of comparison involves the two proposed points of operation, illustrated
1291 at the beginning of section(7). By adding the PDE measured by external groups, all three
1292 characteristics can be illustrated together. Figure(??) shows the comparison result of the SiPMs
1293 examined in this thesis. A minimal OCT point of 15% in the left column, and the maximum PDE
1294 points in the right column, both include external PDE measurements.

1295 At the first, minimal OCT, operation point the LCT5 6mm (S13360) device is favorable, since it
1296 possesses a high PDE of 49% with a fairly low DCR below the expected NSB. The currently used
1297 SiPM in CHEC-S only reaches 25% according to datasheet values.

1298 The four HPK devices (the first four in the list), all have a maximum achievable PDE around the
1299 same level, $\sim 50\%$. The difference in DCR and OCT at this level is the deciding factor. While
1300 the current CHEC-S SiPM reaches a very high OCT level of $\sim 50\%$, the newer generation HPK
1301 SiPMs, with physical trenches, are well below at $\sim 25\%$. The DCR on the other hand seems to be
1302 similar for each device. The LCT5 7mm SiPM at this point of operation seems to have the lowest
1303 DCR among them, but the measurements of this device have not yet reached the maximum PDE
1304 value and will be extended, higher PDE is possible.

1305 In both cases, the PDE of the SensL SiPM is not competitive.

1306 7.4 Photon Detection Efficiency

1308 The measurement technique in this work utilizes only dark counts and aims at giving an under-
1309 standing of the OCT and temperature dependencies of the different SiPMs proposed, therefore
1310 no PDE measurements are possible. The point of operation with the highest PDE as well as the

Device	Min. OCT			Max. PDE		
	OCT	DCR	PDE	OCT	DCR	PDE
CHECS	15%	0.5 MHz	25% (DS)	50%	5 MHz	48% (DS)
LCT5 6mm	15%	3.4 MHz	49% (Nagoya)	22%	5 MHz	51% (Nagoya)
LCT5 7mm	15%	2.0 MHz	42% (Catania)	25%	2.5 MHz	53% (Catania)
LVR 6mm	15%	2.5 MHz	43% (Nagoya)	>27%	>6MHz	>50% (Nagoya)
SensL	15%	3.0 MHz	37% (Nagoya)	30%	6 MHz	40% (Nagoya)

Figure 50: Comparison table of the measured devices based on the two proposed operation points for CHEC-S. First point represents minimal achievable OCT, second point represents maximum achievable PDE. PDE values taken from results of other groups and datasheet values. Note that the LCT5 6mm device can achieve even lower OCT values ($\sim 3\%$ at $V_{ov} = 2.5$)

1311 PDE versus OCT behaviour is determined by a different group in Japan, at the University of
 1312 Nagoya. A figure showing the behavior of PDE versus OCT is the usual procedure of comparing
 1313 SiPMs, it gives a correlated overview of the two most significant characteristics. This gives
 1314 insight of the capabilities of the different devices compared to the two proposed points of op-
 1315 eration in section(7.3). For consistency and to make comparison between group results easier,
 1316 the PDE ascertained by the groups, of devices in common, compared to the resulting OCT from
 1317 this work produces figure(51).

1318

1319 Comparing all devices at the two proposed points of operation produces the table in
 1320 figure(50). This table together with figure(51) of the 5 measured devices in this thesis, where
 1321 PDE data is accesible, is used to confirm results between groups and assist in the decision on
 1322 the most viable SiPM for CHEC-S. The final decision will be taken by the GCT group based on
 1323 measurements on substantially more devices (see section(H), for the complete list).

1324 The PDE of SiPMs, when plotted versus the corresponding OCT at a common over-voltage point
 1325 show the behaviour in figure(51). A clearly visible saturation after a certain OCT marks the
 1326 point, from where an increase in power no longer increases photon-detection capabilities. An
 1327 increase in OCT without rising PDE would have a adverse effect on the detectors resolution.

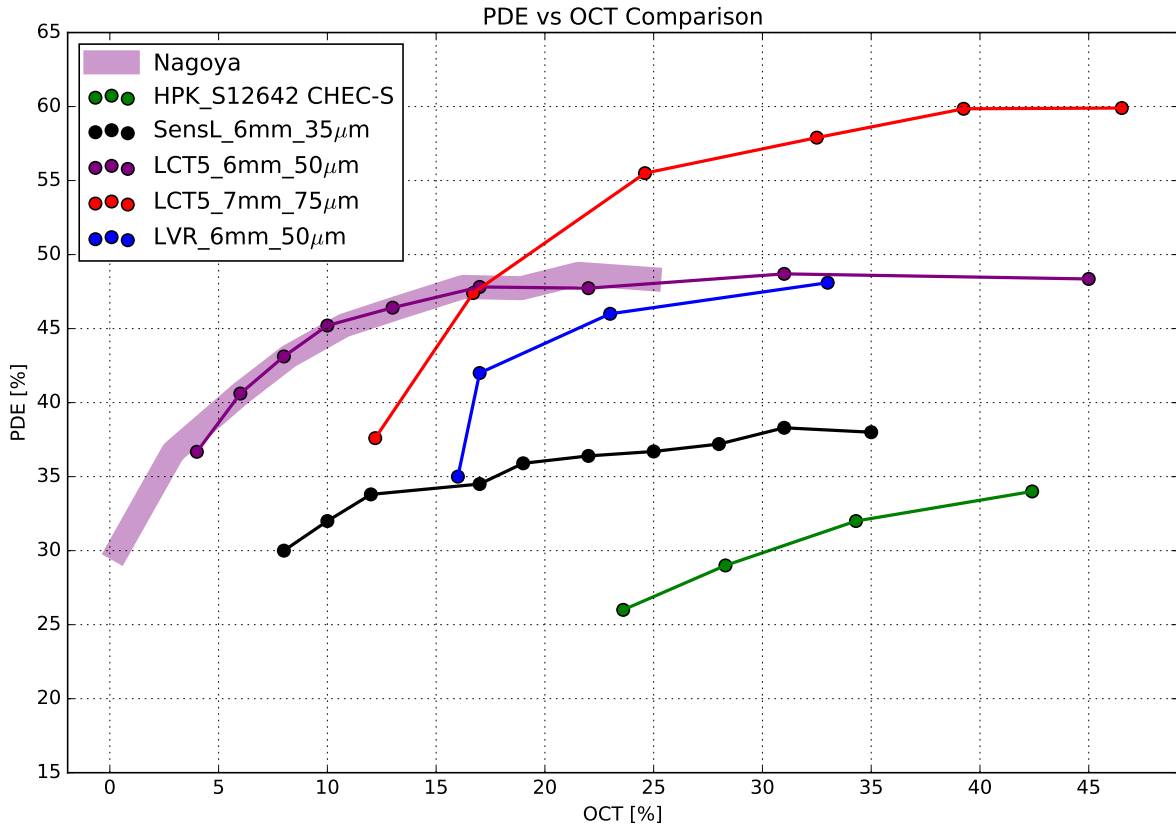


Figure 51: PDE results from the University of Nagoya parametrized with OCT results from this work, where available. PDE measurements at $\lambda = 400\text{nm}$. The faded purple bar shows measurements of the University of Nagoya. An optimum device for IACT application would be in the upper left region.

- 1328 The prototype LCT5 7mm fig(51)(red) device reaches the highest PDE. This is expected for de-
 1329 vices with larger cell-size and pixel-size, leading to a higher fill-factor. The increase in size and
 1330 therefore PDE comes with a trade-off, increasing size comes with a rise of DCR and OCT, which
 1331 are very high at this point (at $\sim 25\%$).
 1332 The commercially available LCT5 6mm (HPK S13360) SiPM shows the most promising results.
 1333 It reaches a high PDE very quickly compared to its OCT, with $\sim 47\%$ before the OCT reaches
 1334 20%. Compared to this, the OCT of the LVR 6mm at a point where the PDE saturates and
 1335 reaches the same PDE is very high.
 1336 The LCT5 6mm device seems the most promising for the low-OCT point, while the LCT5 7mm
 1337 device would be the choice at the high PDE point. Being a fairly new technology, the LVR device
 1338 is being developed and will be competitive.
 1339 Due to the low fill-factor, the PDE of the SensL FJ60035 device is not competitive. The HPK
 1340 S12642 device is clearly sub-optimal for CHEC-S, but will still be used for initial tests. It shows
 1341 a very low PDE compared to a very high OCT at this point.

1342
1343

8 Conclusion and Outlook

1344 Over the course of this work five new-generation SiPMs have been examined in dark conditions,
1345 for their possible use in single photon detection for the high energy instrument of the Cherenkov
1346 Telescope Array.

1347 A lasting experimental teststand has been developed, that is capable to be upgraded for future
1348 illumination tests. It is a reference to other groups, who will build similar setups for the mass-
1349 production of the CHEC camera. The teststand involves a climate chamber for temperature
1350 regulation, that functions as a light tight box. For each SiPM pre-existent shaping electronics
1351 has been modified in order to achieve a preferred signal. Data acquisition code was developed
1352 to control the experimental parameters of the teststand remotely, and storing all experimental
1353 data from the internal memory of the oscilloscope on a Lab-PC. A data analysis procedure has
1354 been designed and developed to analyze the data offline, both were developed in python.

1355 Experimental studies of the SiPMs showed better performance at lower temperatures. In obser-
1356 vation conditions temperatures lower than 25 °C are unfortunately not expected. Even at those
1357 temperatures SiPMs are a strongly considered candidate.

1358 By now, only dark measurements can be conducted, but once a tunable lightsource and
1359 monochromator is installed, light measurements are possible. Before that, a solution for the
1360 potential warm-up of the SiPM surface must be found.

1361 The work on both, the teststand and the analysis method, will be expanded in the future. Fol-
1362 lowing this work the involved groups start to exchange the physical devices for better coverage
1363 of the measurement results.

1364

1365 Comparing the devices measured in this work showed the LCT5 generation to be favorable
1366 for both proposed points of operation of CHEC-S. There is a new technology, LVR, that seems
1367 promising and is still being developed.

1368 Correlation between group results

1369 '_____>'

1370 For that purpose 5 different SiPM from two manufacturers have been examined.

1371 9 Glossary

- 1372
- 1373 1. SiPM - Silicon Photomultiplier
 - 1374 2. IACT - Imaging Atmospheric Cherenkov Telescope
 - 1375 3. CTA - Cherenkov Telescope Array
 - 1376 4. LST - Large Sized Telescope
 - 1377 5. MST - Medium Sized Telescope
 - 1378 6. SST - Small Sized Telescope
 - 1379 7. GCT - Gamma Cherenkov Telescope
 - 1380 8. CHEC - Compact High Energy Camera
 - 1381 9. HPK - Hamamatsu Photonics K.K.
 - 1382 10. SensL - Sense Light

1383 1384 10 Bibliography

1385 1386 References

- 1387 [1] Jim Hinton et al. *Teraelectronvolt Astronomy* Ann. Rev. Astron. Astrophys., 47:523
- 1388 [2] The CTA Consortium *Design Concepts for the Cherenkov Telescope Array CTA, An Advanced*
1389 *Facility for Ground-Based High-Energy Gamma-Ray Astronomy* ; arXiv:1008.3703v3 [astro-
1390 ph.IM] 11 Apr 2012
- 1391 [3] Teresa Montaruli et al. *The small size telescope projects for the Cherenkov Telescope Array*
1392 arXiv:1508.06472v1 [astro-ph.IM]
- 1393 [4] *The ASTRONET Infrastructure Roadmap* ISBN: 978-3-923524-63-1
- 1394 [5] Jim Hinton et. al *Seeing the High-Energy Universe with the Cherenkov Telescope Array* As-
1395 troparticle Physics 43 (2013) 1-356
- 1396 [6] R. López-Coto for the HAWC collaboration *Very high energy gamma-ray astronomy with*
1397 *HAWC* arXiv:1612.09078v1 [astro-ph.IM] 29 Dec 2016
- 1398 [7] John Murphy *SensL J-Series Silicon Photomultipliers for High-Performance Timing in Nuclear*
1399 *Medicine*
- 1400 [8] A. N. Otte et al. *Characterization of three high efficient and blue sensitive Silicon photomul-*
1401 *tipliers* arXiv:1606.05186v2 [physics.ins-det] 26 Jan 2017
- 1402 [9] A. Bouvier et al. *Photosensor Characterization for the Cherenkov Telescope Array: Silicon*
1403 *Photomultiplier versus Multi-Anode Photomultiplier Tube* ; arXiv:1308.1390v1 [astro-ph.IM]
1404 6 Aug 2013
- 1405 [10] V. Vassilieva , S. Fegan *Wide field aplanatic two-mirror telescopes for ground-based*
1406 *gamma-ray astronomy* Astropart. Phys. 28 (2007) 10, [astro-ph/0612718] arXiv:astro-
1407 ph/0612718v2 12 Apr 2007
- 1408 [11] A. Zech, J.-P. Amans, S. Blake et al. *SST-GATE: A dual mirror telescope for the Cherenkov*
1409 *Telescope Array* arXiv:1307.3035v1 [astro-ph.IM] 11 Jul 2013
- 1410 [12] Julien Rousselle et al. *Construction of a Schwarzschild-Couder telescope as a candidate for*
1411 *the Cherenkov Telescope Array: status of the optical system* arXiv:1509.01143v1 astro-ph.IM
- 1412 [13] J. Rosado S. Hidalgo *Characterization and modeling of crosstalk and afterpulsing in Hamamatsu*
1413 *silicon photomultipliers.* arXiv:1509.02286v2 [physics.ins-det] 21 Oct 2015
- 1414 [14] K. Boone, Y. Iwai, F. Retiere, C. Rethmeier *Delayed avalanches in Multi-Pixel Photon Counters*
1415 arXiv:1703.04651v1 [physics.ins-det] 14 Mar 2017

- 1416 [15] Robert G. Wagner et al. *The Next Generation of Photo-Detectors for Particle Astrophysics*
1417 arXiv:0904.3565v1 [astro-ph.IM] 22 Apr 2009
- 1418 [16] *Opto-semiconductor handbook Chapter 03 Si APD, MPPC*. Hamamatsu Photonics K.K.
- 1419 [17] Jonathan Biteau et al *Performance of Silicon Photomultipliers for the Dual-Mirror Medium-*
1420 *Sized Telescopes of the Cherenkov Telescope Array* arXiv:1508.06245v1 [astro-ph.IM] 25 Aug
1421 2015
- 1422 [18] Richard White *private communication*. 2017
- 1423 [19] Hirojamina *private communication*. 2017
- 1424 [20] Koei Yamamoto *private correspondence*. 2016
- 1425 [21] Luigi Tibaldo *Initial testing at MPIK (wb July 18 2016)* July 2016
- 1426 [22] T. C. Awes et al. *Configurable electronics with low noise and 14-bit dynamic range for*
1427 *photodiode-based photon detectors* Nuclear Inst. and Methods in Physics Research, Mai 2006
- 1428 [23] Maurice Stephan. *Design and Test of a Low Noise Amplifier for the Auger Radio Detector*
1429 Diploma Thesis, RWTH Aachen University, July 2009
- 1430 [24] Hiro Tajima *Roadmap for Procurement of SiPMs*, GCT Meeting, Amsterdam, February
1431 15–17, 2017
- 1432 [25] http://astro.desy.de/gamma_astronomy/cta/index_eng.html
- 1433 [26] [http://www.ung.si/en/research/laboratory-for-astroparticle-physics/
1434 projects/cta/](http://www.ung.si/en/research/laboratory-for-astroparticle-physics/projects/cta/)
- 1435 [27] [http://www.ung.si/en/research/laboratory-for-astroparticle-physics/
1436 projects/fermi-lat/](http://www.ung.si/en/research/laboratory-for-astroparticle-physics/projects/fermi-lat/)
- 1437 [28] http://212.71.251.65/aspera//index.php?option=com_content&task=blogcategory&id=111&Itemid=234

11 Appendix

A CTA

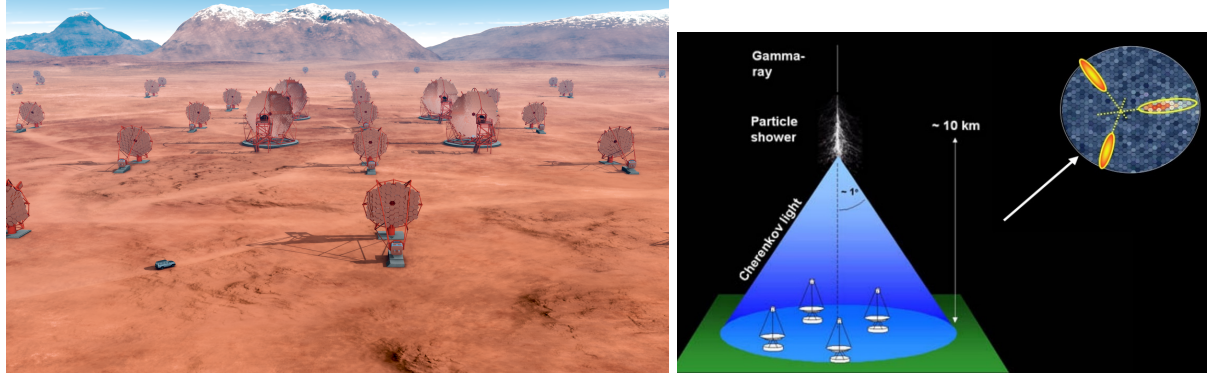


Figure 52: A render of the finished CTA Array at the site in Chile (left) with visible LSTs and MSTs, and the Shower Path Reconstruction technique of the stereoscopic view employed by current IACT experiments like HESS, MAGIC, VERITAS (right).

B progenitor experiments of CTA



Figure 53: IACT Projects: HESS in the Khomas Highland, Namibia. MAGIC at the Roque de los Muchachos Observatory on La Palma , one of the Canary Islands. VERITAS at Mount Hopkins, Arizona, USA

C OCT dependency on cellsize

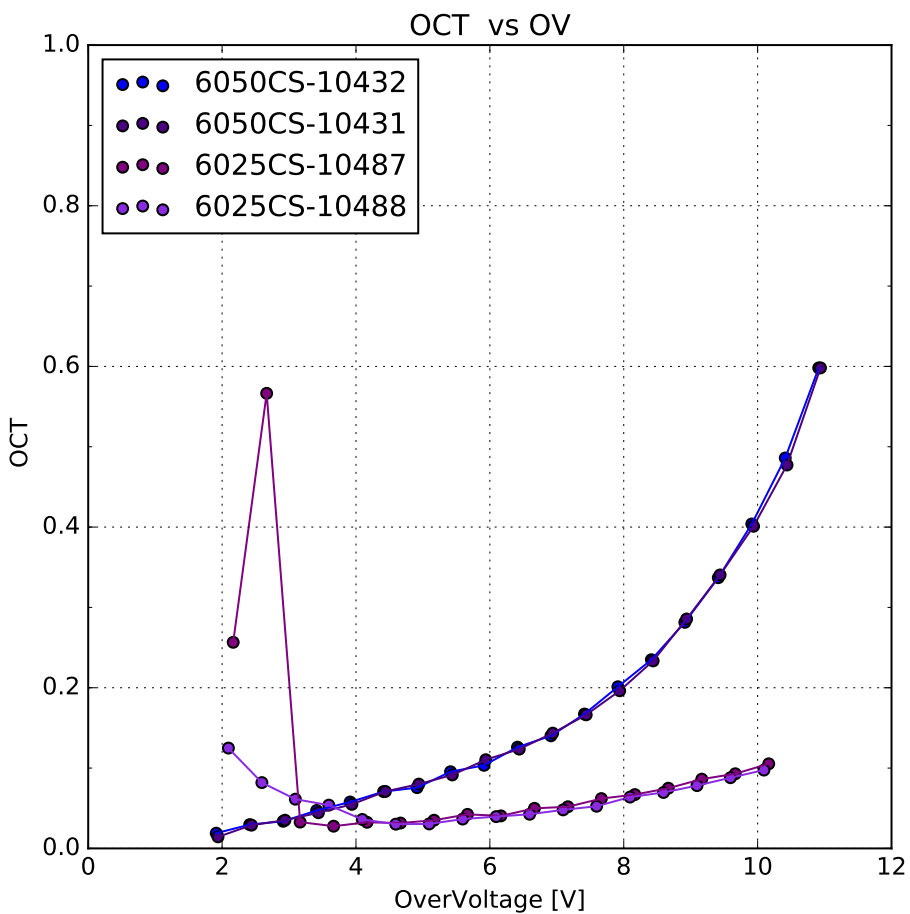
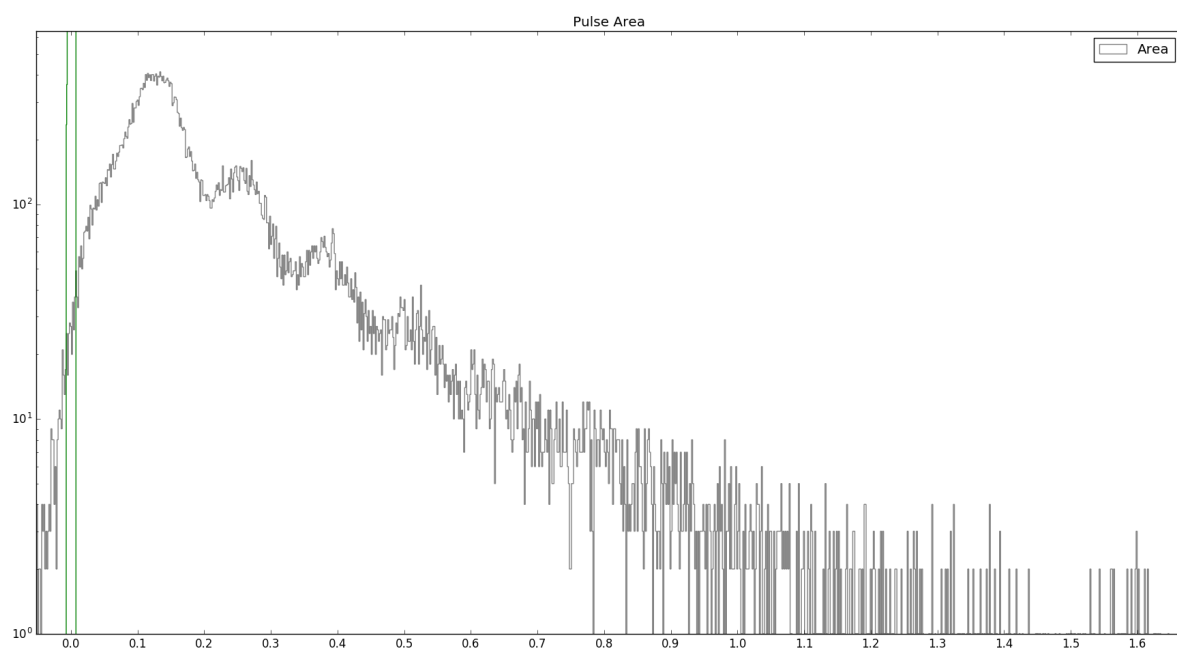
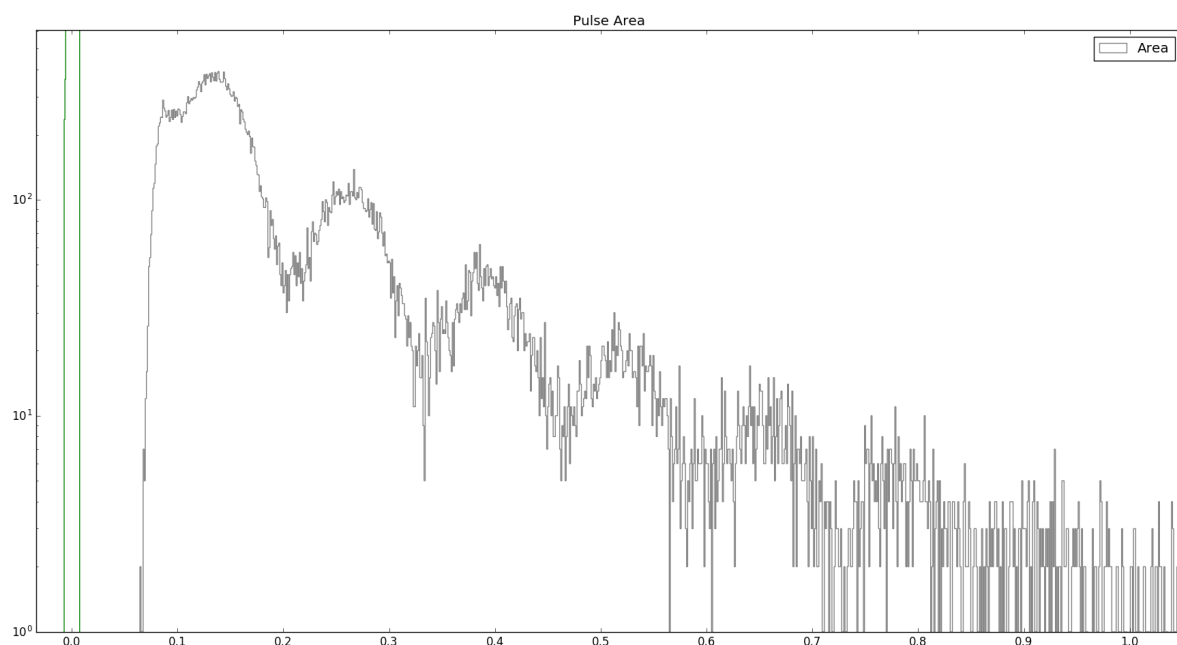


Figure 54: Results of the OCT of two sets of two similar HPK S13360 devices, that only differ in their respective cell-size. HPK S13360 is the first device incorporating physical trenches in the upper layer, optically isolating each cell. Consequence to this is a drastic reduction in prompt cross-talk. Delayed cross-talk and afterpulsing are basically unaffected. Upscaling the $25\mu\text{m}$ results shows an overlap between the 2, see text.

In figure(54) the results of the complete OCT of 2 sets of $50\mu\text{m}$ and $25\mu\text{m}$ HPK S13360 devices are shown. Plotting the results of 2 similar devices, only different in their cell-size, and then multiplying the $25\mu\text{m}$ results by the factor derived from their difference in area, here 4, a correlation is visible. Scaling up the OCT of the $25\mu\text{m}$ cell, shows an overlap between the 2 cell-sized pixels. This means, that the OCT is directly area and therefore cell-size dependent. Research by J. Rosado and S. Hidalgo [13] on the cross-talk probability of Hamamatsu SiPMs showed through Monte Carlo simulation, that the prompt crosstalk mostly takes place in a small area of pixels (~ 8) around the primary one. Which means, that the cross-talk is directly increasing with increasing cell-size, or in other words: with chance to diffuse to a neighboring cell. Small cells reduce the chance, as there is less area to a neighboring cell to pass through. Since the measurements conducted by me do not differ between the range of secondary

¹⁴⁵⁸ avalanche effects, the OCT shown contains every aspect, prompt and delayed as well as af-
¹⁴⁵⁹ terpulsing.

D Pulse Area Spectra of different integration window widths



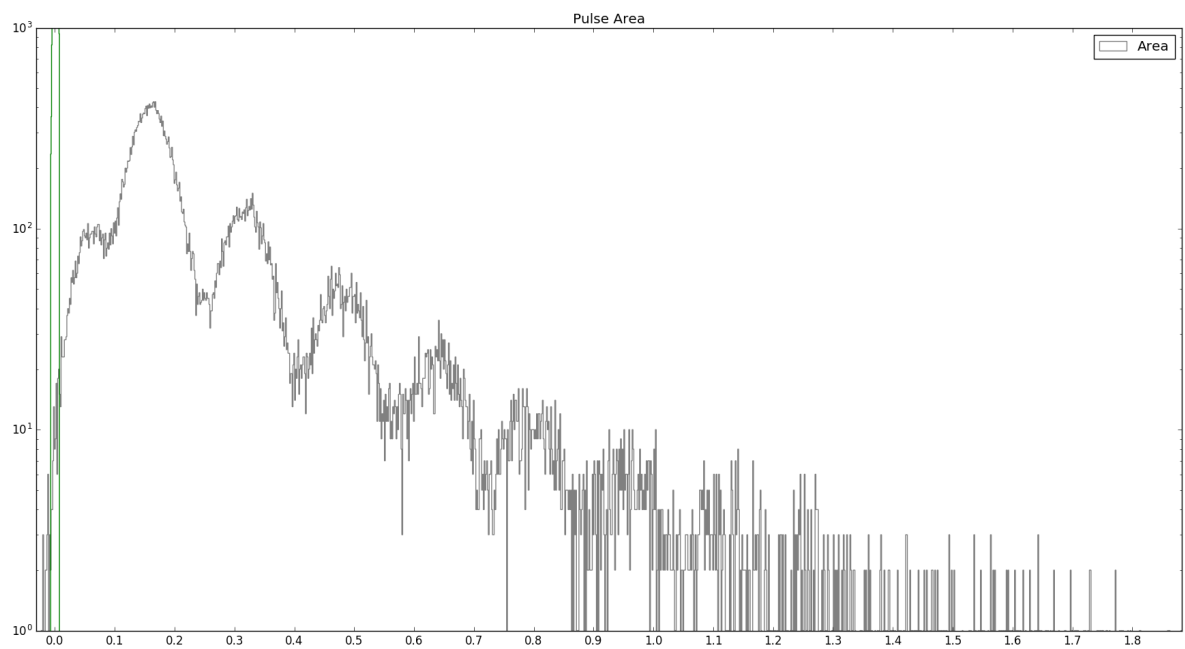


Figure 55: Pulse Area Spectra with window widths of 5 left 5 right (top), 5 left 20 right (middle), 10 left 10 right (bottom) bins respectively. Left of the 1p.e. peak of the top picture a part of the 0p.e. peak is visible. The middle figure shows the distortion an asymmetrical integration window causes. The bottom figure is the employed integration window to derive the pulse area histogram.

E Pulse Area Spectra examples

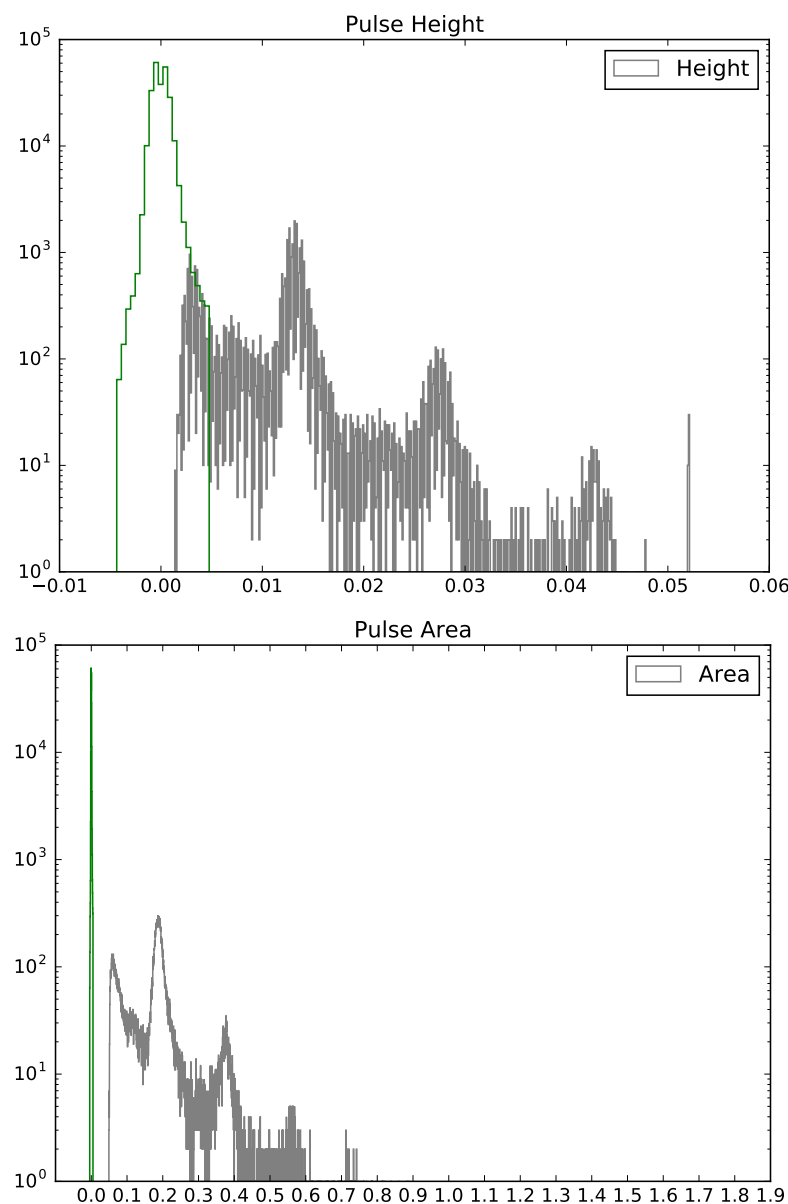


Figure 56: Pulse height and pulse area spectrum of the S12642 device at $V_b = 58V$ and $T = 25^\circ C$. The x-axis is pulse height and pulse area respectively and the y-axis is number of counted pulses

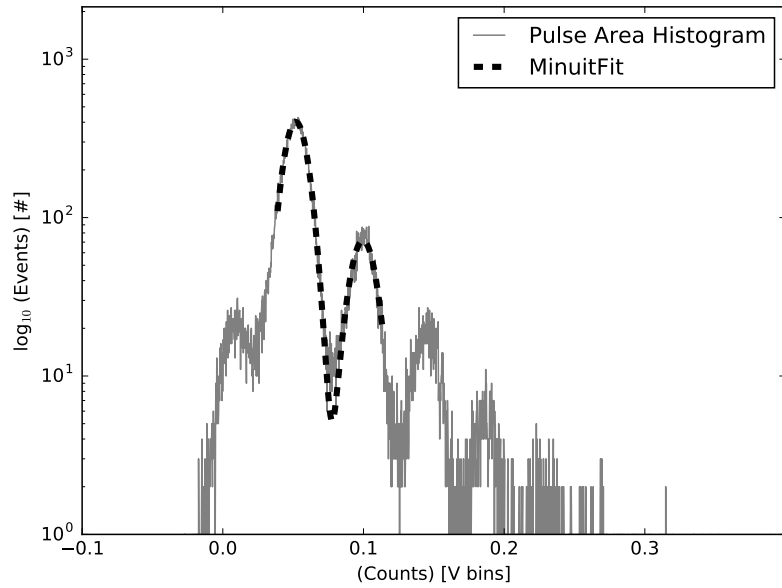


Figure 57: Pulse area spectrum of the S13360 LCT5 6mm device at $V_b = 56.2\text{V}$ at $T = 25^\circ\text{C}$. The x-axis is pulse height and pulse area respectively and the y-axis is number of counted pulses. The dashed black line shows the fitted function.

F BreakdownVoltage

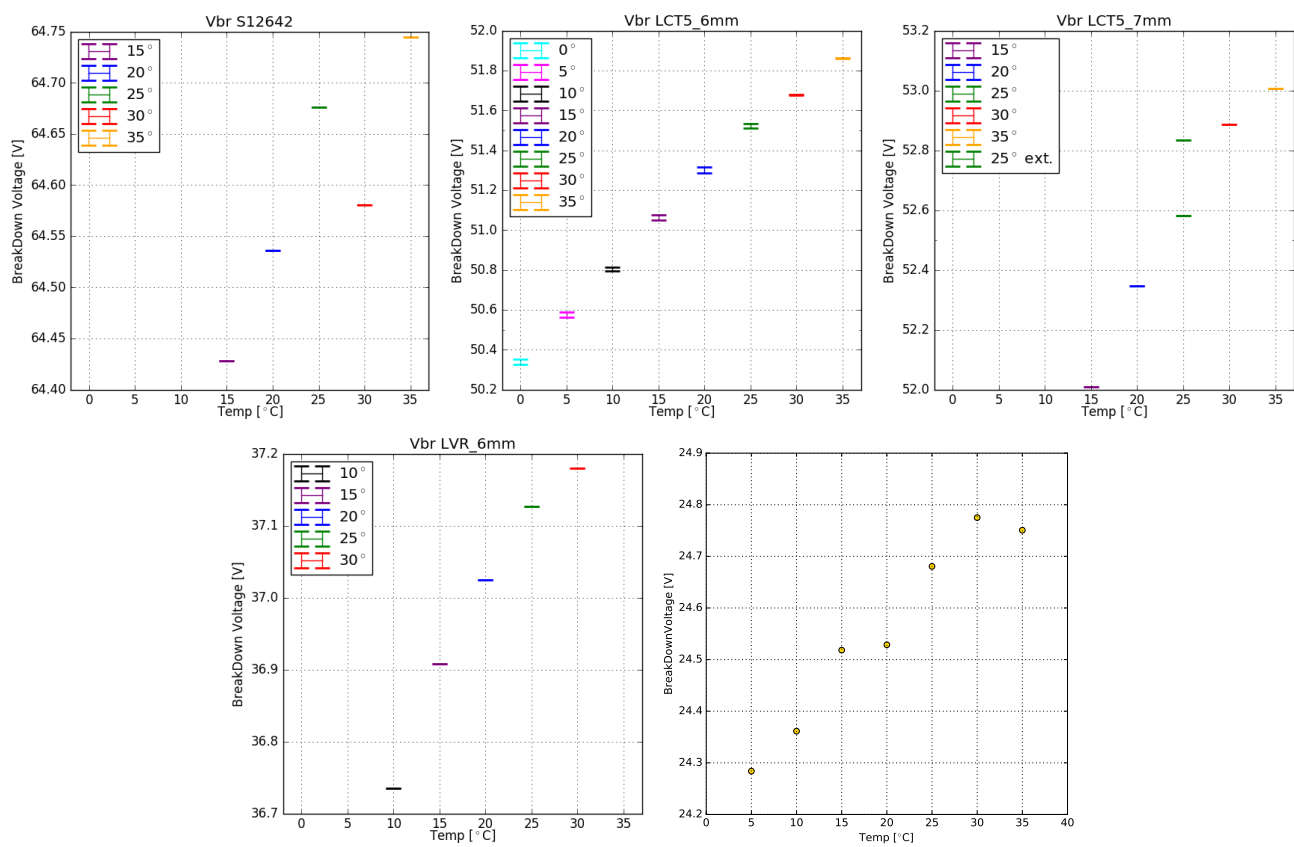


Figure 58: Dependency of the breakdown-voltage of temperature for the 5 measured devices.

For LCT5 7mm , the extended range measurement adds an extra datapoint at 25 °C
 HPK S12642 (CHEC-S) (top left) ; HPK LCT5 6mm (top middle) ; HPK LCT5 7mm (top right) ; HPK LCT5 LVR 6mm (bottom left) ; SensL FJ60035 (bottom right).

Device	$\Delta V / T$ [mV/°C]
CHECS	13.1 ± 4.1
LCT5 6mm	43.5 ± 0.4
LCT5 7mm	53.0 ± 4.0
LVR 6mm	25.6 ± 2.6
SensL	15.0 ± 1.1

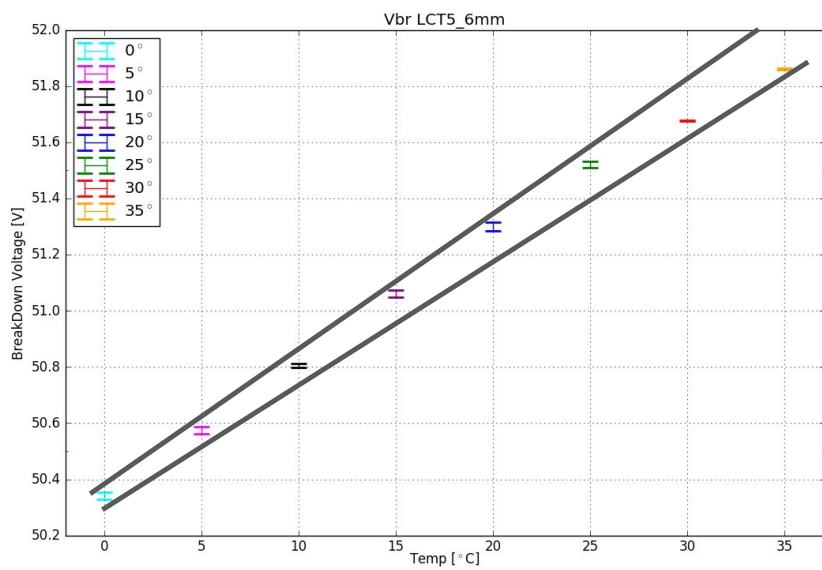
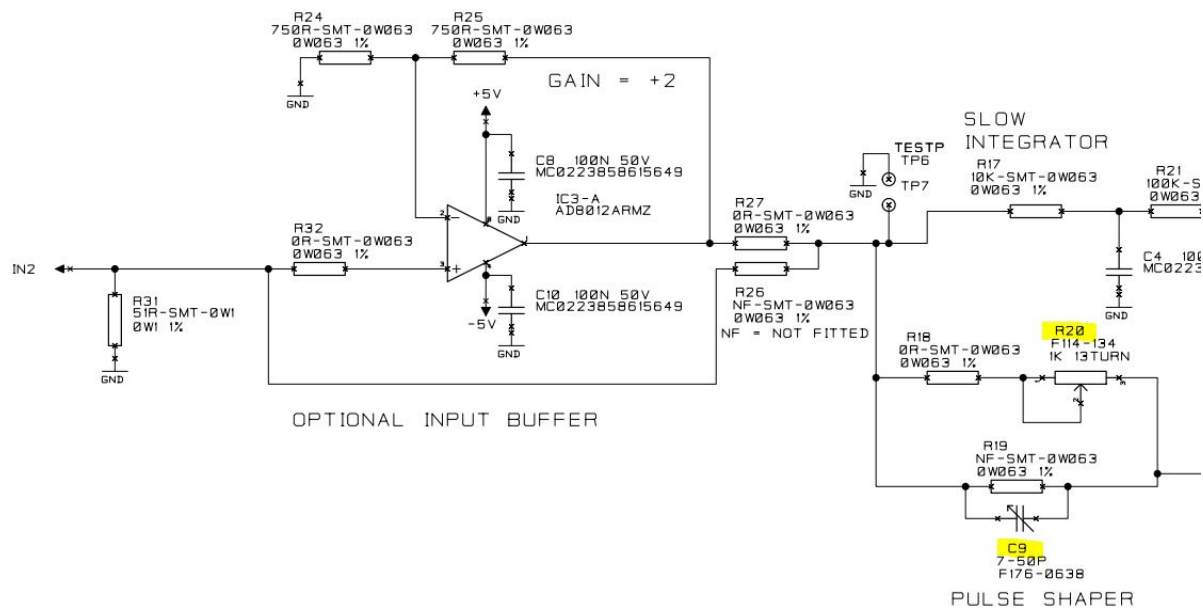


Figure 59: The extracted breakdown-voltage dependence of all measured devices, derived from two regression lines and their mean. For some devices the breakdown-voltage dependency is known through datasheet values. S12642 = 60 mV/°C, S13360 = 54 mV/°C, SensL FJ60035 =<21.5 mV/°C

G Shaper**Figure 60:** Full schematic of the shaper developed at the University of Leicester.

H SiPM list tested at University of Nagoya

MAKE YOUR OWN DAMN TABLE :)[24]

Manufacturer	pixel size [mm]	cell size [μm]	coating	connection	specifics	pre-Amp
HPK S12642-1616PA-50 *CHEC-S SiPM	3	50	SR	TSV	no trenches	CHEC-S buffer
HPK LCT5 S13360-6050CS	6	50	SR	wire-bonds	trenches	MS 13V
HPK LCT5 6.975MM-SIL Single	6.915	75	SR	wire-bonds	trenches	MS 8V
HPK 6050HWB-LVR-LCT	6	50	SR	TSV	trenches	MS 13V
SensL FJ60035	6	35	glass	TSV	no trenches	MS 15V

Figure 61: List of SiPM devices which results are presented in this work. *(SR: silicon resin , MS: MiniCircuits , TSV: through silicon via)

I CHEC-S pixel comparison

1471 Comparison of results from 10 different pixels on the CHEC-S (HPK S12642-1616PA-50) array.
1472 Every pixel is analyzed with the same technique and analysis parameters.

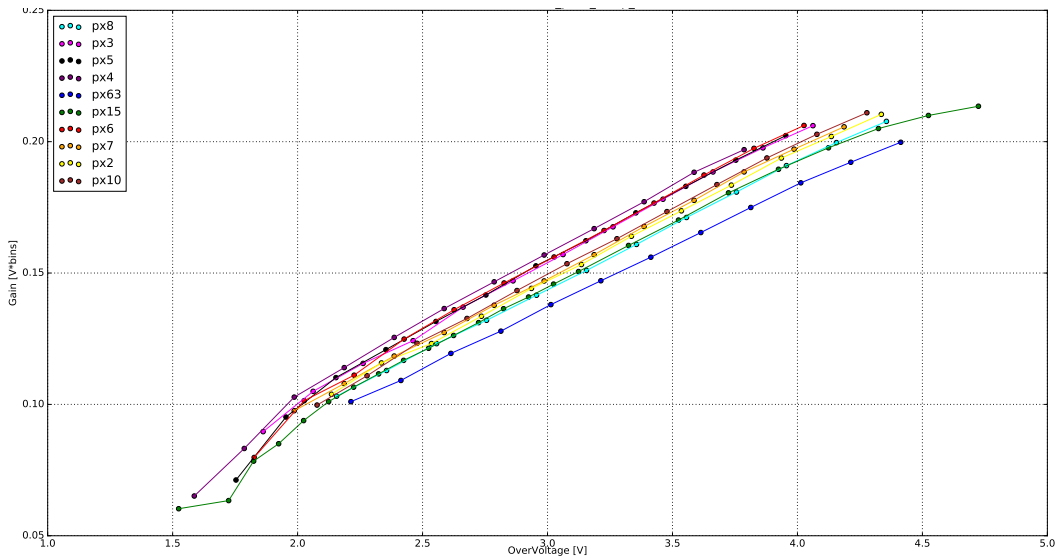


Figure 62: Gain comparison of 10 different pixels of the CHEC-S (HPK S12642-1616PA-50) array

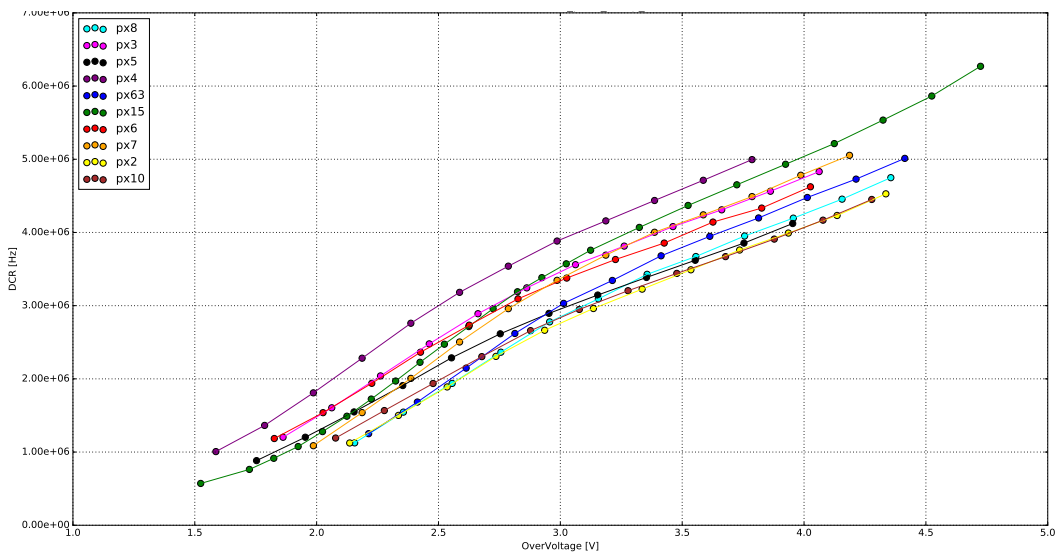


Figure 63: DCR comparison of 10 different pixels of the CHEC-S (HPK S12642-1616PA-50) array

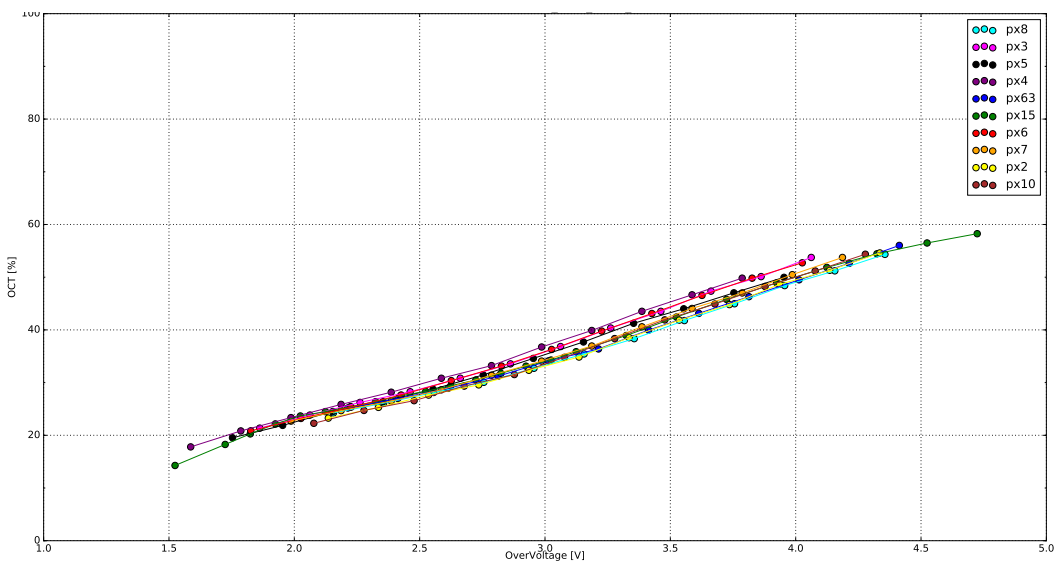
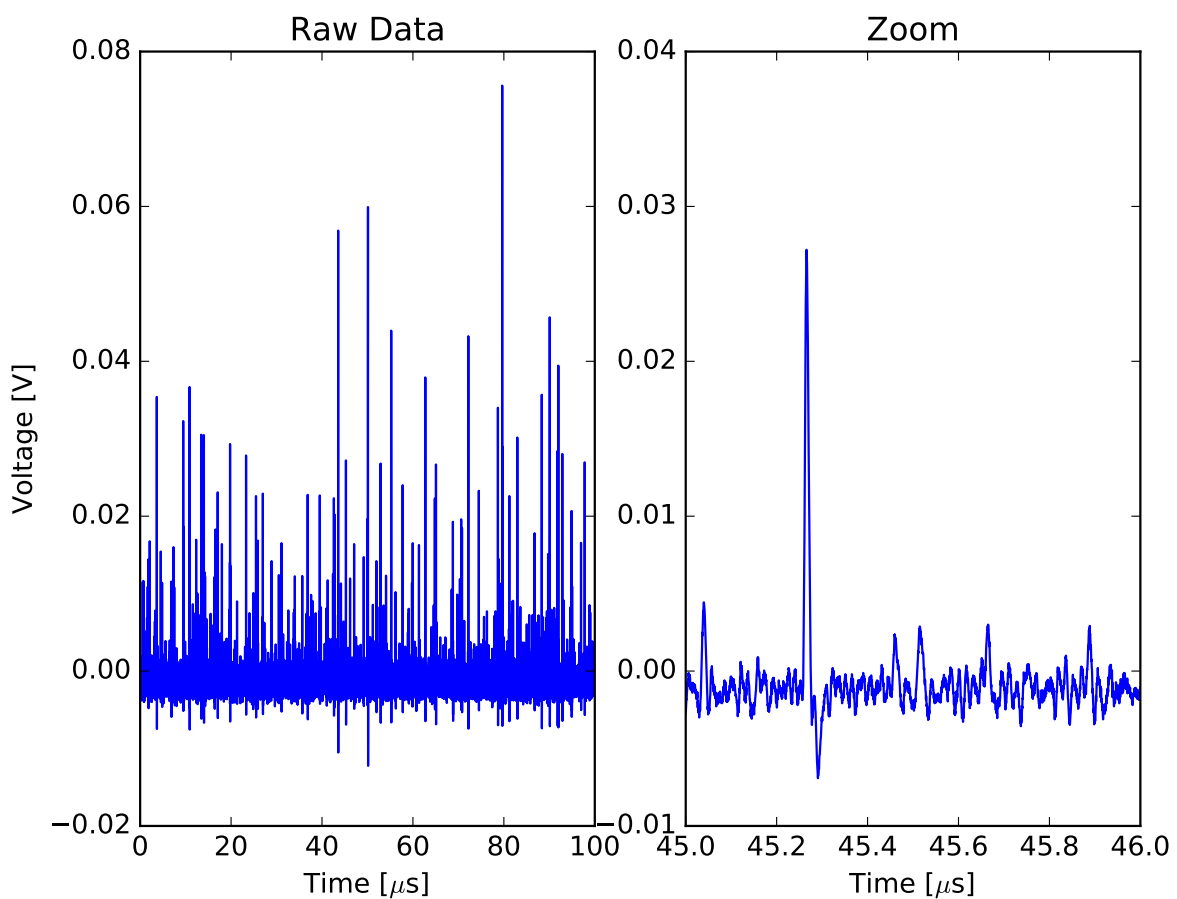


Figure 64: OCT comparison of 10 different pixels of the CHEC-S (HPK S12642-1616PA-50) array

J Additional Data Analysis Plots**Figure 65:** Description

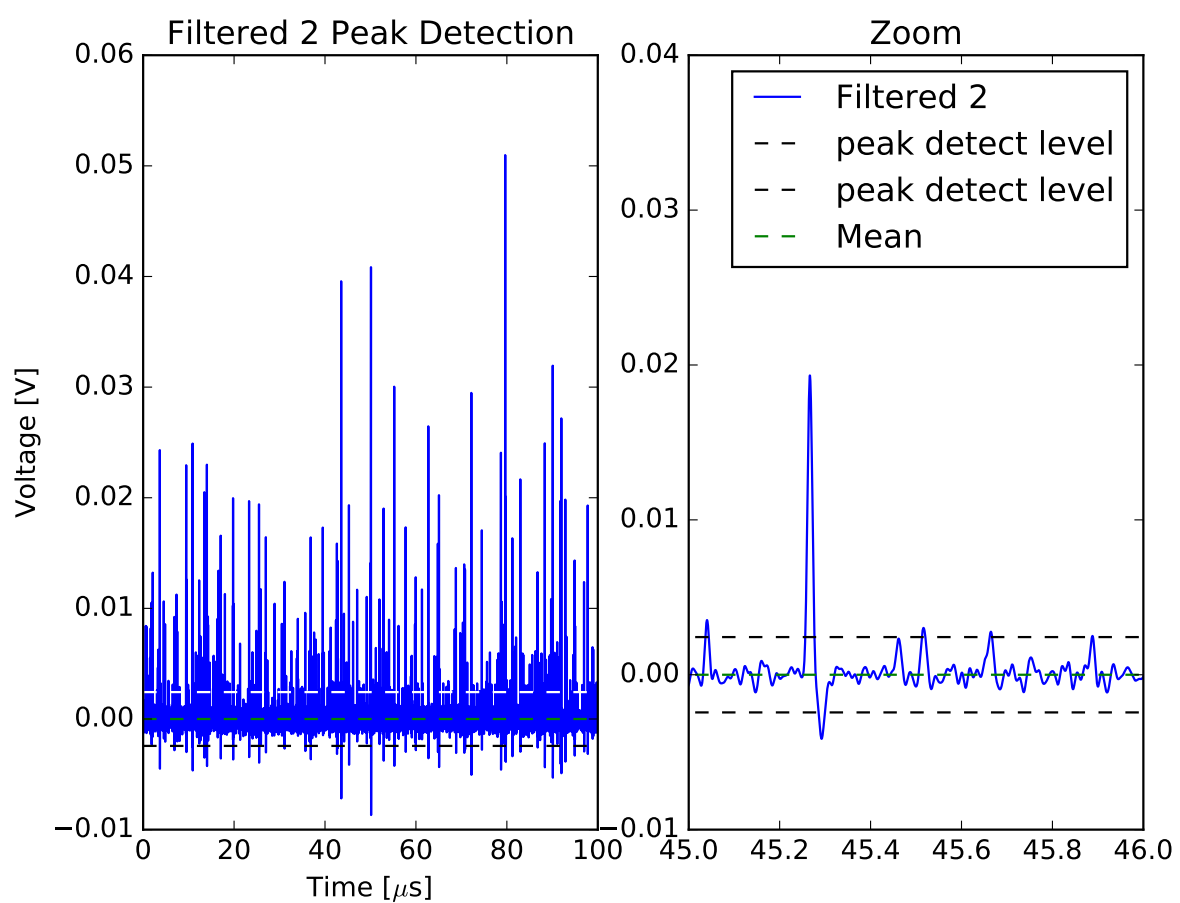


Figure 66: Description

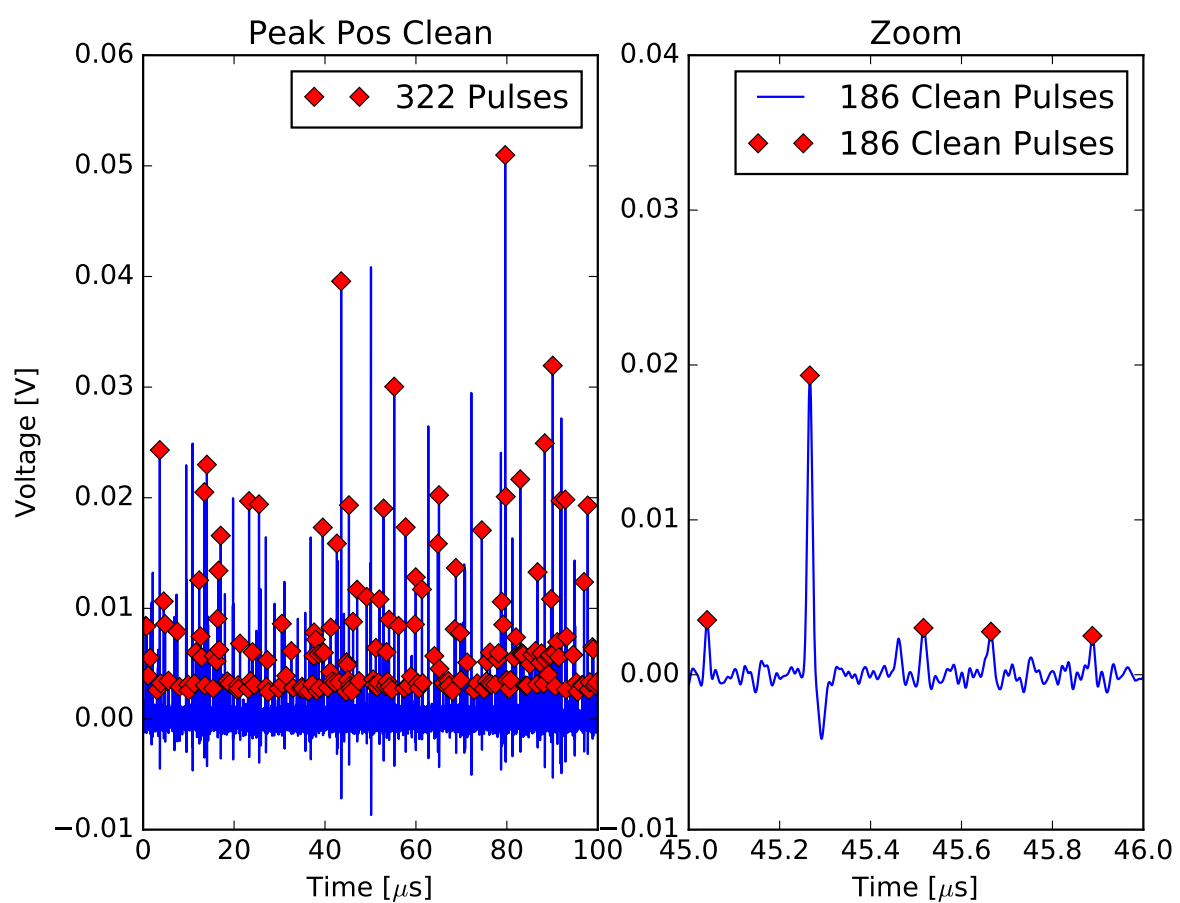


Figure 67: Description

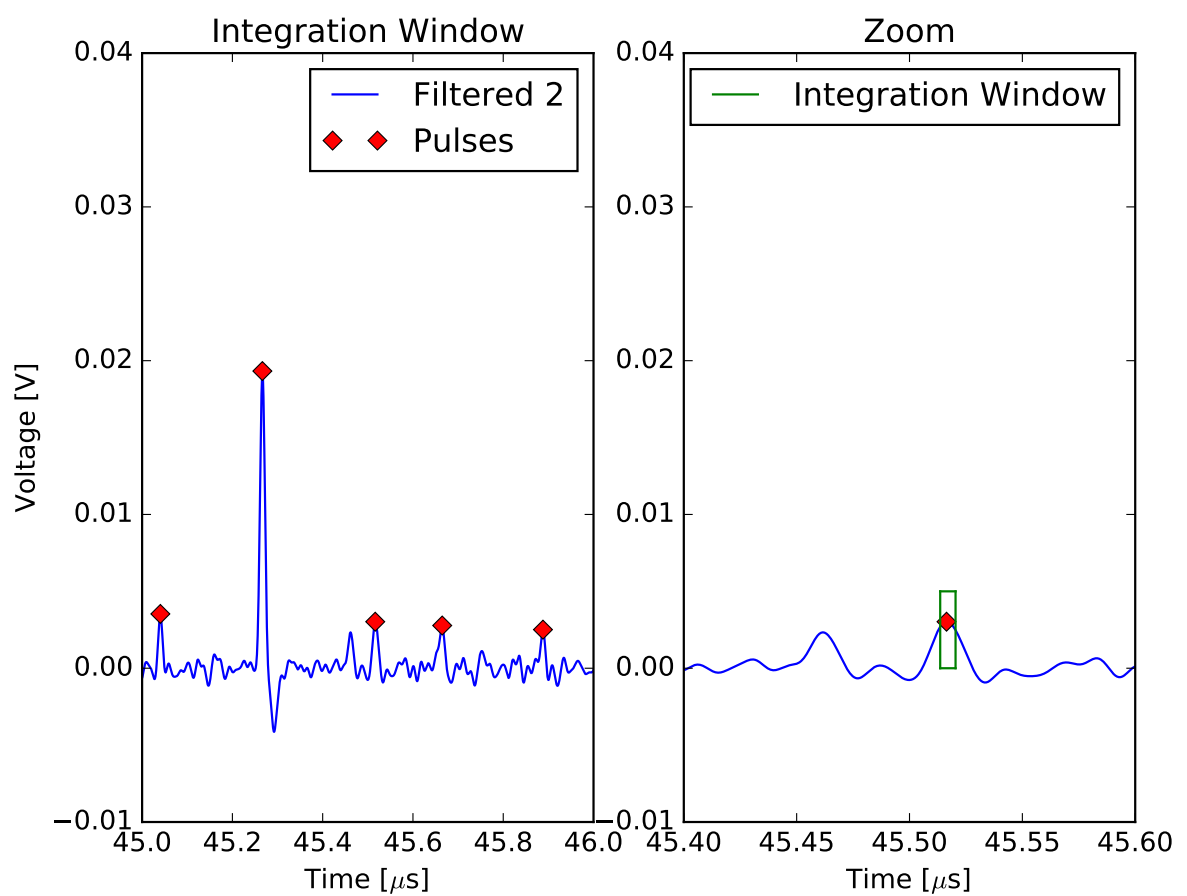


Figure 68: Description

1477 K Multi incident probability and Optical Cross Talk

1479 , _____>,

1480 With increasing DCR the probability of two dark events happening at the same time rises with
1481 increasing bias-voltage. This has an effect on the calculated OCT. In the event of 2 1p.e. pulses
1482 coinciding with each other, they could be misinterpreted as 1 2p.e. pulse. Taking, for example,
1483 the DCR of S13360, 4 MHz at $V_{ov} = 8V$ and $T = 25^\circ C$, with the FWHM of the characteristic
1484 pulse as 5.6 ns we can calculate the probability of two coinciding pulses as $\sim 2.2\%$. This proba-
1485 bility has a direct effect on the calculated OCT (eq:7), in reducing it compared to the calculation.
1486 The OCT at this point is only $\sim 17\%$, but a $\sim 2.2\%$ shift of the number events $N_{events(\geq 1.5p.e.)}$ to
1487 $N_{events(\geq 0.5p.e.)}$ lowers the OCT by $\sim 0.75\%$. Even though the multi hit coincidence is low, this
1488 shows that there are analysis related problems with high Dark Count Rates.

1489

1490

1491 For devices with high DCR and OCT like S12642 this effect grows in magnitude. At only
1492 $V_{ov} = 4.5V$ at $25^\circ C$ the DCR is 6 MHz. With the pulse FWHM of 9 ns this leads to a coincidence
1493 of 5.4%. The OCT at that point is 55%, so a reduction of 5.4% of the $N_{events(\geq 1.5p.e.)}$ towards the
1494 $N_{events(\geq 0.5p.e.)}$ leads to a reduction of the OCT by 5.6%.

1495 Maybe a half FWHM overlap is more real, since now overlap is marked as true, even when
1496 the 2 pulses blur into a very blurry one by only "touching" with their FWHM. Dont know, maybe
1497 half fwhm would be more real.

¹⁴⁹⁸ Erklärung zur Master-Thesis

¹⁴⁹⁹ Hiermit versichere ich, die vorliegende Master-Thesis ohne Hilfe Dritter nur mit
¹⁵⁰⁰ den angegebenen Quellen und Hilfsmitteln angefertigt zu haben. Alle Stellen, die
¹⁵⁰¹ aus Quellen entnommen wurden, sind als solche kenntlich gemacht. Diese Arbeit
¹⁵⁰² hat in gleicher oder ähnlicher Form noch keiner Prüfungsbehörde vorgelegen.

¹⁵⁰³ Darmstadt, den April 25, 2017

¹⁵⁰⁴ _____

¹⁵⁰⁵ (B. Gebhardt)